

## Promises and Challenges of Next-Generation “Beyond Li-ion” Batteries for Electric Vehicles and Grid Decarbonization

Yaosen Tian, Guobo Zeng, Ann Rutt, Tan Shi, Haegyeom Kim, Jingyang Wang, Julius Koettgen, Yingzhi Sun, Bin Ouyang, Tina Chen, Zhengyan Lun, Ziqin Rong, Kristin Persson,\* and Gerbrand Ceder\*



Cite This: <https://dx.doi.org/10.1021/acs.chemrev.0c00767>



Read Online

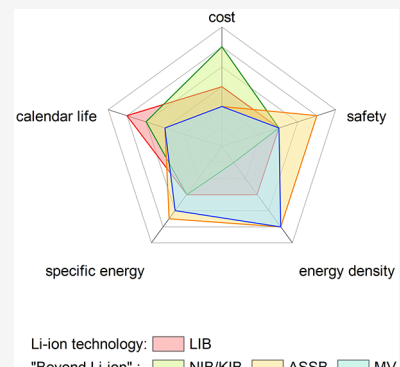
ACCESS |

Metrics & More

Article Recommendations

Supporting Information

**ABSTRACT:** The tremendous improvement in performance and cost of lithium-ion batteries (LIBs) have made them the technology of choice for electrical energy storage. While established battery chemistries and cell architectures for Li-ion batteries achieve good power and energy density, LIBs are unlikely to meet all the performance, cost, and scaling targets required for energy storage, in particular, in large-scale applications such as electrified transportation and grids. The demand to further reduce cost and/or increase energy density, as well as the growing concern related to natural resource needs for Li-ion have accelerated the investigation of so-called “beyond Li-ion” technologies. In this review, we will discuss the recent achievements, challenges, and opportunities of four important “beyond Li-ion” technologies: Na-ion batteries, K-ion batteries, all-solid-state batteries, and multivalent batteries. The fundamental science behind the challenges, and potential solutions toward the goals of a low-cost and/or high-energy-density future, are discussed in detail for each technology. While it is unlikely that any given new technology will fully replace Li-ion in the near future, “beyond Li-ion” technologies should be thought of as opportunities for energy storage to grow into mid/large-scale applications.



### CONTENTS

1. Introduction	B
2. Na-ion and K-ion Batteries	D
2.1. Layered Oxide Cathodes	D
2.2. Polyanion and Prussian Blue Analogue Cathodes	F
2.2.1. Polyanionic Compound Cathodes	F
2.2.2. Inductive Effect in Fluorophosphates	G
2.2.3. Selection of Transition Metals in NASICONs	G
2.2.4. Prussian Blue Analogue (PBA) Cathodes	H
2.3. Graphitic Carbon Anodes	I
2.4. Hard Carbon Anodes	J
2.4.1. Effect of Synthesis Conditions on Electrochemical Properties of Hard Carbon Anodes	J
2.4.2. Overview of Hard Carbon Structure Models and Na-Insertion	J
2.5. Low-Voltage Intercalation Anodes	K
2.6. Alloying Reaction Anodes	L
2.7. Outlook for Na/K-ion Batteries	L
3. All-Solid-State Batteries	M
3.1. Opportunities for Solid-State Batteries	M
3.2. Accelerated Development of Fast Ion Conductors	O
3.3. Challenges Facing ASSBs	P

3.3.1. Intrinsic Stability of SEs	P
3.3.2. Chemical Reactivity with Cathodes and Coatings	R
3.4. Interfacial Stability with Li/Na Metal Anode	T
3.4.1. Dendrites in ASSBs	T
3.5. Practical Considerations for Full-Cell Fabrication	V
3.5.1. Composite Electrode Morphology	V
3.5.2. Thin Solid Electrolyte Separator	V
3.6. Outlook for ASSBs	W
4. Multivalent (Mg and Ca) Batteries	W
4.1. Introduction	W
4.2. Mg and Ca Anodes	X
4.2.1. Metal Anode Electrodeposition and Surface Morphology	X
4.2.2. Alternative Mg and Ca Anodes Promise Energy Density	X
4.3. Mg and Ca Liquid Organic Electrolytes	X
4.3.1. Monovalent vs Multivalent Electrolytes	X

Received: July 22, 2020

4.3.2. Progress in Mg Electrolytes	Y
4.3.3. Development of Ca Electrolytes	AA
4.4. Mg and Ca Cathodes	AA
4.4.1. Prominent Mg and Ca Intercalation Cathodes	AA
4.4.2. Cathode Multivalent-Ion Mobility	AB
4.4.3. Challenges in Synthesizing Mg and Ca Cathodes with Low Migration Barriers	AC
4.5. Summary and Outlook for Multivalent Batteries	AD
5. Summary and Outlook	AE
Associated Content	AF
Supporting Information	AF
Special Issue Paper	AF
Author Information	AF
Corresponding Authors	AF
Authors	AF
Author Contributions	AG
Notes	AG
Biographies	AG
Acknowledgments	AH
References	AH

## 1. INTRODUCTION

The world is going electric. The sustained improvement in performance and price of lithium-ion batteries (LIBs) have made them the technology of choice for electrical energy storage. The gravimetric energy density of LIBs increased from approximately 90 Wh kg<sup>-1</sup> at the cell level in the 1990s to over 250 Wh kg<sup>-1</sup> today,<sup>1</sup> which has enabled their successful application in portable electronics, electric vehicles (EVs), and LIB-based grid storage. Today, Li-ion is even considered for electric flight.<sup>2,3</sup> In 2018, the global EV fleet exceeded 5.1 million vehicles, up 2 million from the previous year, with the number of new electric car sales almost doubling.<sup>1,4,5</sup> Over decades of development, the cell architecture and electrode material options for LIBs have been established. Olivines (e.g., LiFePO<sub>4</sub>, i.e., LFP), layered oxides (e.g., LiNi<sub>0.8</sub>Co<sub>0.15</sub>Al<sub>0.05</sub>O<sub>2</sub>, i.e., NCA, and Li(Ni,Mn,Co)O<sub>2</sub>, i.e., NMC), and spinels (e.g., LiMn<sub>2</sub>O<sub>4</sub>, i.e., LMO) are typically used as the cathodes, which are separated from a graphite anode by a polymer separator(s) immersed in a carbonate-based organic liquid electrolyte. Manufacturing improvements have significantly reduced the cost of LIB modules from over 1000 USD kWh<sup>-1</sup> to less than 150 USD kWh<sup>-1</sup> today.<sup>1,6</sup> Its consistent improvement and dramatic market growth is also exposing the potential challenges for lithium-ion (Li-ion) based energy storage: (1) continued expectation for cost reduction, in particular, in large-scale applications such as EV and grid; (2) how will the energy density be further increased given that there is no further roadmap for cathode or anode materials with higher energy density; (3) resource issues; (4) safety. We discuss these issues very briefly and will later in the article put new “beyond Li-ion” technologies in this context, as each of them should at a minimum address one of these challenges.

While Li-ion is already being integrated into the grid,<sup>7–9</sup> it is estimated that the energy storage cost must fall further to support wind and solar energy-based electricity generation, in particular, once the higher-value applications in the grid such as frequency regulation and intraday load shifting are exhausted. In addition, the emerging EV market calls for lower-cost and higher-energy density automotive batteries to increase travel

distances to sufficient levels for typical driving patterns. In 2017, targets of 350 Wh kg<sup>-1</sup> and 750 Wh L<sup>-1</sup> at the cell level for automotive batteries by 2020 were proposed by the U.S. Department of Energy (DOE) and U.S. Advanced Battery Consortium (USABC).<sup>10–13</sup> Today’s Li-ion chemistry is maturing, with Li(Ni,Mn,Co)O<sub>2</sub> (i.e., NMC) compounds dominating the cathode, and graphite (both synthetic and natural) still almost exclusively used for the anode. While pure Si anodes, or Si-blended into graphite anodes, would increase the specific energy and energy density of Li-ion cells,<sup>14–16</sup> the Si content in today’s commercial cells is very limited due to lifetime problems caused by the nonpassivating SEI on Si.<sup>17–19</sup> NMC cathodes have evolved from compounds with equal amounts of Ni, Mn, Co “111” to high Ni content materials such as “622”, “811” (the numbers specify the relative amount of Ni, Mn, and Co). The higher Ni content lowers the charging voltage at the top of charge, thereby enabling higher capacity, but the gains from further modifying the cathode are becoming increasingly limited. The most serious issue for the further scaling of current Li-ion technology is most likely the metals resource problem. In NMC materials one needs approximately 1 kg of Ni or Co per kWh of energy storage. When the Li-ion industry scales to 1 TWh of production/year, approximately 1 million tons of combined (Ni,Co) will be needed. This will approach 30–40% of current Ni production and more than half of all Co production in the world. While the Co problem is well documented,<sup>20</sup> the Ni resource limitations are only now emerging. Note that 1 TWh of Li-ion capacity can provide only 10 million EVs ( $\approx$ 10% of world annual vehicle production) with a 100 kWh battery (required to drive 350 miles). SNE research in Korea predicts the Li-ion market to reach annual production of over 3 TWh.<sup>21</sup> It is unlikely that this can be supported by the current cathode chemistries except for LiFePO<sub>4</sub>. While novel directions for cathode materials based on less resource constrained metals are promising,<sup>22–26</sup> any new cathode material is at least 10 years out from large-scale commercialization due to the very long timeline to optimize, test, and certify new materials.

With the materials-level advancements in LIBs approaching their limits,<sup>27</sup> the demands for lower cost and higher energy density and the growing concerns related to natural resources have triggered the investigation of so-called “beyond Li-ion” technologies. It is unlikely that one single “beyond Li-ion technology” will address all issues of Li-ion. We therefore chose to discuss various technologies, point out the status of them, and the aspects in which they may outperform Li-ion.

Na-ion batteries (NIBs) and K-ion batteries (KIBs) are two examples of “beyond Li-ion” technologies that can potentially solve the resource issues facing LIBs, especially as cost-effective alternatives in applications for which the gravimetric and volumetric energy density are of less importance such as load leveling for power grids. The ability to use inexpensive redox species such as Mn and Fe in NIB or KIB cathodes instead of Co and Ni is expected to substantially reduce the total cost of a cell. The costs of the raw materials for selected active cathode materials for LIBs, NIBs, and KIBs are compared in Figure 1. The gravimetric energy densities of the full cells constructed using these materials are also compared. As the cost of materials contributes significantly to the overall cell cost today, the remarkably inexpensive cathode active material precursors used in NIBs or KIBs are likely to result in significant cost savings. For example, the layered P2-structured sodium manganese iron oxide (Na<sub>2/3</sub>Mn<sub>1/2</sub>Fe<sub>1/2</sub>O<sub>2</sub>, i.e., P2-NMFO) and lithium nickel

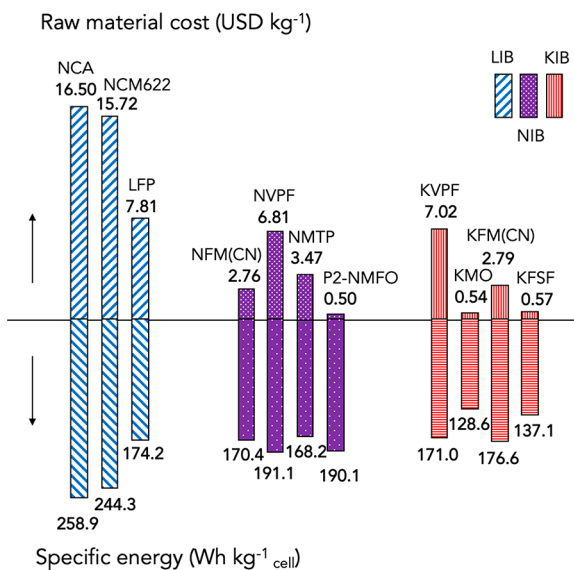


**Figure 1.** Cost of raw materials (direction up) for selected active cathode materials used in LIBs, NIBs, and KIBs and corresponding full-cell specific energy (direction down) calculated at the cell level. Data from the Argonne National Laboratory's Battery Performance and Cost (BatPac)<sup>30</sup> model were used as inputs. The total cost of raw materials accounts for 55–90% of the cost of the processed Li-ion cathode active materials based on data reported for the BatPaC model.<sup>30</sup> Assumptions for the NIBs and KIBs: the cathode composite contains 89% of active material; the NIB cell employs a hard carbon anode with a density of 1.55 g cm<sup>-3</sup> (for active negative electrode material) and specific capacity of 350 mAh g<sup>-1</sup>, and the KIB cell employs a graphite anode with a specific capacity of 250 mAh g<sup>-1</sup>. Al current collectors with a thickness of 15 µm are used in both NIBs and KIBs. The detailed calculation method is described in the Supporting Information, Supplemental Note S1.

cobalt manganese oxide cathode ( $\text{LiNi}_{0.6}\text{Co}_{0.2}\text{Mn}_{0.2}\text{O}_2$ , i.e., NCM622) provide similar specific energies (244.3 Wh kg<sup>-1</sup> cell for NCM622 vs 190.1 Wh kg<sup>-1</sup> cell for P2-NMFO: ~28% reduction); however, the cost of the raw materials for P2-NMFO is more than 30 times lower than for NCA. While raw materials cost certainly does not by itself set cathode price, it does provide an important floor to the price. NIBs may also enable additional cost reduction by replacing the copper current collector in LIBs with an aluminum or stainless steel one.<sup>28,29</sup> NIBs and KIBs can furthermore take advantage of decades of accumulated knowledge on the manufacturing and cell architecture of LIBs, allowing for their faster adoption in large-scale stationary applications.

Replacing the graphite anode with Li metal would provide a path to significantly increase the energy density of today's Li-ion batteries. Compared with current LIBs, all-solid-state batteries (ASSBs) are better suited for utilizing a Li metal anode because the safety concerns are partially eliminated by replacing the organic liquid electrolyte with an inorganic solid electrolyte (SE). Figure 2 compares the specific energies and energy densities at the cell level of the common cathodes used in a typical Li-ion cell and a Li-metal ASSB. Because of the reduction in volume and mass associated with the use of a Li metal anode, multiple selected Li-ion cathodes deliver volumetric energy densities larger than 750 Wh L<sup>-1</sup> at the cell level in the ASSB, with a maximum volumetric energy density of 1373.8 Wh L<sup>-1</sup> reached using the NCA cathode. Although these comparisons do not represent the optimal cell-level energy densities of

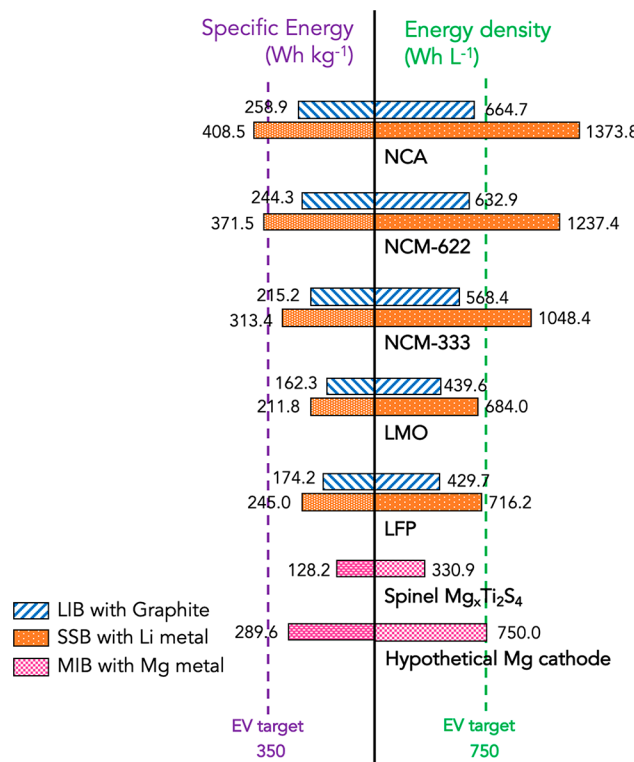


**Figure 2.** Specific energy and energy density calculations of LIBs and conceptual ASSBs and MIBs using selected cathode active materials. The inputs employ data from the BatPaC model.<sup>30</sup> Assumptions for the lithium–metal ASSB cell: a Li–metal anode is used in all ASSBs and a Li utilization of 0.80 was set to determine the anode thickness; the cathode composite contains the same cathode loading as in the LIB (80–83 wt %, depending on the cathode), 6 wt % conductive carbon, and SE powder of remaining weight ratio; the cell uses a  $\text{Li}_2\text{S}–\text{P}_2\text{S}_5$  solid separator of 20 µm thickness with a porosity of 5 vol % in SE pellet and a density of 1.87 g cm<sup>-3</sup>. The calculation for the hypothetical Mg battery assumes the identification of improved multivalent cathodes with capacity of 165 mAh g<sup>-1</sup> and voltage of 3.1 V vs Mg metal. The detailed calculation method is described in the Supporting Information, Supplemental Note S1.

various ASSB systems, they demonstrate the significant energy density increase that can be achieved using established LIB cathodes in a ASSB configuration. Given the significance of Li metal as an anode in ASSB a solution to the problem of Li metal penetration through the solid electrolyte remains one of the primary research and engineering challenges. Other lithium-based “beyond Li-ion” technologies, such as Li–S and Li–air batteries, can also take advantage of Li metal anodes to greatly increase the cell-level energy density. However, in this review paper, we will not discuss these technologies, as their fundamental problems are very different than for the intercalation chemistries discussed in this paper, and many good reviews documenting the problems with these technologies are available.<sup>31–35</sup> While Li–S is a potentially very low cost and high specific energy play, its fundamental limitations on energy density make it an unlikely technology for much of today's Li-ion market. This is to some extent also the case for Li–air, although more uncertainty exist as how a practical Li–air cell system would be built, making extrapolations of energy density more difficult. In addition, both Li–S and Li–air share the Li metal dendrite formation problem that has plagued

attempts to introduce Li metal anodes in liquid-electrolyte Li-ion configurations.

Multivalent battery chemistries offer another interesting path to reach higher energy density for EV applications. Each individual multivalent ion carries multiple charges, leading to larger capacities than those achieved using Li ions for storage of the same number of working ions in an electrode. Compared with Li metal, metallic multivalent anodes offer further improvement in the volumetric energy density (e.g., a theoretical volumetric energy density of  $\sim 3833 \text{ mAh cm}^{-3}$  for Mg metal compared with  $\sim 2046 \text{ mAh cm}^{-3}$  for Li metal<sup>27</sup>). However, the realization of high-energy density multivalent batteries remains limited by the currently available multivalent cathodes. Figure 2 shows the Mg battery energy densities estimated from using (1) a  $\text{Mg}_x\text{Ti}_2\text{S}_4$  ( $0 < x < 1$ ) spinel cathode (representing a state-of-the-art multivalent battery prototype) and (2) a hypothetical, more-energy-dense Mg cathode (assuming the identification of improved multivalent cathodes). This figure illustrates that the energy densities of current multivalent battery prototypes are still far below what can be achieved or imagined with Li-based technology. However, it is worth noting that both the gravimetric and volumetric capacity densities of a  $\text{Mg}/\text{Ti}_2\text{S}_4$  cell (defined as the cell-level gravimetric and volumetric energy densities divided by the voltage) are higher (107 and  $275.8 \text{ mAh cm}^{-3}$ ) than those of today's LIBs (e.g., 66 and  $171 \text{ mAh cm}^{-3}$  for NCM-622/graphite, and 71 and  $183 \text{ mAh cm}^{-3}$  for NCA/graphite). The high capacity density of  $\text{Mg}/\text{Ti}_2\text{S}_4$  indicates that current Mg prototype systems can potentially provide much higher energy density than current Li-ion systems if Mg cathodes could be found that operate at similar voltages as those of Li-ion cathodes. In addition to their potential energy density and/or capacity density advantages, multivalent batteries also provide long-term cost and sustainable resource availability advantages because of the greater abundance of Mg and Ca compounds relative to that of Li. In addition, similar cell configurations to those of current LIBs can be used with Mg or Ca metal anodes for multivalent batteries because these metals are less prone to dendritic growth than Li, which allows multivalent batteries to utilize the manufacturing knowledge already established by the LIB industry. These factors would further reduce the cost of multivalent batteries and accelerate their commercialization. Therefore, if high energy density electrode materials can be developed, Mg and Ca batteries are likely to be able to deliver the unique combination of high energy density and low cost.

In this review, we will discuss the recent achievements, challenges, and opportunities of the four main “beyond Li-ion” technologies: NIBs, KIBs, ASSBs, and multivalent batteries. In each section, the major achievements for the individual technology are briefly summarized, and the remaining challenges toward the goals of a low-cost and/or high-energy density future are discussed in detail. The scope of this review is intended not only to present a collection of electrode and/or electrolyte materials for each individual technology to meet the commercialization requirements but also to critically analyze the fundamental science behind the challenges and offer potential solutions in each field.

## 2. NA-ION AND K-ION BATTERIES

The price of the lithium-based precursor  $\text{Li}_2\text{CO}_3$  (battery grade, 99.5%) skyrocketed from  $\sim 2000 \text{ USD ton}^{-1}$  in 2000 to  $\sim 12\,000 \text{ USD ton}^{-1}$  in 2019 (Shanghai Metals Market (SMM) data<sup>36</sup>), which is one factor that has triggered significant interest in LIB

alternatives, including NIBs and KIBs. The price of  $\text{Na}_2\text{CO}_3$  and  $\text{K}_2\text{CO}_3$  in 2019 was  $\sim 150 \text{ USD ton}^{-1}$  and  $\sim 790 \text{ USD ton}^{-1}$ , respectively.<sup>37</sup> More important for battery cost is the transition metals components in the cathode. Multiple NIB and KIB cathodes have been developed based on inexpensive Mn and Fe redox. More expensive and scarce transition metals such as Co ( $\sim 40\,000 \text{ USD ton}^{-1}$  in 2020, SMM data) and Ni ( $\sim 16\,000 \text{ USD ton}^{-1}$  in 2020, SMM data), which are essential for Li-ion batteries, do not seem essential for NIB or KIB, making them a viable alternative to address resource and cost issues of Li-ion. According to Wood MacKenzie Power and Renewable's latest report in 2019,<sup>38</sup> the global energy storage for grid deployments will grow 13-fold over the next six years from a 12 GWh market in 2018 to a 158 GWh market in 2024. While layered transition metal oxides (TMOs) are obvious cathode candidates for NIB and KIB, we argue that polyanionic compounds and Prussian blue analogues (PBAs) may be better alternatives. We also discuss the challenge of finding good negative electrodes (graphitic carbon, hard carbon, low-voltage intercalation compounds, and alloying-reaction compounds for these technologies).

### 2.1. Layered Oxide Cathodes

Layered oxides of chemical formula  $\text{Na}_x\text{MO}_2(\text{K}_x\text{MO}_2)$  consist of repeating sheets of edge-sharing transition metal octahedra ( $\text{MO}_6$ ), with Na/K ions sandwiched in between. Depending on the anion coordination of the alkali ion and the stacking of the oxygen layers, several polymorphs exist. In the notation first introduced by C. Delmas,<sup>39</sup> the structure is labeled by the coordination geometry around the alkali ion (O, octahedral; P, prismatic) and by the number of O–M–O and O–alkali–O layers that need to be stacked perpendicular to the layer before periodicity is achieved. A prime symbol indicates a monoclinic or orthorhombic distortion, which typically arises because of alkali vacancy ordering, metal ordering, or collective Jahn–Teller distortions. Hence, a P2 structure has prismatically coordinated alkali ions and oxygen stacking ABBA. O3 has octahedral alkali ions and oxygen stacking ABCABC. The latter stacking can also be thought of as a (distorted) FCC lattice of anions with the cations layering in the (111) plane, highlighting the relation between O3 structures and rocksalts.<sup>40</sup> Typically, O3 ( $x = 1$ ), O3' ( $0.75 < x < 1$ ), P3 ( $x \approx 0.6$ ), and P2 ( $x \approx 0.67$ ) phases can be directly synthesized via a solid-state method. Because layered structures are generally stabilized by the size difference of the alkali ion and the transition metal,<sup>41,42</sup> many more types of  $\text{Na}_x\text{MO}_2$  and  $\text{K}_x\text{MO}_2$  compounds form in a layered structure compared to  $\text{Li}_x\text{MO}_2$ . For example, most of the first-row transition metals (Ti, V, Cr, Mn, Fe, Co, Ni) can crystallize in electrochemically active layered O3 structures with Na.<sup>43–45,45–49</sup> This leads to tremendous chemical flexibility in making potential layered Na-ion cathodes.<sup>50,51</sup> It has been shown that the large size of Na and K ions lowers the transition metal mobility in layered oxides,<sup>52</sup> which makes Na and K-layered compounds less vulnerable to the transition metal disorder upon cycling, which is the main issue that restricts layered Li-cathodes to the Ni–Mn–Co chemistry. While  $\text{Li}_x\text{MO}_2$  only forms layered oxides in which Li is octahedrally coordinated (O3/O2 structures),  $\text{Na}_x\text{MO}_2$  and  $\text{K}_x\text{MO}_2$  can also form structures in which Na or K ions are prismatically coordinated by oxygen (P3/P2 structures). Details of the nomenclature have been described by Delmas et al.<sup>39</sup> Layered oxides can have large theoretical capacity, high density, and facile synthesis methods, but many of them suffer from low

average voltage and poor capacity retention when highly charged, possibly due to structural instabilities in the deep-charged state.<sup>50,51</sup>

It is often stated that the rate capability and capacity retention of P2 phases outperform that of the O3 phase as Na can migrate directly from one prismatic site to another through the shared rectangular face.<sup>53–55</sup> In contrast, in the O3 structure, the octahedral-coordinated Na ions must migrate through a tetrahedral intermediate site, which introduces a high-energy migration barrier. This idea is supported by theoretical work of Mo et al., who calculated activation energies for Na migration of 0.20 eV in P2–Na<sub>0.69</sub>CoO<sub>2</sub> and 0.28 eV in O3–Na<sub>0.67</sub>CoO<sub>2</sub>.<sup>54</sup> Experimentally, however, the P2 phase does not always outperform the O3 phase. Figure 3 summarizes the rate

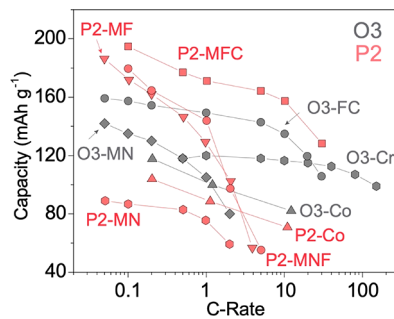


**Figure 3.** Discharge capacity as a function of C-rate for various Na layered oxides. P2–MF: Na<sub>0.67</sub>Mn<sub>0.5</sub>Fe<sub>0.5</sub>O<sub>2</sub>.<sup>63</sup> P2–MFC: Na<sub>0.67</sub>Mn<sub>0.5</sub>Fe<sub>0.25</sub>Co<sub>0.25</sub>O<sub>2</sub>.<sup>47</sup> P2–MN: Na<sub>0.67</sub>Mn<sub>0.7</sub>Ni<sub>0.33</sub>O<sub>2</sub>.<sup>64</sup> P2–MNF: Na<sub>0.67</sub>Mn<sub>0.63</sub>Ni<sub>0.23</sub>Fe<sub>0.13</sub>O<sub>2</sub>.<sup>65</sup> P2–Co: Na<sub>0.67</sub>CoO<sub>2</sub>.<sup>66</sup> O3–FC: NaFe<sub>0.5</sub>Co<sub>0.5</sub>O<sub>2</sub>.<sup>67</sup> O3–MN: NaMn<sub>0.5</sub>Ni<sub>0.5</sub>O<sub>2</sub>.<sup>57</sup> O3–Co: NaCoO<sub>2</sub>.<sup>66</sup> and O3–Cr: NaCrO<sub>2</sub>.<sup>56</sup>

capabilities of various P2– and O3–Na layered oxide cathodes. Some O3 cathode materials exhibit superb rate capability, such as O3–NaCrO<sub>2</sub>,<sup>56</sup> which delivers a discharge capacity of 99 mAh g<sup>-1</sup> at a rate of 150C (75% of the capacity at 1C). When comparing the rate capabilities from different studies in Figure 3, one needs to keep in mind that the high rate performance can be influenced by cell assembly procedures, electrode preparation methods, particle size and morphology, and conductive additives. Nonetheless, because a high rate is not possible without sufficient Na mobility, the results in Figure 3 confirm the high intrinsic diffusivity of Na in many layered compounds.

Furthermore, the multiple phase transformations in O3 phases do not necessarily lead to poor cyclability, as several O3 cathodes have been reported to exhibit good capacity retention.<sup>57–59</sup> For example, O3–NaNi<sub>0.5</sub>Mn<sub>0.5</sub>O<sub>2</sub><sup>57</sup> and O3–NaNi<sub>0.5</sub>Mn<sub>0.2</sub>Ti<sub>0.3</sub>O<sub>2</sub><sup>60</sup> exhibit good capacity retention (90% and 85% after 100 and 200 cycles at 1C, respectively). This evidence indicates that capacity degradation does not originate from multiple phase transitions, as is often accepted, but rather issue stems from structural instability in the deep deintercalation state (at low Na/K content), which is an intrinsic problem for both O3 and P2 phases.<sup>59,61,62</sup> Therefore, to improve the cycling stability of layered transition metal oxides, a better understanding of how to improve the structural stability at low Na/K content is required.

While high capacity and reasonable cycling performance have been achieved for several Na layered oxides by mixing two, three, or even four transition metals,<sup>47,50,62,65</sup> several disadvantages of layered Na/K cathodes have not been addressed. Because of the lower voltage of Na/K layered oxides, no cathode material has

exhibited an energy density comparable to that of Li layered oxides such as LCO or NCM111. While in itself this is not a critical limitation for stationary applications, lower energy content cathode materials increase the cost of cell overhead (anode, electrolyte, cell manufacturing cost, etc.) and may detract from the intrinsic cost advantages of Na/K batteries. The specific capacities and corresponding average voltages of several Li/Na/K layered oxide cathodes are shown in Figure 4a, clearly

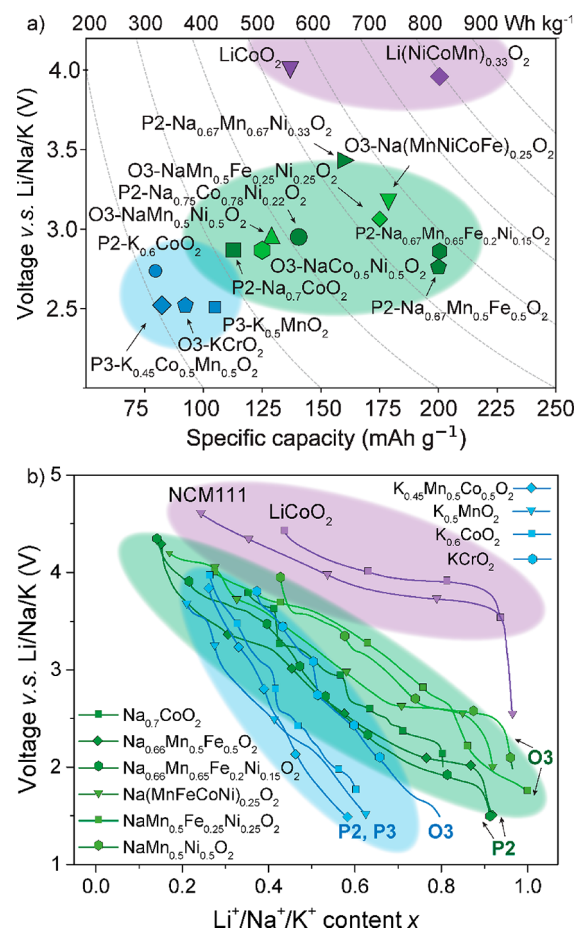


**Figure 4.** (a) Voltage vs capacity map of various Na layered oxides (green) and K layered oxides (blue). Li layered oxides (purple) are shown for comparison. (b) Discharge profiles for various alkali–metal layered oxides. The shaded areas show that the voltage profiles have similar slopes for a particular alkali metal (Li, purple; Na, green; K, blue). Data adapted from LiCoO<sub>2</sub>,<sup>78</sup> Li(NiCoMn)<sub>0.33</sub>O<sub>2</sub>,<sup>79</sup> P2–Na<sub>0.67</sub>Mn<sub>0.67</sub>Ni<sub>0.33</sub>O<sub>2</sub>,<sup>64</sup> P2–Na<sub>0.75</sub>Co<sub>0.78</sub>Ni<sub>0.22</sub>O<sub>2</sub>,<sup>62</sup> P2–Na<sub>0.67</sub>Mn<sub>0.65</sub>Fe<sub>0.2</sub>Ni<sub>0.15</sub>O<sub>2</sub>,<sup>80</sup> P2–Na<sub>0.67</sub>CoO<sub>2</sub>,<sup>66</sup> P2–Na<sub>0.67</sub>Mn<sub>0.5</sub>Fe<sub>0.25</sub>O<sub>2</sub>,<sup>63</sup> O3–NaMn<sub>0.5</sub>Ni<sub>0.5</sub>O<sub>2</sub>,<sup>57</sup> O3–NaCo<sub>0.5</sub>Ni<sub>0.5</sub>O<sub>2</sub>,<sup>81</sup> O3–Na<sub>0.5</sub>Li<sub>0.5</sub>[Mn<sub>0.5</sub>Fe<sub>0.25</sub>Ni<sub>0.25</sub>]<sub>0.95</sub>O<sub>2</sub>,<sup>73</sup> O3–NaMn<sub>0.25</sub>Co<sub>0.25</sub>Fe<sub>0.25</sub>Ni<sub>0.25</sub>O<sub>2</sub>,<sup>62</sup> P3–K<sub>0.5</sub>MnO<sub>2</sub>,<sup>68</sup> P2–K<sub>0.6</sub>CoO<sub>2</sub>,<sup>82</sup> P3–K<sub>0.45</sub>Mn<sub>0.5</sub>Co<sub>0.5</sub>O<sub>2</sub>,<sup>69</sup> O3–KCrO<sub>2</sub>.<sup>70</sup>

demonstrating that the voltages of commercialized Li layered oxides are significantly higher than those of their Na and K counterparts. Na layered oxides typically have average voltages between 2.5 and 3.5 V. The voltage range is even lower for K layered oxides: The average discharge voltages for P3–K<sub>0.5</sub>MnO<sub>2</sub>,<sup>68</sup> P3–K<sub>0.45</sub>Mn<sub>0.5</sub>Co<sub>0.5</sub>O<sub>2</sub>,<sup>69</sup> and O3–KCrO<sub>2</sub><sup>70</sup> are all approximately 2.5 V. Attempts to increase the operating voltage of layered oxides by using transition metal species such as Co<sup>3+/4+</sup> and Ni<sup>3+/4+</sup> have had little success.<sup>71</sup>

No significant improvement was observed in the operating voltages of P2–Na<sub>0.75</sub>Co<sub>0.78</sub>Ni<sub>0.22</sub>O<sub>2</sub><sup>72</sup> and O3–Na<sub>x</sub>Ni<sub>0.5</sub>O<sub>2</sub><sup>73</sup> compared with those of Mn-based Na layered oxides,<sup>59</sup> consistent with the idea put forward in ref 52 that the voltage of the Na and K compounds is largely controlled by the strong alkali–alkali interaction. Because Na<sup>+</sup> and K<sup>+</sup> ions are considerably larger than Li<sup>+</sup>, the interlayer distance between oxide layers in Na and K compounds is larger than that in Li compounds. The larger distance of the oxygen ion to the K-ion reduces its effectiveness in screening the electrostatic repulsion between the alkalis in Na and K materials, which in turn increases the voltage slope<sup>52</sup> and reduces the voltage at the end of discharge. This is illustrated in Figure 4b, which presents the discharge profiles of several alkali–metal layered oxides. The voltage slope for most compounds with a fixed choice of alkali are similar regardless of the transition metal species and oxygen stacking. The slope for Na/K layered compounds is considerably larger than for Li layered compounds, limiting the capacity (and energy density) that can be achieved within a given voltage window.

Different from the other Na layered oxides, O3–NaFeO<sub>2</sub> (also known as  $\alpha$ -NaFeO<sub>2</sub>) exhibits a flat voltage plateau at  $\approx$ 3.4 V with a discharge capacity of 80 mAh g<sup>-1</sup>.<sup>74</sup> This unusually large voltage plateau is attributed to the wide two-phase reaction region when Na ions are deintercalated from NaFeO<sub>2</sub> and may be unique to the Jahn–Teller activity of the Fe<sup>4+</sup> which forms upon charging.<sup>75,76</sup> Although O3–NaFeO<sub>2</sub> suffers from poor cycling stability resulting from Fe migration, it is clear that to achieve more capacity in Na/K layered oxides, one needs to find systems with a wide two-phase region at the top of charge (or end of discharge) to overcome the average slope limitation. For example, Hasa et al. reported an extremely high capacity of 250 mAh g<sup>-1</sup> for P2-type Na<sub>0.6</sub>Ni<sub>0.22</sub>Al<sub>0.11</sub>Mn<sub>0.66</sub>O<sub>2</sub>; the voltage profile contained a clear two-phase plateau originating from the P2–O2 transition at the top of charge.<sup>77</sup> Hence, somewhat counterintuitively, increasing the capacity of Na-layered oxides should focus on finding systems with pronounced first-order phase transformations at end of charge and discharge.

While some Na layered oxides still exhibit reasonable energy density despite having this steep sloped voltage profile, the even larger slope in layered K-oxides makes it unlikely to find good cathodes for K-ion systems in this structure class. Polyanionic compounds or PBAs might be better choices for a K battery and will be discussed in the next section. The very strong K–K interaction also limits the K-content in the as-synthesized cathode material. While O3 Na-compounds can be synthesized at stoichiometry NaMO<sub>2</sub>, for K-compounds this is only true for KCrO<sub>2</sub>,<sup>70</sup> and most layered compounds with K are substoichiometric in K, which would require an additional K source in a K-ion cell.

## 2.2. Polyanion and Prussian Blue Analogue Cathodes

Because of the highly sloped voltage profiles of layered Na and K-ion compounds, host structures that provide more effective screening and/or greater distance between intercalating ions may be better choices for cathodes. While polyanionic compounds and PBAs are usually considered to have poor energy density, based on the experience with Li-ion cathodes, Figure 5 shows that this is not necessarily the case for K and Na. The figure compares the gravimetric energy density (Wh kg<sup>-1</sup>) and volumetric energy density (Wh L<sup>-1</sup>) of layered oxides (e.g., A<sub>x</sub>CoO<sub>2</sub>), polyanionic compounds (e.g., AVPO<sub>4</sub>F), and PBAs (e.g., A-MnFe(CN)<sub>6</sub>), where A = Li, Na, or K.<sup>82–89</sup> For the

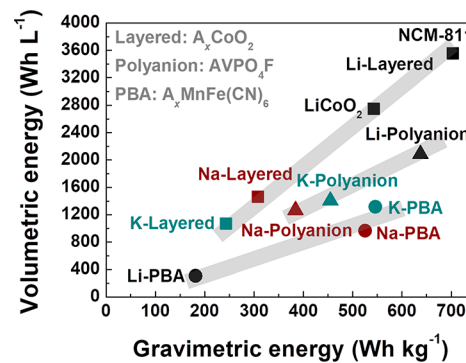


**Figure 5.** Comparison of gravimetric energy density (Wh kg<sup>-1</sup>) and volumetric energy density (Wh L<sup>-1</sup>) of layered oxides (A<sub>x</sub>CoO<sub>2</sub>), polyanionic compounds (AVPO<sub>4</sub>F), and PBAs (A-MnFe(CN)<sub>6</sub>), where A = Li, Na, or K. The gravimetric and volumetric energy densities were calculated from the literature.<sup>82–90</sup> The theoretical material densities of the crystal structures were used to determine the volumetric energy densities.

layered oxides, both the gravimetric and volumetric energy densities significantly decrease with increasing alkali-ion size, which can be ascribed to the increase in molecular weight and structural volume and to the reduction of the capacity and voltage. In contrast, the effect of the alkali-ion size and weight in reducing the energy content is much less pronounced for the polyanion AVPO<sub>4</sub>F and A-PBA systems. Interestingly, in the PBA systems, both the gravimetric and volumetric energy densities increase with increasing alkali-ion size, which will be discussed in the PBA section. While for Na there is still a small decrease in energy density when moving from layered oxides to polyanion and PBAs (though the specific energy increases a lot), for K-cathodes one can clearly increase the specific energy without cost to the energy density by going to nonclose-packed systems.

Whereas layered compounds are clearly the best cathode candidates for Li batteries, the different effects of the alkali-ion size for each class of cathodes (layered oxides vs polyanionic compounds vs PBAs) results in comparable volumetric energy densities for polyanionic compounds/PBAs and layered compounds in Na and K systems. For example, layered LCO exhibits a much higher volumetric energy density than polyanionic LiVPO<sub>4</sub>F (by 24%) despite its lower gravimetric energy density, which is attributable to the high crystal density of the layered compound. In contrast, the volumetric energy density decreases by only  $\sim$ 13% in moving from layered Na<sub>x</sub>CoO<sub>2</sub> to polyanionic NaVPO<sub>4</sub>F. In the K system, both polyanionic KVPO<sub>4</sub>F and K-PBA exhibit higher volumetric energy densities than the layered K<sub>x</sub>CoO<sub>2</sub>. These results indicate that polyanionic compounds and PBAs have the potential to compete with layered oxides in Na and K systems.

**2.2.1. Polyanionic Compound Cathodes.** Polyanionic compounds with tetrahedral motifs of XO<sub>4</sub> or trigonal motifs of XO<sub>3</sub> (X = P, S, B, Si, etc.) have been extensively investigated as high-voltage cathodes for NIBs and KIBs.<sup>91–94</sup> The most popular polyanion groups include phosphates (PO<sub>4</sub>)<sup>3–</sup><sup>95</sup>, sulfates (SO<sub>4</sub>)<sup>2–</sup><sup>96</sup>, and silicates (SiO<sub>4</sub>)<sup>4–</sup><sup>97</sup> and their derivatives, including fluorophosphates,<sup>98–101</sup> pyrophosphates,<sup>102,103</sup> fluorosulfates,<sup>104</sup> etc. The polyanionic compounds offer several advantages. (i) Because of the structural and chemical variety of polyanionic frameworks, these materials provide the opportunity to explore novel cathode materials with open-framework structures that provide fast Na-ion diffusion pathways. (ii) It is

feasible to tailor the working voltage by modifying the chemical composition. (iii) The unique structural stability of polyanionic groups results in excellent high-voltage stability and improved cyclability compared with that of their layered-oxide counterparts. As these materials have recently been discussed in several excellent review articles,<sup>91,94,105,106</sup> we will limit our scope to discussing how the working voltage of polyanionic compounds can be tailored via (1) the “inductive effect” from anion tuning and (2) the selection of transition metals. We also propose that the energy density can be increased by applying these strategies.

**2.2.2. Inductive Effect in Fluorophosphates.** Fluorophosphates with the general formula  $\text{Na}_x\text{M}_2(\text{PO}_4)_2\text{F}_{3-y}\text{O}_y$ , where  $\text{M} = \text{transition metal}$ ,  $0 \leq x \leq 4$ ,  $0 \leq y \leq 2$ , are some of the most promising polyanionic Na-cathode materials.  $\text{Na}_3\text{V}_2(\text{PO}_4)_2\text{F}_3$  has an average operating voltage of 3.9 V and a capacity of 128 mAh g<sup>-1</sup> (yielding a specific energy density of 499 Wh kg<sup>-1</sup>).<sup>107,108</sup> It can potentially be competitive with some conventional Li-ion cathodes (e.g.,  $\text{LiFePO}_4$  with a specific energy density of 580 Wh kg<sup>-1</sup>).

The crystal structure of  $\text{Na}_3\text{V}_2(\text{PO}_4)_2\text{F}_3$  (NVPF)<sup>112</sup> is shown in Figure 6a and consists of a three-dimensional framework of  $\text{V}_2\text{O}_8\text{F}_3$  biotahedra connected via  $\text{PO}_4$  tetrahedra. The substitution of oxygen for fluorine ( $\text{V}_2\text{O}_8\text{F}_{3-y}\text{O}_y$ ) occurs at the apex of the biotahedra and the F/O ratio can be tuned either by solid-state<sup>107,110</sup> or wet chemistry synthesis.<sup>113</sup> Figure 6b shows the electrochemical performance of six  $\text{Na}_3\text{V}_2(\text{PO}_4)_2\text{F}_{3-y}\text{O}_y$  samples, with  $y$  ranging from 0 (NVPF<sub>3</sub>) to 0.5 (NVPF<sub>2.5</sub>O<sub>0.5</sub>), causing the oxidation state for vanadium to vary from 3+ at  $y = 0$  to 3.25+ at  $y = 0.5$ . Because of the inductive effect, the average voltage for Na-ion intercalation continuously decreases as  $y$  increases (decrease in F/O ratio) even though the valence of V slightly increases in the pristine samples. Similarly, for K-ion intercalation, Kim et al. observed that the voltage decreases for  $\text{KVPO}_4\text{F}$  when F is partially substituted by O. The average voltage drops from 4.33 V for  $\text{KVPO}_4\text{F}$  to 4.20 V for  $\text{KVPO}_{4.36}\text{F}_{0.64}$ .<sup>114</sup>

State-of-the-art NVPF allows reversible intercalation of only 2 Na per formula unit.<sup>109</sup> To improve the energy density of NVPF further and make it a highly competitive cathode material for Na-ion batteries, the third sodium should be cycled in NVPF. This is, however, unlikely in the pristine compound as the voltage to reach the  $\text{V}_2(\text{PO}_4)_2\text{F}_3$  composition is predicted to be  $\approx 5.3$  V,<sup>111</sup> significantly above the electrochemical stability window limit of the electrolyte (4.4–4.7 V). The inductive effect suggests that the working voltage can be manipulated through substitution with another anion of different electronegativity. One strategy, supported by a calculation by Xiao (Figure 6c), is to bring the extraction voltage for the third sodium into the accessible voltage window of the electrolyte<sup>115</sup> by replacing the F in  $\text{Na}_3\text{V}_2(\text{PO}_4)_2\text{F}_3$  with a less electronegative ion, such as Cl or Br. However, so far, this prediction has not been validated with experiments.

Using a different approach, Tarascon et al. recently triggered the activity of the third Na via the formation of a disordered  $\text{Na}_x\text{V}_2(\text{PO}_4)_2\text{F}_3$  phase with tetragonal symmetry ( $I4/mmm$  space group)<sup>116</sup> The authors claim that a new phase forms irreversibly when the third sodium is extracted electrochemically from  $\text{Na}_3\text{V}_2(\text{PO}_4)_2\text{F}_3$  (*Amam*) upon the first charge and hold at 4.8 V, and that this new phase can reversibly intercalate three Na per formula unit over the voltage range of 1–4.8 V. The energy density increases by only ~15% with respect to the conventional NVPF *Amam* phase as the last Na is being reinserted at 1.6 V.

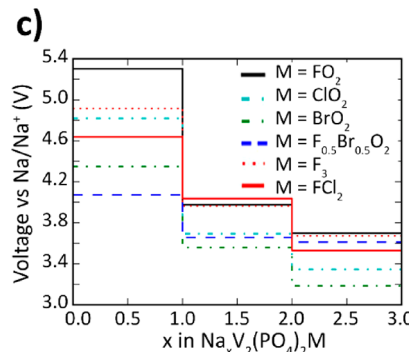
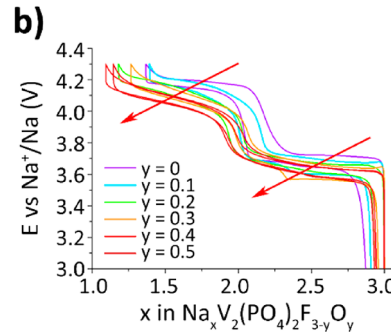
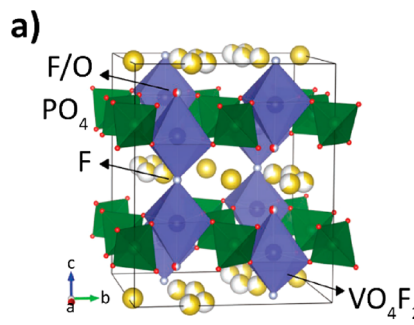


**Figure 6.** (a) Crystal structure of  $\text{Na}_3\text{V}_2(\text{PO}_4)_2\text{F}_{3-y}\text{O}_y$  (either in orthorhombic space group *Amam* or tetragonal *P4<sub>2</sub>/mnm* space group depending on  $y$ ). Reproduced with permission from ref 109. Copyright 2017 Wiley. (b) Voltage profiles for different compositions of  $\text{Na}_3\text{V}_2(\text{PO}_4)_2\text{F}_{3-y}\text{O}_y$  ( $0 \leq y \leq 0.5$ ) cycled at C/20. Reproduced with permission from ref 110. Copyright 2016 American Chemical Society. (c) Computational modifications of  $\text{Na}_3\text{V}_2(\text{PO}_4)_2\text{F}_3$  to enable extraction of the third Na within the electrolyte stability window. Reproduced with permission from ref 111. Copyright 2014 American Chemical Society.

This low discharge voltage of the extra capacity makes it less attractive for practical applications.

**2.2.3. Selection of Transition Metals in NASICONs.** As an alternative to employing the inductive effect to tune the cathode voltage, the transition metal species can also be directly changed as is well illustrated in the NASICON-type compounds. NASICON is an abbreviation for sodium (Na) super ionic conductor, which refers to a family of materials with the chemical formula  $\text{Na}_x\text{NM}(\text{PO}_4)_3$  ( $0 \leq x \leq 4$ , N and M = Ti, V, Cr, Mn, Zr, etc.). They are characterized by an “open” three-dimensional framework enabling fast Na-ion migration, relatively high working voltage (>3.5 V), reasonable specific capacity (~110 mAh g<sup>-1</sup>), and excellent stability in the charged state.<sup>117</sup> The rich selection of N/M combinations enables fine-

tuning of the working voltage of NASICON-type materials. Among the various NASICON compounds,  $\text{Na}_3\text{V}_2(\text{PO}_4)_3$  is a promising candidate because the reversible cycling of two Na per formula unit<sup>124</sup> gives it a reasonable energy density of  $\sim 400 \text{ Wh kg}^{-1}$ .

Figure 7a shows the crystal structure of a typical NASICON-type framework, which is built up with corner-sharing  $\text{MO}_6$  and

$\text{K}$ , etc.,  $\text{M}$  = transition metal (Fe, Mn, Co, Ni, Cu, etc.), and  $0 < x < 2$ . They consist of  $\text{M}_A^{2+}$  and  $\text{M}_B^{3+}$  ions sitting on alternate corners of corner-shared octahedra, which are bridged by cyano ( $\text{C}=\text{N}$ )<sup>-</sup> ligands. Structurally, they form three-dimensional rigid frameworks containing open ionic channels (3.2 Å in diameter in  $\langle 100 \rangle$ ) and spacious interstitial sites,<sup>142,143</sup> which enable fast diffusivity for multiple ions, e.g.,  $\text{Na}^+$ ,  $\text{K}^+$ , etc.

Figure 8b presents the discharge profiles of  $\text{A}_x\text{Mn}[\text{Fe}(\text{CN})_6]$  ( $\text{A} = \text{Li}, \text{Na}$ , and  $\text{K}$ ). As the size of the intercalating ion increases the voltage increases, and, surprisingly, Li-PBA has the lowest capacity and voltage among the three compounds. A similar trend can also be observed in other transition-metal-based PBA systems, as shown in Figure 8c. The high voltage of K intercalation in PBA is likely attributable to the stronger interaction between K ion and the metal–organic framework than that in Na and Li systems, stabilizing the discharged products.<sup>144</sup>

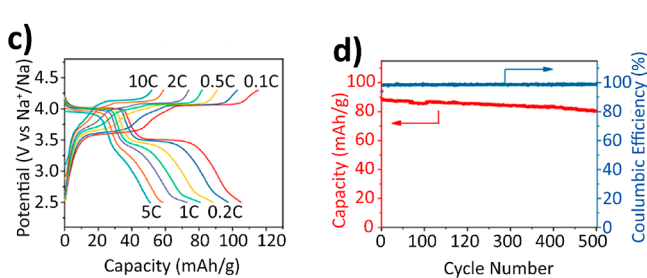


Figure 7. (a) Typical NASICON-type crystal structure,  $\text{Na}_3\text{NM}(\text{PO}_4)_3$  ( $\text{N}, \text{M} = \text{Ti}, \text{V}, \text{Cr}, \text{Mn}, \text{Zr}$ , etc.). (b) Cyclic voltammetry profiles, (c) rate performance, and (d) long-term cycling performance of  $\text{Na}_3\text{MnZr}(\text{PO}_4)_3$ . Reproduced with permission from ref 125. Copyright 2018 American Chemical Society.

$\text{XO}_4$  polyhedra, with interstitial sites accommodating two different types of Na ions: Na(1) with 6-fold coordination and Na(2) with 8-fold coordination. Compared with V-based NASICON-type materials, the Mn-based ones,  $\text{Na}_3\text{MnM}(\text{PO}_4)_3$  ( $\text{M} = \text{Ti}$  and  $\text{Zr}$ ), are not only less expensive and environmentally friendly but also provide higher voltages (at 3.6 and 4.1 V, respectively) with comparable capacity (approximately 110 mAh g<sup>-1</sup>),<sup>125,126</sup> as shown in Figure 7b,c. In addition, carbon coated  $\text{Na}_3\text{MnZr}(\text{PO}_4)_3$  demonstrates excellent rate performance and stable cycling (Figure 7c,d).<sup>125</sup> To achieve higher energy density, fully reversible three-electron redox reactions are desired. In recent work by Mai et al.,  $\text{Na}_3\text{MnTi}(\text{PO}_4)_3$  was shown to have a specific capacity of 160 mAh g<sup>-1</sup> at 0.2C, resulting from the  $\text{Ti}^{3+/4+}$ ,  $\text{Mn}^{2+/3+}$ , and  $\text{Mn}^{3+/4+}$  redox couples at 2.1, 3.5, and 4.0 V, respectively.<sup>127</sup> While the capacity corresponds to reversible intercalation of almost three Na, the actual energy gain is compromised by the low-voltage intercalation of the additional Na at 2.1 V, yielding a total energy density of  $\sim 470 \text{ Wh kg}^{-1}$ . Therefore, NASICON materials that enable the intercalation of three Na at higher voltage requires further optimization through substitution/combination with other transition metals.

**2.2.4. Prussian Blue Analogue (PBA) Cathodes.** Similar to other polyanionic cathode compounds, PBAs have an open framework structure and wide compositional variety.<sup>128,141</sup> PBAs represent a large family of metal hexacyanoferrates with a perovskite-type, face-centered cubic structure (space group  $Fm\bar{3}m$ ), as shown in Figure 8a.<sup>128</sup> The chemical composition of PBAs can be expressed as  $\text{A}_x\text{M}_A[\text{M}_B(\text{CN})_6]_y$ , where  $\text{A} = \text{Li}, \text{Na}$ ,

PBAs are usually prepared via a wet chemistry route at low temperature, which results in a hydrated PBA lattice with a large number of  $\text{M}_B(\text{CN})_6$  vacancies. The chemical formula can be more accurately expressed as  $\text{A}_{2-x}\text{M}_A[\text{M}_B(\text{CN})_6]_y\Box_{1-y}\cdot z\text{H}_2\text{O}$ , where  $\text{M}_A$  and  $\text{M}_B$  represent transition metals and  $\Box$  represents  $\text{M}(\text{CN})_6$  vacancies,  $0 < x < 2$ ,  $0 < y < 1$ . The vacancies and coordinated  $\text{H}_2\text{O}$  in the crystal structure play a crucial role in determining the electrochemical properties. As  $\text{M}_B(\text{CN})_6$  vacancies are charge balanced by a lower Na content that reduce capacity. The vacancy defect also causes  $\text{H}_2\text{O}$  molecules to coordinate with the dangling  $\text{M}_A$  bonds, which decreases the available sites for intercalants and is believed to block the diffusion channels. When  $\text{H}_2\text{O}$  molecules are released upon cycling, they can lead to side reaction with the organic electrolyte which eventually deteriorates the electrochemical performance.<sup>145</sup> Therefore, a defectless structure and low  $\text{H}_2\text{O}$  content are the key factors to realize long-term cycling for PBAs. The importance of creating low defect PBAs was confirmed by Guo et al., who found a considerably larger capacity (170 vs 140 mAh/g) for  $\text{Na}_x\text{Fe}[\text{Fe}(\text{CN})_6]_y\Box_{1-y}\cdot z\text{H}_2\text{O}$  with a low concentration of lattice defects ( $x = 0.61$ ,  $y = 0.94$ ,  $z = 2.6$ ) than for a sample with high concentration of lattice defects ( $x = 0.13$ ,  $y = 0.68$ ,  $z = 3.5$ ).<sup>146</sup> Goodenough et al. reported a scalable method to prepare high-quality and low-cost rhombohedral  $\text{Na}_{1.92}\text{Fe}[\text{Fe}(\text{CN})_6]$ , with a negligible  $\text{H}_2\text{O}$  content (0.08 H<sub>2</sub>O/f.u.), and this material exhibited a high capacity (160 at 10 mA g<sup>-1</sup>), large energy density ( $\sim 490 \text{ Wh kg}^{-1}$ ), good rate capability (up to 15C), and long cycle life.<sup>137</sup> The sensitivity of PBA's performance to the structure has also been observed in KIBs. For instance,  $\text{K}_{0.220}\text{Fe}[\text{Fe}(\text{CN})_6]_{0.805}\cdot 4.01\text{H}_2\text{O}$  with a high vacancy and  $\text{H}_2\text{O}$  content can only deliver a capacity of  $\sim 0.84 \text{ K/f.u.}$  with a low initial Coulombic efficiency of 44%.<sup>147</sup>

Overall, polyanionic compounds have great potential as cathode materials in NIBs and KIBs. Different combinations of transition metals and anion groups have been experimentally explored to determine their corresponding Na/K-ion insertion voltage and capacity, as summarized in Figure 9. However, numerous potential choices for the transition metal and (poly)anionic group are still unexplored, and the synthesis and optimization of each newly proposed compound can be formidable. In this regard, the emerging ab initio-based high-throughput method can shed light on searching and predicting novel electrode materials.<sup>148,149</sup>

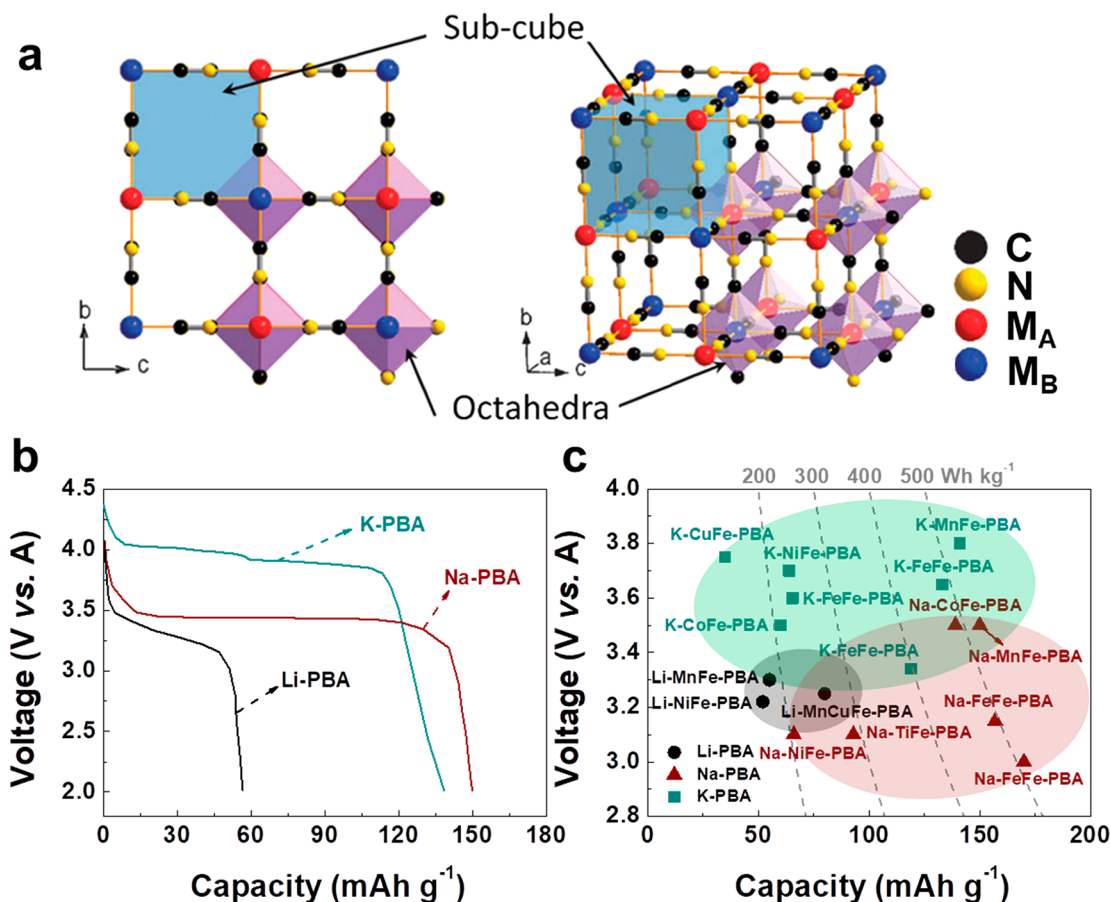


**Figure 8.** (a) Framework of PBAs. Reproduced with permission from ref 128. Copyright 2012 Royal Society of Chemistry. (b) Discharge profiles of A-MnFe-PBA ( $A = \text{Li}, \text{Na}$ , and  $\text{K}$ ), plotted using data from refs 87–89. (c) Capacity–voltage plot of Li-PBA, Na-PBA, and K-PBA systems, plotted using data from refs 87–89, 129–140.

### 2.3. Graphitic Carbon Anodes

Graphite and graphite-based materials are preferred anode materials for alkali-ion-based batteries because of their low cost. Whereas both Li and K intercalate in graphite, Na does not.<sup>151</sup> Several plausible arguments have been made to explain the lack of Na intercalation in graphite.<sup>158,159</sup> The ionic size of  $\text{Na}^+$  cannot play a determining role because it is in between that of  $\text{Li}^+$  and  $\text{K}^+$ , both of which form insertion compounds. In addition, graphite does not have much cohesion between the carbon planes,<sup>160</sup> making it easy for the structure to dilate to accommodate larger alkali ions. Hence, the origin of the inability to insert Na into graphite is unlikely to be related to the ionic size of Na, and more insight can be obtained from a basic thermodynamic analysis: The insertion energy is the summation of the ionization energy of the alkali metal and the insertion energy of the alkali ion and electron into the graphite. As an alkali ion has no substantial hybridization with carbon its insertion energy is almost purely electrostatic, making its energy contribution for each alkali similar. The same argument can be made for the electron insertion into the graphite states. Hence, the difference between  $\text{Li}^+$ ,  $\text{Na}^+$ , and  $\text{K}^+$  must arise from the ionization energy of the metal. Indeed, there is drastic drop in ionization energy for Na.<sup>158</sup> Therefore, the more plausible explanation for the positive formation energy (negative voltage) for  $\text{Na}^+$  insertion into graphite is due to the ionization energy of Na metal, not due to any size mismatch issues with  $\text{Na}^+$  in graphite. As a result, this problem is intrinsic and not easy to solve unless one can lower the electronic states in which the

electron is donated in order to compensate for the higher ionization energy of sodium.

While K can intercalate into graphite with reasonable capacity, it is still unclear if its cycling stability is suitable for practical applications. Capacity fade has been found to be significantly affected by the choice of binders and electrolytes.<sup>151–157</sup> As an illustration, Figure 10b presents two sets of data with approximately 200 cycles: the first group of data includes the same electrolyte (0.8 M  $\text{KPF}_6$  in EC/DEC(1:1)) with different binders, and the second group includes the same binder (Na alginate) with different electrolytes. As indicated in Figure 10b, both the binder and the electrolyte have a significant effect on the capacity and cycling stability of the K/graphite anode. A Na-alginate binder combined with 1 M  $\text{KPF}_6$  in EC/DEC (1:1) as the electrolyte resulted in capacity fade of more than 50% after 100 cycles. But when the same binder and salt is used in EC/DMC or EC/PC the capacity fading was less significant.

While not all the data for K/graphite is evaluated over 200 cycles, it nonetheless reveals interesting trends. Wu et al., used 0.8 M  $\text{KPF}_6$  in EC/DEC (1:1) to compare electrodes with either PVDF, NaCMC, and PAANa as binders in a 1:9 ratio with graphite. The electrode made with a PAANa binder showed superior behavior, retaining 97% of its original capacity after 50 cycles, whereas the other two electrodes retained less than 80% of the original capacity. Komaba et al.<sup>151</sup> confirmed PAANa's positive effect on capacity retention with a 1 M KFSI EC/DEC (1:1) electrolyte. These reports indicate that PAANa binder may be a superior choice over PVDF and CMC for K-graphite

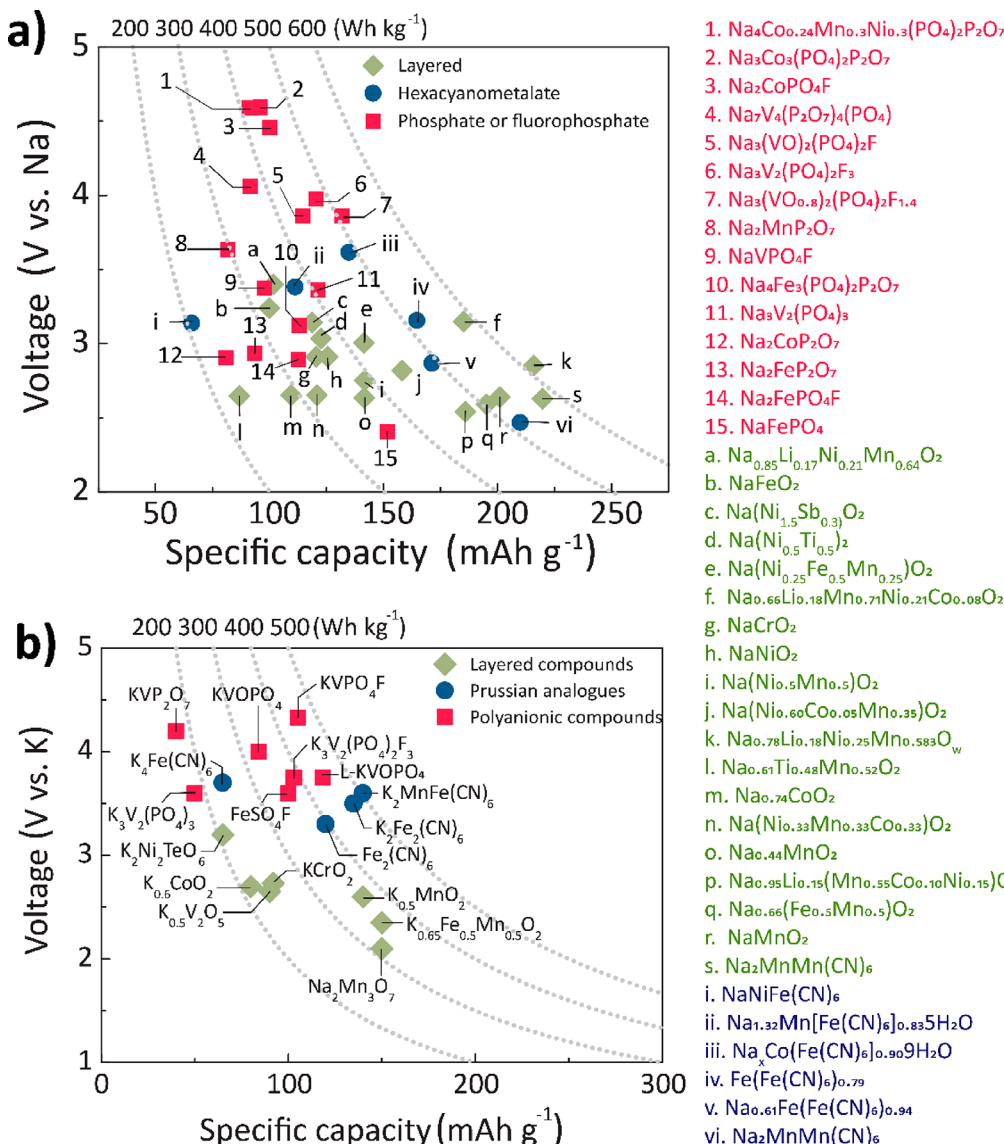


**Figure 9.** Classified cathode materials for (a) NIBs, reproduced with permission from ref 105. Copyright 2016 Springer Nature. (b) KIBs, plotted using data from refs 52,150.

electrodes and that graphite can exhibit a stable cycle life with the selection of an appropriate binder and electrolyte.

#### 2.4. Hard Carbon Anodes

**2.4.1. Effect of Synthesis Conditions on Electrochemical Properties of Hard Carbon Anodes.** Given that Na does not intercalate into graphite, hard carbon, which is a partially disordered carbon, has been used as an alternative anode for NIBs. State-of-the-art hard carbon can provide a reversible capacity of  $\sim 350 \text{ mAh g}^{-1}$ .<sup>161</sup> Both the capacity and voltage profile of the hard carbon are influenced by the synthesis conditions.<sup>161</sup> Figure 11 shows that the Na storage capacity increases as the synthesis temperature increases from 1000 to 2000 °C<sup>161</sup> but declines for carbons prepared at even higher temperature. The voltage profile also changes: at synthesis temperatures below 1000 °C, most of the capacity originates from the high-voltage part. With increasing temperature, the contribution of the low-voltage capacity gradually increases and becomes maximal at approximately 2000 °C, with the capacity between 280 and 300 mAh g<sup>-1</sup> originating from the low-voltage

plateau region (<0.1 V). Both the low-voltage capacity and overall capacity decrease at higher synthesis temperature.<sup>161–164</sup>

**2.4.2. Overview of Hard Carbon Structure Models and Na-Insertion.** Different structural models of hard carbon have been proposed, dating back to the 1970s. Before 2000,<sup>165–168</sup> models derived from transmission electron microscopy (TEM) described the hard carbon structure as consisting of graphene/graphite flakes with either curvature or cavities. A commonly used starting point of structural models is the “house of card” picture proposed in 2000 by Dahn et al.<sup>169</sup> In this model, hard carbon is described as a disordered stacking of defective graphite flakes with Na insertion into these domains responsible for the sloping voltage region in the voltage curve. Although this model has been widely adopted to understand the structure and electrochemical properties of hard carbon, there is no description of the nongraphitic structural features such as the curvature states and sp<sup>3</sup>-hybridized C–C bonds that are observed in hard carbon. Notably, there is no clear experimental evidence validating the “house of card” model, and the intercalation mechanism remains under debate.

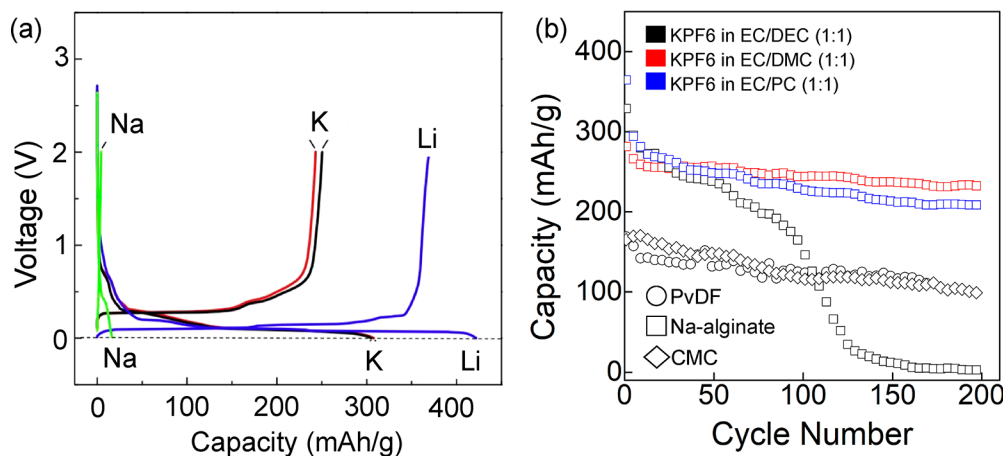


**Figure 10.** (a) Charge–discharge curves of graphite electrode with polyacrylate binder in 1 M  $\text{LiPF}_6/\text{EC:DMC}$  (1:1) for Li cell (blue line), 1 M  $\text{NaPF}_6/\text{EC:DEC}$  (1:1) for Na cell (green line), and 1 M KFSI EC:DEC (1:1) for K cell (red and black lines). A graphite composite electrode was formed on Cu foil (blue and black lines) and Al foil (red and green lines). Reproduced with permission from ref 151. Copyright 2015 Elsevier. (b) The effect of the binder and electrolyte on the capacity of graphite for KIB, plotted using data from refs 151–157. The shape and color of the marker are used to demonstrate the effect of the binder and electrolyte, respectively.

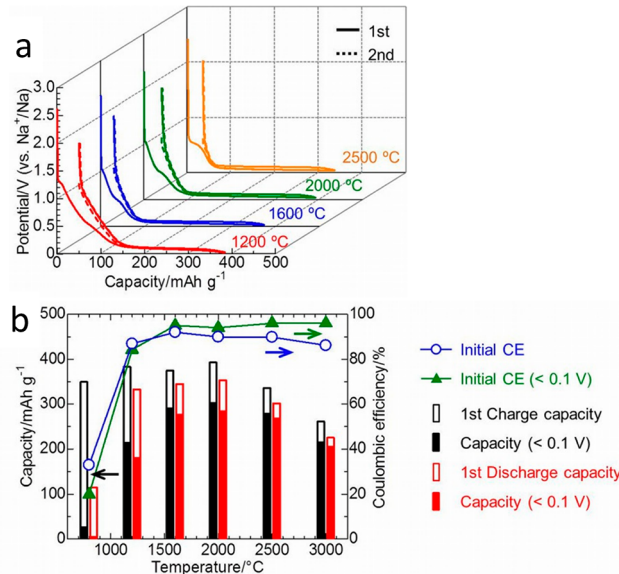


**Figure 11.** (a) Charge and discharge curves of carbon electrodes treated at 1200–2500 °C between 2.0 and 0.005 V (vs  $\text{Na}^+/\text{Na}$ ) at 20 mA g<sup>-1</sup>. (b) Charge and discharge capacities and initial CEs as a function of calcination temperature. Reproduced with permission from ref 161. Copyright 2015 Wiley.

Recently, with assistance from machine learning, Gray et al. proposed atomic models for hard carbon.<sup>170</sup> Two types of local structures were proposed for hard carbon. One structure consists of a distorted carbon framework connected with  $\text{sp}^3$ -hybridized C–C bonds and defects, which is proposed as the origin of the small pores in hard carbon. The other structure consists of a curved graphene sheet with 5–7 rings. This model better captures some of the main features believed to exist in hard carbon, such as the  $\text{sp}^3$  bonds, curvature, and subnanometer pores. However, limited by the computational scale and characterization capability, the distribution of these local structures and their effect on the electrochemical performance could not be determined.

It is widely accepted that the high-voltage part comes from Na adsorption in defects or Na insertion in graphitic regions and

that the micropore filling by Na clusters is responsible for the low-voltage region.<sup>171–173</sup> The formation of metallic Na clusters in hard carbon in the low-voltage plateau region has been demonstrated by nuclear magnetic resonance (NMR) spectroscopy and TEM characterization.<sup>174–176</sup> Although the similar lattice fringes of metallic Na and possible oxidized products (i.e.,  $\text{Na}_2\text{O}_2$  and  $\text{Na}_2\text{CO}_3$ ) in TEM makes it difficult to confidently assert the presence of Na metal, the metallic electronic state of Na in the low-voltage plateau region has been demonstrated with NMR, likely indicating metallic Na clustering at ~0.1 V.<sup>174,175</sup> Nevertheless, it remains unclear how small Na metal clusters can form at a positive voltage. Na metal formation should occur at <0 V when the cell overpotential and the small cluster size are considered. One can argue that the formation of Na metal clusters in hard carbon can be stabilized at positive voltage by the Na–C interaction, but this argument is not consistent with the computational work by Yoon et al., who found that Na metal is not stabilized on the carbon surface.<sup>159</sup> Clearly, understanding of the Na storage mechanism in hard carbon remains incomplete, thereby warranting further investigation to optimize the performance of hard carbon anodes.

## 2.5. Low-Voltage Intercalation Anodes

Noncarbon intercalation compounds have also been investigated as alternative anodes for NIBs and KIBs. Figure 12a summarizes the capacity of the materials whose average voltage is below 1 V vs  $\text{Na}/\text{Na}^+$  or  $\text{K}/\text{K}^+$ .<sup>177–185</sup> So far, most of the intercalation-based anodes offer no energy advantage over graphite anodes (for K) and hard carbon anodes (for Na) because of their relatively low volumetric capacity and high voltage. Only a few compounds (i.e.,  $\text{Li}_4\text{Ti}_5\text{O}_{12}$ ,  $\text{Na}_2\text{Ti}_3\text{O}_7$ ,  $\text{K}_2\text{Ti}_8\text{O}_{12}$ ,  $\text{K}_2\text{V}_3\text{O}_8$ , and  $\text{Nb}_2\text{O}_5$ ) have higher volumetric capacities than graphite (for K) and hard carbon (for Na) but their higher Na and K intercalation voltages ultimately reduce the energy density of a full cell.  $\text{Na}_2\text{Ti}_3\text{O}_7$  is the only exception because it can intercalate two Na ions delivering a reversible capacity of ~180 mAh g<sup>-1</sup> (~617 mAh cm<sup>-3</sup>) at a low voltage of ~0.3 V (vs  $\text{Na}/\text{Na}^+$ ).<sup>185</sup> Xu et al. used first-principles calculations to argue that the low voltage originates from the low Na-ion coordination (6 in  $\text{Na}_4\text{Ti}_3\text{O}_7$  vs 7–9 in  $\text{Na}_2\text{Ti}_3\text{O}_7$ ) and the shearing of Ti–O slabs in the  $\text{Na}_4\text{Ti}_3\text{O}_7$  structure.<sup>115</sup>

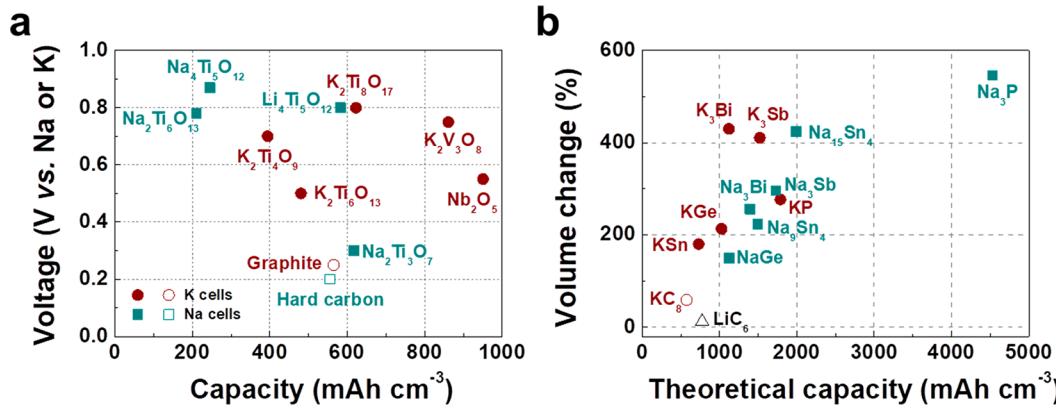


**Figure 12.** (a) Capacity–voltage plot of intercalation-based anode materials for NIBs and KIBs using data from refs 177–185. (b) Theoretical capacity vs volume change of alloy anodes. The volumetric capacity was calculated using the density of the crystal structure.

While current insertion anodes cannot compete with graphite and hard carbon anodes, there is no fundamental reason that limits the capacity and lower voltage of insertion materials, warranting further efforts to search for alternative Na and K intercalation anodes.

## 2.6. Alloying Reaction Anodes

High theoretical capacity compounds based on alloying reactions have attracted significant attention as anodes for LIBs. For example, silicon has a theoretical capacity of ~4200 mAh g<sup>-1</sup> (~4956 mAh cm<sup>-3</sup>), forming Li<sub>4.4</sub>Si and a low voltage of ~0.2 V (vs Li).<sup>18</sup> However, Si is not a good candidate for NIB and KIB anodes because of the low solubility of Na and K in Si, which would result in low capacity.<sup>186</sup> Tin (Sn), antimony (Sb), and phosphorus (P) have been proposed as alternative high-capacity anodes for NIBs and KIBs.<sup>187–191</sup> Nonetheless, K-alloying compounds have in general lower capacity and higher average voltage than their Na counterparts. For example, the P anode delivers a reversible capacity of ~1800 mAh g<sup>-1</sup> (~3204 mAh cm<sup>-3</sup>) at an average voltage of 0.45 V (vs Na), forming Na<sub>3</sub>P,<sup>187</sup> but P can react with only one K ion to form KP, exhibiting a reversible capacity of ~850 mAh g<sup>-1</sup> (~1793 mAh cm<sup>-3</sup>) with a relatively high average voltage of ~0.7 V (vs K).<sup>188,192</sup> Similarly, while Sn can form a Na-rich alloy compound (Na<sub>15</sub>Sn<sub>4</sub> with theoretical capacity: 830 and 1992 mAh cm<sup>-3</sup>).<sup>167,168</sup> Sn can only accommodate a single K, forming KSn, for which the theoretical capacity is only 221 mAh g<sup>-1</sup> (731 mAh cm<sup>-3</sup>).<sup>191</sup> These results indicate that alloying reaction compounds are less attractive for KIB than for NIB.

While some alloying reaction anodes may have an energy density benefit because of their higher capacity compared with hard carbon (for Na) and graphite (for K), the large volume change of alloying anodes upon cycling causes electrode pulverization and loss of electronic contact with the current collector and thus rapid capacity fading. Figure 12b shows the volume change of alloying anodes and compares them with that of graphite anodes in K and Li systems. The volume change was calculated from the crystal density of materials in the ICSD inorganic crystal structure database. All the alloying reaction anodes suffer from much larger volume change (>150%) than graphite (~59% for K and ~13% for Li). To accommodate such a large volume change, it is necessary to fabricate nanostructures and/or carbon composites, which would significantly decrease the volumetric energy density and possibly increase the manufacturing cost of the cell. Indeed, if the capacity of a composite electrode is limited by the maximal volume expansion

that can be tolerated in an electrode, rather than by the theoretical capacity of the electrode material, one can argue that alloying electrodes are not beneficial to increase the energy density of Na-ion batteries.<sup>193,194</sup> Applying this argument for K-alloying would lead to an even more negative evaluation of alloying electrodes for KIB.

## 2.7. Outlook for Na/K-ion Batteries

Na-ion batteries have some potential to reduce the cost for grid energy storage, in particular as their cathodes may have less reliance on Ni and Co. Potential cathode materials can be found from layered oxides as well as polyanion compounds. In a layered mixed metal systems, the cathode energy density can exceed 500 Wh kg<sup>-1</sup> with reasonable capacity retention,<sup>47,63,65,77,195</sup> although the strong Na–Na interaction creates a more sloped voltage profile,<sup>52,114,194</sup> which will be difficult to circumvent and may have to be managed in applications. It is not clear how much further improvement can be expected from layered Na-ion cathodes, justifying a more comprehensive evaluation of polyanion compounds. Recent research indicates that NASICON materials based on earth-abundant Mn show some promise. For instance, Na<sub>3</sub>MnTi(PO<sub>4</sub>)<sub>3</sub> realizes reversible intercalation of almost three Na, yielding a comparable energy density of ~470 Wh kg<sup>-1</sup>.<sup>196</sup> So far, only hard carbon has emerged as a viable anode for Na-ion systems. Cyclability of these anodes is highly dependent on appropriate choices of binders and electrolytes. Current and previous reviews of the literature on low voltage intercalation compounds<sup>52,186,197,198</sup> indicate that there is not yet a true competitor for hard carbon, but research has not nearly been as extensive as for cathode materials.

The alkali-ion interaction that creates the steep voltage slope in layered Na-ion compounds is even more severe for layered K-ion compounds, making them unlikely to be viable cathode materials for KIB. Hence, the search for K-ion cathodes should be directed toward polyanion and other more novel compound classes. Some polyanion compounds have shown high voltage and good capacity retention, but considerably more exploration of K-ion cathodes is needed. While graphite is a functioning anode for K, it may not have the capacity to create reasonable full cells, and some effort is needed to find alternative anodes.

If one is willing to sacrifice the volumetric energy density, Prussian blue compounds appear particularly attractive for both Na and K-ion batteries. Many PBAs only use inexpensive Mn and Fe, can be water processed, and deliver high specific energy (as high as ~490 Wh kg<sup>-1</sup>).<sup>88</sup> Considering that the most

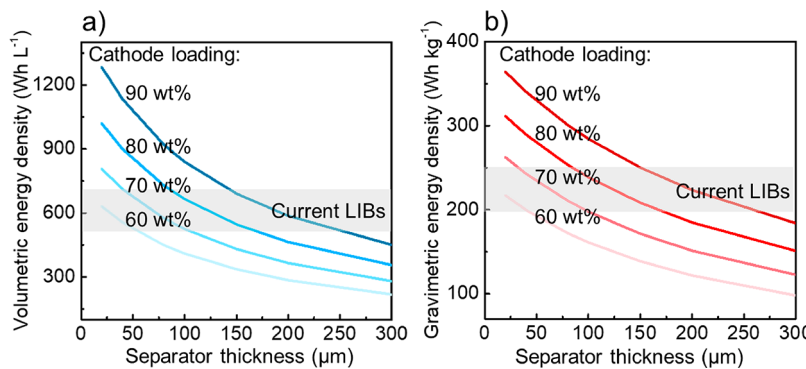


**Figure 13.** Estimated cell-level (a) volumetric and (b) gravimetric energy density for ASSB utilizing Li metal anode with different cathode loadings and separator thicknesses compared with those of current LIBs. The model uses NMC622 as the cathode, 20% excess Li metal as the anode, and LPS as the SE. Details of the model are described in the Supporting Information, *Supplemental Note S1*.

important aspect of NIBs and KIBs is the reduction of material cost, PBAs based on inexpensive elements are of significant interest. But the relation between their chemistry, processing, water content, and electrochemical properties needs further clarification.

Because  $\text{Na}^+$  and  $\text{K}^+$  are much larger than  $\text{Li}^+$ , their electrodes will generally undergo larger volume changes for a comparable capacity cycled. Their advancement would therefore benefit greatly from the development of alternative electrode and cell architectures that can accommodate larger volume changes of the electrodes.

Finally, while most focus in solid-state batteries is focused on lithium chemistries, the availability of several good Na-ion conducting solid electrolytes creates the possibility of solid-state Na batteries. Na metal is very soft and deformable, creating the possibility that only mild stack pressure is required to keep contact between the metal anode and the solid electrolyte. In addition, the less reductive potential of  $\text{Na}/\text{Na}^+$  creates somewhat less stringent chemical requirements for thermodynamic stability of the solid conductor against the metal anode.<sup>199</sup> However, the low melting point of Na metal ( $98^\circ\text{C}$ ) will require that a Na metal solid-state battery is well protected against thermal excursions. Because research into Na (or K) metal solid-state batteries is very limited, we focus on the next section solely on Li solid-state systems, but several of the challenges encountered with lithium will also be relevant for solid-state batteries with other alkalis.

### 3. ALL-SOLID-STATE BATTERIES

#### 3.1. Opportunities for Solid-State Batteries

Solid-state batteries (ASSBs), in which a solid ionic conductor is used as an electrolyte to transport working ions between the anode and cathode, have been proposed as an important advance in energy storage, driven by the numerous fast solid ionic conductors that have been discovered.<sup>200,201</sup> Several major automotive companies have even targeted the mid-2020s to begin using ASSBs in EVs<sup>202–204</sup> although it remains to be seen whether such aggressive targets can be met in practice.

Besides functioning as a separator between the anode and cathode, the solid electrolyte (SE) is also added to the cathode to provide ionic pathways to the cathode particles unless hybrid electrolytes are used.<sup>205–208</sup> Current SEs can be divided into two categories: organic and inorganic SEs. The recent advances and remaining challenges for the organic SEs have been extensively reviewed.<sup>209,210</sup> Although organic SEs are mechanically soft and

can better accommodate the electrode volume change, their low ionic conductivity limits the power density at room temperature. In this section, we will therefore mainly focus on recent research progress in ASSBs that use an inorganic SE.

The potential for improved safety is one of the most significant advantages of ASSBs over current LIBs. A major concern for current LIBs is the flammability of the carbonate-based organic liquid electrolyte. When thermal runaway occurs as a result of electrical or mechanical abuse, the liquid electrolyte participates in a rapid exothermic reaction which can lead to fire or explosion. Several widely publicized safety incidents involving both consumer electronics and EVs have focused attention on the safety of LIBs.<sup>211,212</sup> ASSBs mitigate these risks by replacing the flammable carbonate-based organic liquid electrolyte with an inorganic SE. This inherent safety makes ASSBs much more attractive for consumer electronics and EV applications than LIBs and other potential beyond-LIB systems that employ organic liquid electrolytes.

ASSBs are also believed to be a pathway toward higher energy density than LIBs because the solid-state separator may enable the use of a lithium metal anode which has a theoretical specific capacity of  $3860 \text{ mAh g}^{-1}$ . Despite decades of efforts, it is still not possible to integrate metallic Li anodes in liquid-electrolyte cells without compromising cycle life and/or safety.<sup>213</sup> Although Li metal penetration through the solid electrolyte has been observed in ASSBs under high-current-density cycling conditions,<sup>214,215</sup> their inherent nonflammability would prevent catastrophic failure in the event of a short circuit. Figure 13 shows the estimated volumetric and gravimetric energy density for ASSBs utilizing a NMC622 cathode,  $\text{Li}_3\text{PS}_4$  (LPS) SE, and Li metal anode. With a high cathode loading (>80 wt % active material in the cathode composite) and a thin separator (<50  $\mu\text{m}$ ), ASSBs can have a significant energy density advantage over current LIBs, particularly in terms of volumetric energy density. ASSBs also allow bipolar electrode stacking cell design, which can reduce the overall current collector thickness as well as the “dead volume” between cells.<sup>206</sup>

Several SEs with ionic conductivities higher than those of current liquid electrolytes ( $\sim 10 \text{ mS cm}^{-1}$ ) have been reported (e.g.,  $25 \text{ mS cm}^{-1}$  for  $\text{Li}_{0.54}\text{Si}_{1.74}\text{P}_{1.44}\text{S}_{11.7}\text{Cl}_{0.3}$ <sup>206</sup> and  $12 \text{ mS cm}^{-1}$  for  $\text{Li}_{10}\text{GeP}_2\text{S}_{12}$ <sup>216</sup>), and some ASSBs have been shown to exhibit very high rate capability,<sup>206</sup> although all the transport limitations that can occur in ASSBs are not fully characterized. Improving the ionic conductivity of the electrolyte reduces the Li transport resistance and can lower the cell overpotential under high current density. In addition, high ionic conductivity

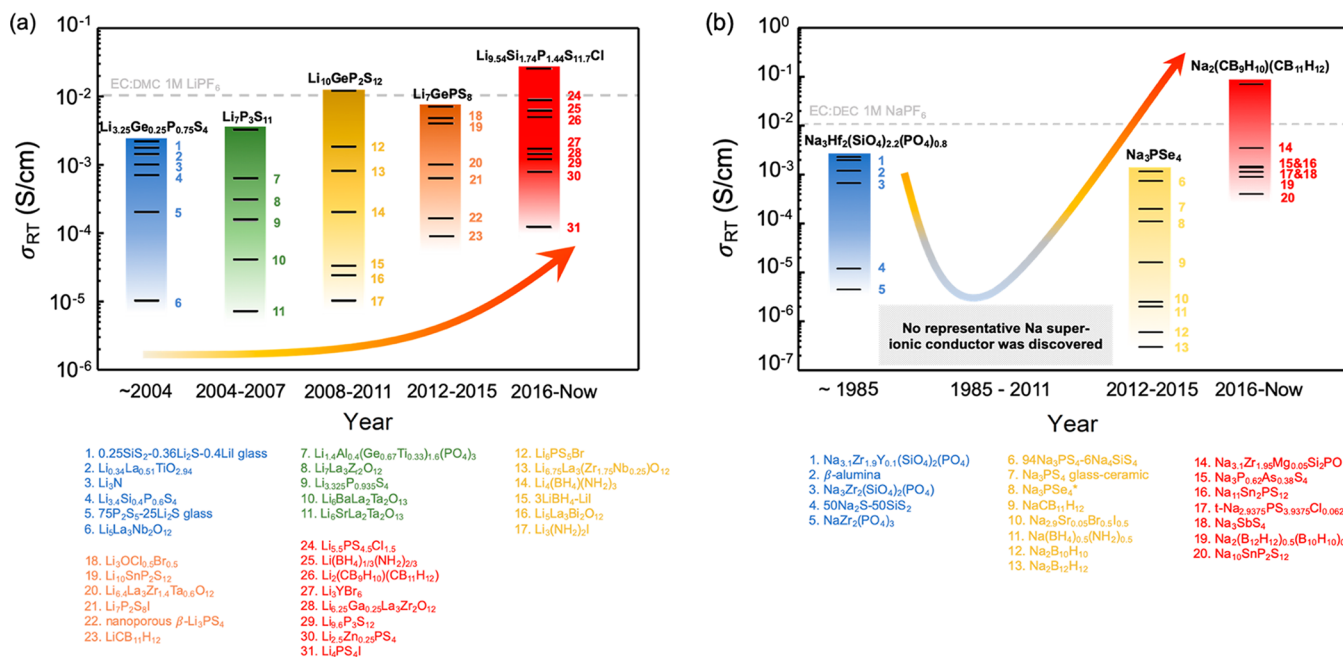


**Figure 14.** Progress in discovery of fast (a) Li-ion conductors and (b) Na-ion conductors. The room temperature ionic conductivity of representative conductors over time is plotted to demonstrate the improvement in ionic conductivity.

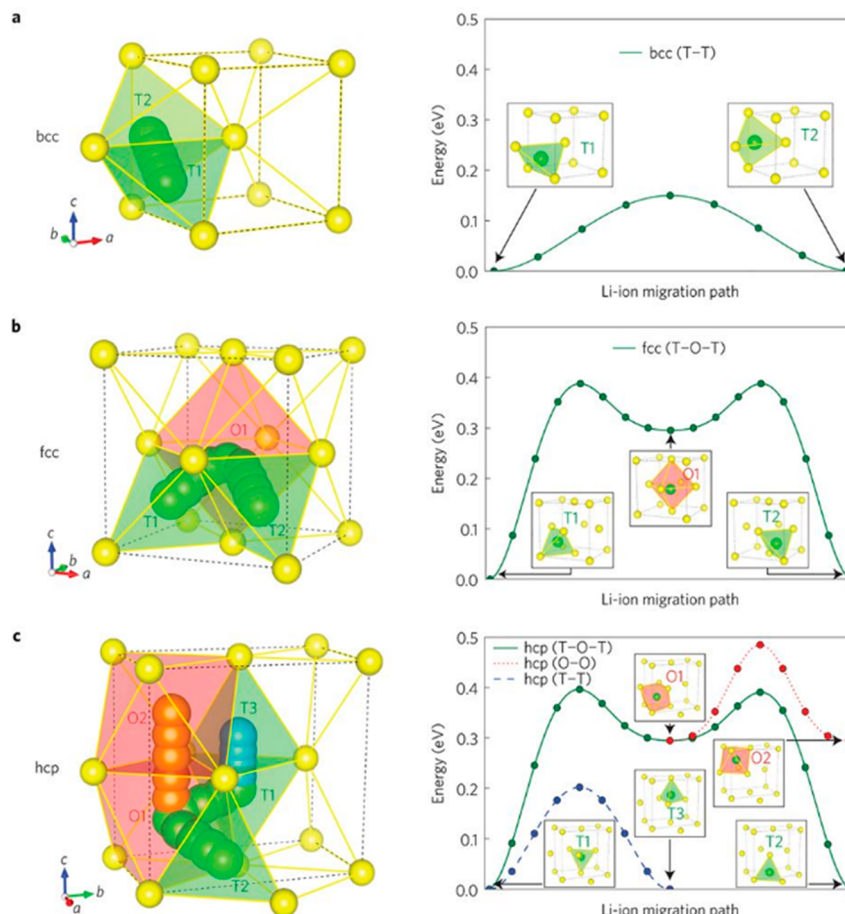


**Figure 15.** Li-ion migration path (left panels) and calculated energy path (right panels) in (a) bcc, (b) fcc, and (c) hcp sulfur anion lattices. The sulfur anions are colored yellow, and the Li ions are colored green, blue, and red for different paths. LiS<sub>4</sub> tetrahedra and LiS<sub>6</sub> octahedra are colored green and red, respectively. Reproduced with permission from ref 218. Copyright 2015 Springer Nature.

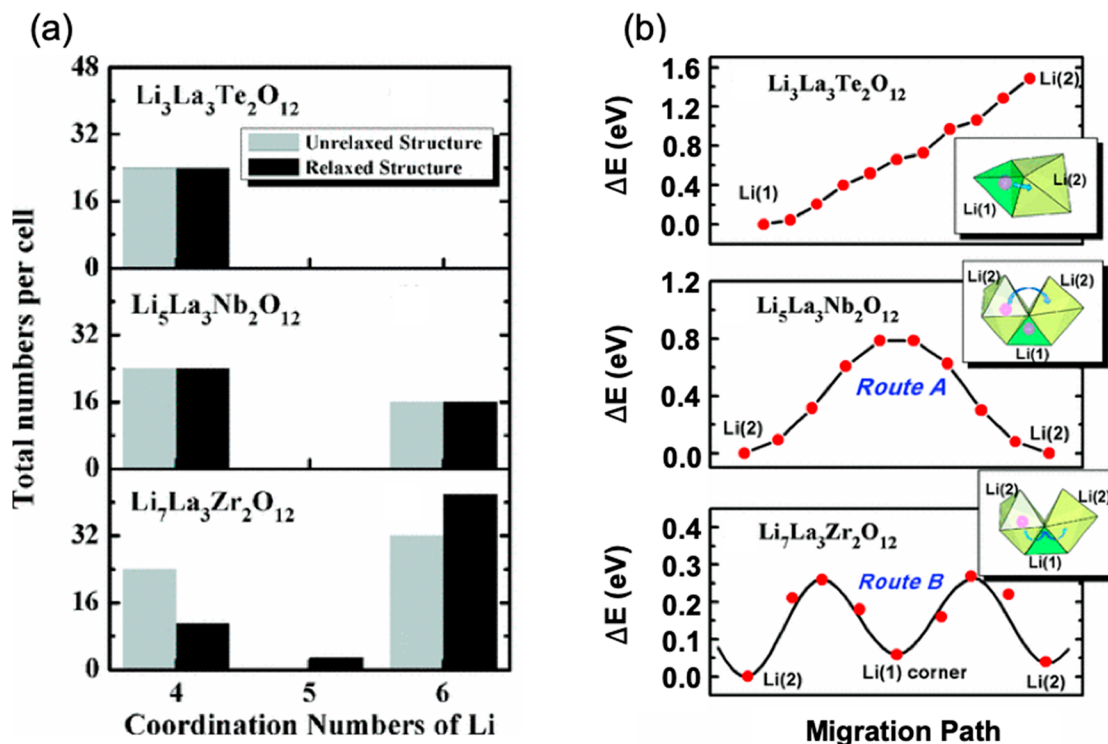


**Figure 16.** (a) Coordination numbers (CNs) of Li ions in  $\text{Li}_3\text{La}_3\text{Te}_2\text{O}_{12}$ ,  $\text{Li}_5\text{La}_3\text{Nb}_2\text{O}_{12}$ , and  $\text{Li}_7\text{La}_3\text{Zr}_2\text{O}_{12}$ . CN = 4, 5, 6 represent Li ions that are inside tetrahedral sites [Li(1) sites], near the tetrahedral–octahedral borders [Li(1)–Li(2) borders], and inside octahedral sites [Li(2) sites], respectively. (b) Energy barrier plots of Li-ion migration in  $\text{Li}_3\text{La}_3\text{Te}_2\text{O}_{12}$ ,  $\text{Li}_5\text{La}_3\text{Nb}_2\text{O}_{12}$ , and  $\text{Li}_7\text{La}_3\text{Zr}_2\text{O}_{12}$ . Reproduced with permission from ref 284. Copyright 2012 American Physical Society (APS).

has been shown to limit pressure build up in the SE and may therefore favorably influence resistance against Li penetration.<sup>217</sup> More superionic conductors are likely to be discovered given the improved understanding of alkali-ion conductivity<sup>218–223</sup> and the large number of discovery projects going on worldwide.<sup>224–229</sup>

### 3.2. Accelerated Development of Fast Ion Conductors

Parts a and b of Figure 14 show the recent progress made in Li and Na-ion conductors. The ionic conductivity of many of these conductors, such as garnet-type materials, argyrodite-type materials, and LISICON materials, approaches or even surpasses that of currently used liquid electrolytes ( $\sim 10^{-2} \text{ S cm}^{-1}$ ).<sup>206,216,230–261</sup> Although fast Na-ion conductors such as  $\beta\text{-Al}_2\text{O}_3$  and NASICON-type materials predate many of the recent Li-ion conductors,<sup>262–266</sup> the discovery of novel Na-ion conductors stagnated until 2012 when several novel Na-ion conductors were derived from their Li counterparts. Very high ionic conductivities up to  $70 \text{ mS cm}^{-1}$  have now been demonstrated.<sup>226,248,249,267–279</sup> Although ionic conductors using working ions other than Li or Na (such as Mg) have been investigated,<sup>280,281</sup> none of these materials have achieved high enough ionic conductivity for room-temperature ASSB applications.

While a complete understanding of superionic conductivity is not yet available, some factors that enable high cation conductivity have been established. In general, a flat energy landscape, where the displacement of the working ion only causes a small change in structure energy, is beneficial to create a low activation energy. One way to flatten the energy landscape is to keep the coordination changes along the diffusion path minimal. Wang et al. used this argument to rationalize why body-centered cubic (bcc)-like anion frameworks, where Li can

directly hop between adjacent tetrahedral sites, tend to have lower activation energy for cation motion than other close-packed frameworks, where Li must hop along a tetrahedral–octahedral–tetrahedral path (Figure 15).<sup>218</sup> Many sulfide superionic conductors with low activation energy, such as  $\text{Li}_2\text{P}_3\text{S}_{11}$  and  $\text{Li}_{10}\text{GeP}_2\text{S}_{12}$ , indeed have a bcc anion framework.

The screening power of the anion strongly affects the cation mobility. For materials with the same structure but different anion species, such as the argyrodite-type materials  $\text{Li}_6\text{PO}_5\text{Cl}$  and  $\text{Li}_6\text{PS}_5\text{Cl}$ , sulfides usually exhibit higher ionic conductivities than oxides.<sup>235</sup> This can be understood because the larger and more polarizable sulfur anions better screen the interaction between cations in the structural framework (such as the  $\text{P}^{5+}$  in  $\text{PS}_4^{3-}$ ) and the migrating cation ( $\text{Li}^+$  or  $\text{Na}^+$ ). It seems that for many systems, replacing a monatomic anion with a polyanion also improves conductivity. This may be because the higher degree of freedom of a polyanion provides another way to screen the moving ion and flatten the energy landscape. For example, the ionic conductivity of sodium antiperovskite  $\text{Na}_3\text{OX}$  ( $\text{X} = \text{Cl}$ , Br, I, etc.) can be increased by 4 orders of magnitude by substituting the halide anion with the  $\text{BH}_4^-$  group.<sup>282</sup>

Depending on the transport mechanism, the cation vacancy and interstitial defect concentration can be another important factor in determining the ionic conductivity of materials. This defect concentration can usually be tuned by aliovalent doping. For example, Ca doping can be used to create Na vacancies in cubic  $\text{Na}_3\text{PS}_4$  to obtain a room-temperature ionic conductivity of  $\sim 1 \text{ mS cm}^{-1}$ <sup>283</sup> and Zr doping has been reported to increase the ionic conductivity of  $\text{LiTaSiO}_5$  by introducing interstitial Li ions.<sup>224</sup> While the effect of carrier concentration on the ionic conductivity can be well understood from dilute diffusion theory, some superionic conductors show a more unusual

dependence of conductivity on carrier concentration. It appears that in some materials with very high Li content, the structure becomes very cation-crowded, pushing Li into high energy sites. Such “Li-stuffed” materials have a lower activation barrier for Li motion as the ion is already in a high energy position. For example, the well-known garnet-type ionic conductor  $\text{Li}_7\text{La}_3\text{Zr}_2\text{O}_{12}$  exhibits a ionic conductivity of  $0.3 \text{ mS cm}^{-1}$ , whereas materials with the same garnet-type structure but lower Li concentrations,  $\text{Li}_5\text{La}_3\text{Nb}_2\text{O}_{12}$  and  $\text{Li}_3\text{La}_3\text{Te}_2\text{O}_{12}$ , exhibit much lower ionic conductivities. As shown in Figure 16a, as the Li concentration increases from  $x = 3$  to  $x = 7$  in a garnet-type  $\text{Li}_x\text{La}_3\text{M}_2\text{O}_{12}$  ( $\text{M} = \text{Te}, \text{Nb}, \text{Zr}$ ), more Li ions are pushed to the high-energy octahedral sites to minimize the interaction between adjacent Li ions.<sup>284</sup> As a result of the higher Li site energy, the energy barrier along the Li diffusion path is greatly lowered with higher Li content (Figure 16b).<sup>284</sup> In addition, Mo and co-workers argued that the strong mobile-ion interaction resulting from their high concentration can lead to multi-ion correlated migration with a reduced migration energy barrier.<sup>222</sup> These Li-excess or “Li-stuffed” materials provide a new route for the design of superionic conductors.

While no complete theory of superionic conductivity is available, many factors that favor high Li mobility have clearly been identified. These ideas can assist in the more rapid experimental or computational discovery of fast ion conductors,<sup>224–228</sup> making it likely that new fast ion conductors will surface in the coming years. However, for a fast ion conductor to function well as a solid electrolyte, other properties also need to be optimized and should be considered in future materials design exercises. As we will discuss in the following section, both the chemical and mechanical properties of the SE are also crucial for ensuring the stable cycling of ASSBs.

### 3.3. Challenges Facing ASSBs

Even with the availability of several possible excellent ionic conductors, realizing high-energy-density ASSBs with long cycle life must overcome several other scientific and engineering issues, as shown in Figure 17. These challenges include chemical, mechanical, and processing issues. Many SEs decompose or react with cathode active materials when charged to high voltage or upon cosintering at high temperatures.<sup>285,286</sup> In addition, contact loss between the cathode and SE can occur due to cycling-induced volume changes of the cathode material.<sup>287,288</sup> The use of a Li metal anode results in additional issues of contact

loss during plating/stripping, possible interfacial reactions, and Li propagation through the conductor.<sup>214,215,217,289</sup> Most of these mechanical and chemical interfacial instabilities increase the overpotential, resulting in lower energy density and capacity fade. Finally, practical cells will also require very thin SE separators that are easily processed and handled, and high cathode loading, which are issues that have only been partially addressed so far by the scientific community.<sup>208,290–295</sup>

**3.3.1. Intrinsic Stability of SEs.** The electrochemical stability window of SEs is crucial because it limits the operating voltage of the cell. During cell cycling, the SE experiences different Li/Na chemical potentials at various interfaces (e.g., Li metal anode, current collector, conductive carbon additives, electronically conductive cathode). Because Li or Na ions are very mobile in the SE, the SE readily decomposes at these interfaces when the applied Li/Na chemical potential exceeds their cathodic/anodic stability limits in the conductor, generating decomposition products with poor ionic conductivity.<sup>225,285,286</sup> While early claims of very high anodic stability were made for some SEs; it is now clear that many conductors are not intrinsically stable against the cathode and/or anode. Limited reaction rates may make such instabilities difficult to see with conventional experimental techniques, but they are nonetheless important for evaluating the long-time cycle life of solid-state batteries. For example, in the conventional semiblocking planar electrode setup for cyclic voltammetry (CV) measurements, the contact between the conductor and the electron source is much smaller than in a composite cathode architecture, leading to a very small current signal in CV scans. This led to a significant overestimation of the stability windows of  $\text{Li}_{10}\text{GeP}_2\text{S}_{12}$  (LGPS) (i.e., 0–5 V),<sup>216</sup> LPS,<sup>245,296,297</sup>  $\text{Na}_3\text{PS}_4$ ,<sup>273</sup> and  $\text{Li}_7\text{La}_3\text{Zr}_2\text{O}_{12}$  (LLZO).<sup>241,298–300</sup> In contrast, a more accurate stability window can be experimentally determined by mixing electronic conductors (such as carbon) with the conductor, thereby providing a sufficiently large reaction front over which electrons are provided. When this approach was applied, the reduction of LGPS was observed to start at 1.6 V against Li metal, and its oxidation was observed at 2.7 V,<sup>286,301</sup> consistent with theoretical calculations.

High-throughput density functional theory (DFT) calculations have enabled large-scale computational screening of electrolyte stability, with the findings showing good agreement with experimental results in most cases.<sup>224,225</sup> The calculated stability windows in Figure 18 indicate the oxidation and reduction limits of selected conductors representing different material families. It is clear that the stability of a SE strongly depends on the material chemistry. Currently, there is no fast ion conductor that possesses both high oxidation and low reduction limits.

**3.3.1.1. General Trends in Electrochemical Stability of SEs.** The combination of experiments and first-principles calculations has led to a better understanding of the stability of conductors in different chemistries. The decomposition of a SE requires the extraction (oxidation) or insertion (reduction) of electrons. The highest occupied electron state is therefore an important factor in setting the oxidation limit of the ion conductor (i.e., electrons at the valence band maximum in Figure 19a). Because an ionic conductor usually has no metal valence electrons in order to minimize electron conductivity, the oxidation limit is typically controlled by the anion state. Figure 19b,c shows the calculated oxidation stabilities of various ternary compounds with different anion chemistries.<sup>302</sup> Not surprisingly, fluorides exhibit high oxidation stability because of the high electronegativity of the  $\text{F}^-$

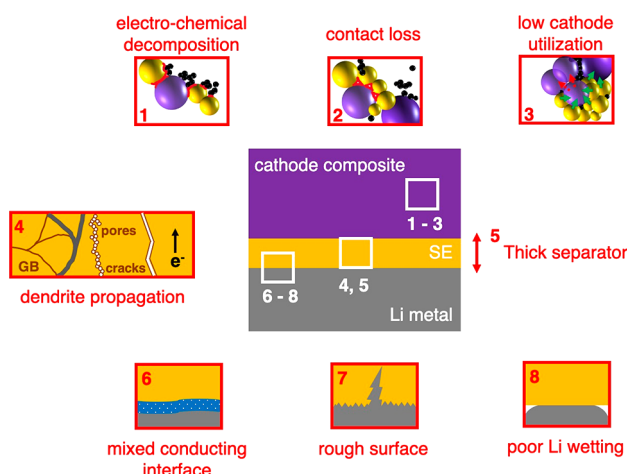
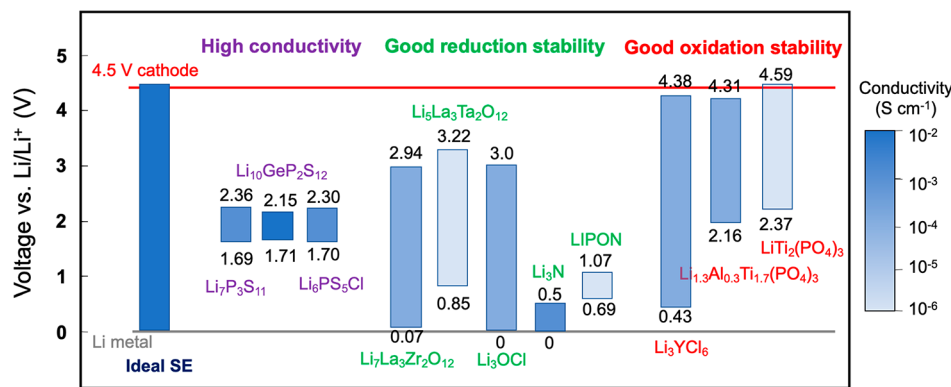
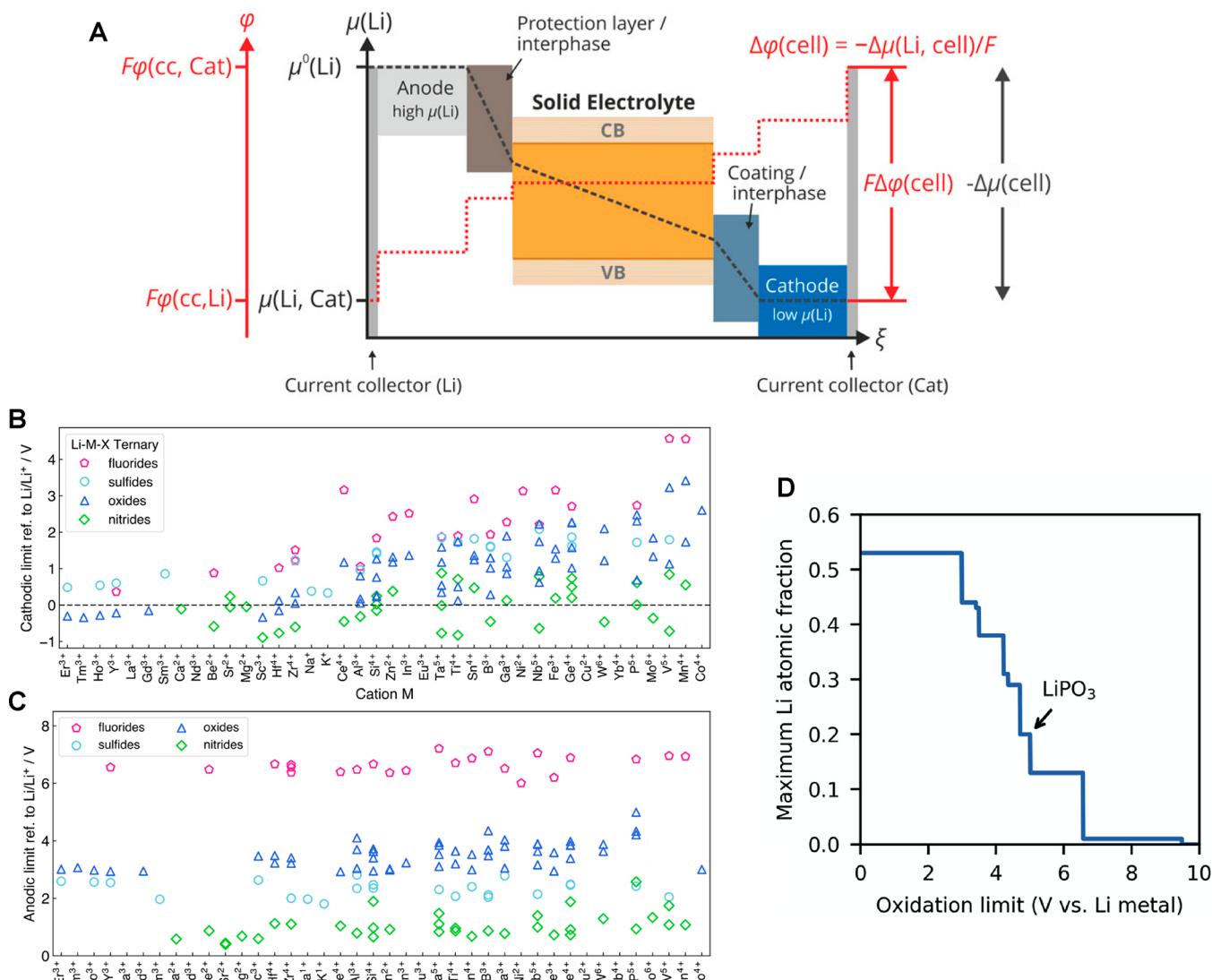


Figure 17. Schematic illustration of the major issues in ASSB.



**Figure 18.** Ionic conductivity of selected conductors and the corresponding calculated oxidation and reduction limits. An ideal SE (shown as the bar on the left side) should present ionic conductivity higher than  $10^{-2}$  S cm<sup>-1</sup> (conductivity of typical liquid electrolytes), stability with Li metal anode, and wide stability window that spans the full cycling voltage range.



**Figure 19.** (a) Potential profile in an ASSB cell. VB stands for valence band, and CB stands for conduction band. The variables  $\mu$  and  $\phi$  are the chemical potential of lithium (as a neutral component, in black) and the electric potential (in red), respectively. Reproduced with permission from ref 306. Copyright 2019 Wiley. (b,c) Cathodic and anodic limits for selected Li–M–X ternary compounds ( $M$  = cations presented in the figure,  $X$  = N, O, S, or F). Reproduced with permission from ref 302. Copyright 2017 Wiley. (d) Maximum Li atomic fraction versus oxidation limit for the 411 selected polyanionic oxides. A point ( $x$  and  $y$ ) in the profile means that all polyanionic oxides with an oxidation limit of  $x$  or higher have a maximum Li atomic fraction of  $y$ . LiPO<sub>3</sub> exhibits the advantages of excellent high-voltage stability and a low migration barrier and thus is marked by the black arrows. Reproduced with permission from ref 303. Copyright 2019 Elsevier.

ion. High oxidation limits have also been reported for polyanionic oxide materials in which the strong covalency of oxygen with the nonmetal cation(s) in the polyanion leads to a decrease in the energy of  $O^{2-}$  states and protects them from oxidation.<sup>303</sup> Such hybridization protection of the oxygen ion is one of the most important tools available to create coatings or conductors with good anodic stability.<sup>303,304</sup> Sulfides, however, usually exhibit poor stability against oxidation, consistent with the more facile oxidation of the  $S^{2-}$  ion. Thus, the incorporation of a sulfide SE in a composite cathode that needs to be charged to high voltage faces great challenges. For example, a much lower Coulombic efficiency was observed in ASSBs using a LPS electrolyte than in liquid cells using a  $LiNi_{0.8}Mn_{0.1}Co_{0.1}O_2$  (NMC811) cathode,<sup>287</sup> which is related to the irreversible decomposition of sulfides when charged above their oxidation limit. In cathode composites with a LGPS electrolyte, the accumulation of highly oxidized sulfur species was observed upon introducing carbon in the composite, leading to a large interfacial charge-transfer resistance and aggravated capacity fading.<sup>305</sup>

The Li content also plays a role in determining the stability window of a conductor. A high concentration of Li in the structure usually results in a high Li chemical potential. Such “Li-stuffed” materials are thus more susceptible to Li extraction and exhibit a low stability against oxidation. This can be systematically observed in polyanionic oxides where increasing the Li atomic fraction significantly decreases the oxidation limit (Figure 19d). Given that a low Li fraction in turn indicates a large Li migration distance, which negatively affects the ionic conductivity, a trade-off between conductivity and oxidation stability of solid conductors must be considered in the design of new conductors.<sup>303</sup>

The stability against the reduction of a conductor (or any alkali-containing compound) is mostly controlled by the presence of nonalkali reducible cation(s). In general, compounds containing late-transition-metal cations exhibit worse stability against reduction than those without these cations, whereas a low reduction limit can be observed in conductors containing alkali, alkali-earth, and lanthanide cations. For example, as shown in Figure 19b,  $LiYF_4$  is predicted to be reduced at 0.364 V against Li metal as opposed to  $Li_2NiF_4$ , which can be reduced at 3.130 V. This explains the unique stability of some of the antiperovskites, such as  $Li_3OCl$ ,  $Li_3SBF_4$  and  $Na_2BH_4NH_2$ , because they contain no reducible cations. But this lack of cations to protect the anions through the hybridization mechanism explained previously leads to very poor intrinsic anodic stability. The presumed intrinsic stability of LLZO against Li metal is consistent with it only containing La and Zr as non-Li metals.

Even though the anion in the SE does not usually change valence in a reduction process against the anode, anion chemistry can indirectly affect the cathodic stability of SEs. In particular, nitride anions have been shown to be highly beneficial by stabilizing some metal ions to a lower potential against reduction. In addition, even when they decompose, they often form nitrides that passivate Li metal.<sup>302</sup> Upon reduction with lithium ternary nitrides  $Li-M-N$  more often create electronically insulating products in contrast to the metallic  $Li-M$  compounds that are usually generated upon lithiation of the  $Li-M-X$  systems when  $X$  is one of the other anion chemistries. For example, as shown in Figure 20d, the lithiation of the  $Li-Al-N$  compound ( $Li_3AlN_2$ ) results in passivating products ( $Li_3N$ ,  $AlN$ , or  $Li_3AlN_2$ ), as opposed to other  $Li-Al-X$  ( $X = F, O, S$ ) system

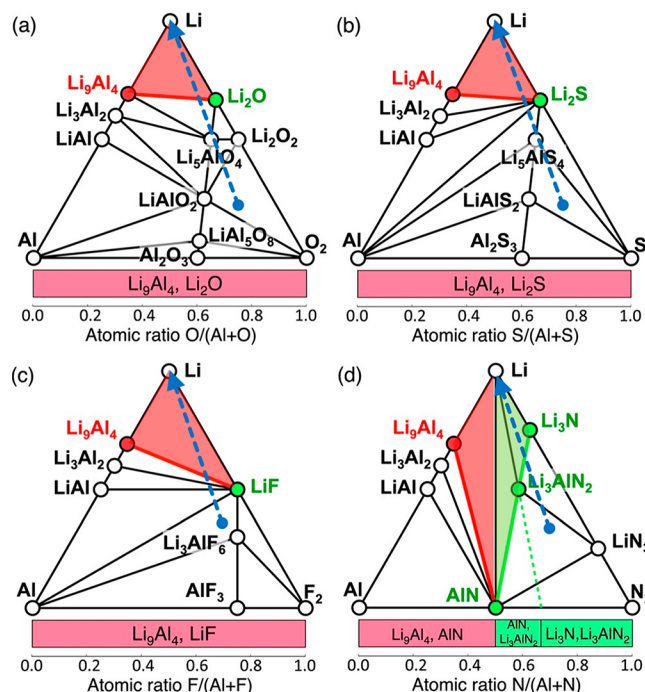


**Figure 20.** Phase diagrams of (a)  $Li-Al-O$ , (b)  $Li-Al-S$ , (c)  $Li-Al-F$ , and (d)  $Li-Al-N$  systems. Li-stable phases that are electronic insulating and that are electronic conductive are colored green and red, respectively. The bottom bar represents the phase equilibria with Li metal as a function of anion and cation atomic fraction  $x_X$  and  $x_M$ , where passivating and nonpassivating ranges are colored green and red, respectively. The blue dots and dashed arrows indicate decompositions of an example composition with Li metal. Adapted with permission from ref 302. Copyright 2017 Wiley.

in metallic phase is generated when reacting with Li. This result can be attributed to the stronger covalent bonding between nitrogen and metal cations. As a result, nitrides usually have lower cathodic limits than oxides, sulfides, or fluorides with the same metal.

**3.3.2. Chemical Reactivity with Cathodes and Coatings.** A thermodynamically stable cathode–electrolyte pair is rare in ASSBs, and chemical reactions between the cathode and SE have been characterized after battery cycling. For example, cobalt from LCO cathodes has been observed to diffuse into the LPS electrolyte and form an interdiffusion layer as thick as ~50 nm after charging the battery to 3.6 V vs Li–In (Figure 21a).<sup>306,307</sup> Although some reactions may be kinetically slow, they accelerate when high-temperature sintering is involved. In addition, at high states of charge, the driving force for such reactions increases significantly through what should be more appropriately referred to as a combined electrochemical/chemical breakdown:<sup>308</sup> At high voltage, the low Li chemical potential in the cathode can lead to Li extraction from the solid electrolyte and the oxidized reaction products in the SE then further react with the cathode material.<sup>309</sup>

Chemical reactivity is widely observed between many thiophosphate electrolytes and layered oxide cathodes such as LCO<sup>307</sup> and NCM.<sup>287</sup> The reaction is primarily driven by O/S exchange between the SE and cathodes, forming transition metal sulfide and phosphate compounds,<sup>199,225,310</sup> and these reactions are exacerbated at high states of charge.<sup>308</sup> Janek et al. reported that although no chemical reaction could be detected between  $LiNi_{0.8}Co_{0.1}Mn_{0.1}O_2$  (NCM-811) and  $\beta$ - $Li_3PS_4$  after 48 h upon

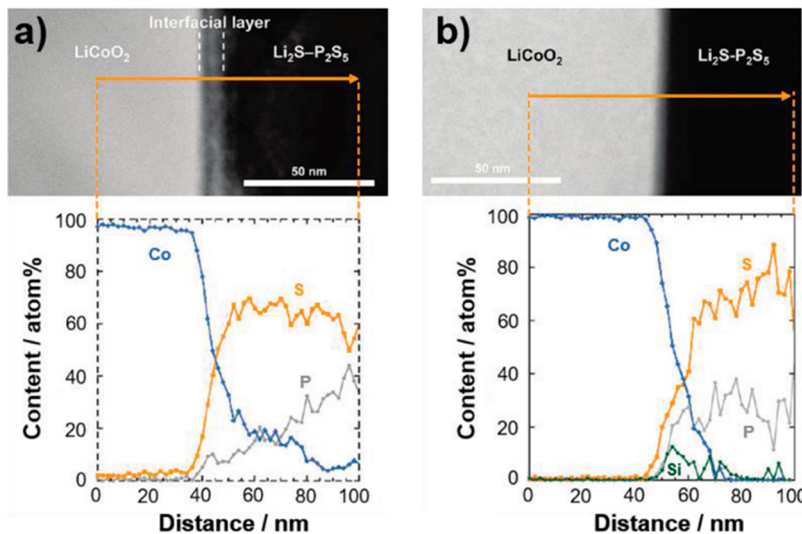


**Figure 21.** Cross-sectional scanning transmission electron microscopy (STEM) images and energy-dispersive X-ray spectroscopy line profiles of  $\text{LiCoO}_2/\text{Li}_2\text{S}-\text{P}_2\text{S}_5$  interface (a) without and (b) with a  $\text{Li}_2\text{SiO}_3$  coating, which were collected after the initial charge. Reproduced with permission from ref 307. Copyright 2010 American Chemical Society.

	Passivating interface	Mixed conducting interface
Interface schematic		
Resistance		
Examples	LIPON 	$\text{Li}_{1.6}\text{Al}_{0.5}\text{Ti}_{0.95}\text{Ge}_{0.5}(\text{PO}_4)_3$ 
Decomposition products	Passivating $\text{Li}_2\text{O}$ , $\text{Li}_3\text{P}$ , $\text{Li}_3\text{N}$	Ionic and electronic mixed conducting $\text{Li}_4\text{TiO}_4$ , $\text{Li}_2\text{O}$ , $\text{Li}_5\text{AlO}_4$ , $\text{Li}_3\text{P}$ , <b>Ge*</b> (* metallic phase)

**Figure 22.** Interface schematic and examples of different types of the interface between a SE and metal anode. Reproduced with permission from refs 333–335, 333, 2013, 334 and 2016 American Chemical Society.<sup>335</sup>

mixing,  $\text{PO}_x$  species were detected in the cell after the first charge.<sup>287</sup> Such chemical reactions will lead to interfacial resistance growth and capacity loss over time.

Compared with sulfide electrolytes, oxide SEs are generally more stable with oxide cathodes than sulfide SEs. The reaction

energies are usually much smaller than those of the reaction between a sulfide electrolyte and an oxide cathode.<sup>224,225,303</sup> However, incorporating oxide electrolytes usually requires additional processing,<sup>311</sup> such as cosintering, in situ cathode synthesis, or thin-film deposition for improved cathode/SE

contact. These processes promote the interdiffusion of elements and can form new compounds between the SE and cathode. Tremendous effort has been devoted to decreasing the sintering temperature of oxide electrolytes to mitigate these issues, which will be discussed in the later section.

The introduction of a coating layer on the cathode particles is the preferred way to prevent undesired reactions between the cathode and the SE. For example, despite the driving force for S/O exchange,<sup>303</sup> the introduction of a LiNbO<sub>3</sub> coating reduces the interface resistance between sulfide electrolytes and oxide cathodes such as LCO<sup>312</sup> and LiMn<sub>2</sub>O<sub>4</sub><sup>313</sup> by orders of magnitude at room temperature. This improvement is attributed to a relatively high electrochemical stability and the low reactivity of LiNbO<sub>3</sub> with oxide cathodes.<sup>303</sup> A LiNbO<sub>3</sub> is also predicted to have reasonable stability with sulfide electrolytes.<sup>303</sup> Similarly, the range over which cobalt diffuses out from LCO into LPS was demonstrated to be reduced when a Li<sub>2</sub>SiO<sub>3</sub> coating was applied (Figure 21a,b).<sup>307</sup> Other ternary oxide coatings such as LiTaO<sub>3</sub><sup>314</sup> and Li<sub>2</sub>ZrO<sub>3</sub><sup>315</sup> have been shown to have analogous protective effects. In addition to a low reactivity with the cathode and electrolyte, a good coating material should also exhibit electrochemical stability (against Li extraction) up to the highest cathode operating voltage. It was recently demonstrated that a Li<sub>3</sub>B<sub>11</sub>O<sub>18</sub> coating provides more effective protection than a Li<sub>2</sub>ZrO<sub>3</sub> coating, which was observed to degrade at the typical NMC charging voltage,<sup>316</sup> highlighting the importance of good intrinsic oxidation stability of the coating material.

Apart from some ternary-metal-oxide coatings, recent high-throughput computations indicated that polyanionic oxide compounds can offer the best combination of excellent electrochemical and chemical stability and good ionic conductivity. Three compounds LiH<sub>2</sub>PO<sub>4</sub>, LiTi<sub>2</sub>(PO<sub>4</sub>)<sub>3</sub>, and LiPO<sub>3</sub> were specifically highlighted as cathode coatings that show great potential for improved performance relative to that of state-of-the-art coatings.<sup>303</sup> It should be noted that despite the protection of the cathode/SE interface by cathode coatings, the contact between the SE and other electron sources (e.g., carbon and the current collector) cannot be protected unless the SE particles are also coated, which would be challenging as such a coating can significantly decrease the overall ionic conductivity of the SE mixed in the cathode composite. Hence, while cathode coatings will reduce the degradation of the SE in a composite cathode, further study is required to understand if it can really lead to cells that combine low conductor and carbon loading with very low capacity fade over hundreds of cycles.

### 3.4. Interfacial Stability with Li/Na Metal Anode

The use of Li/Na metal anodes is essential for ASSBs to achieve a high energy density. The strong electropositive character of these alkali metals makes the stability of any SE in contact with them challenging. Degradation is most likely when the SE contains a reducible cation, which in some cases leads to an electronically conducting compound in the degradation products (Figure 22).<sup>317,318</sup> When in contact with a reaction product that is electronically connected to the current collector, the SE will remain exposed to the full reducing chemical potential of the Li metal anode, and the reaction will continue. The most established mitigation strategy is to form a passivating interface when incorporating Li/Na metal in ASSBs. Some conductors can be functionally stable with Li metal through a self-passivating mechanism. Lithium phosphorus oxynitride (LIPON) as shown in Figure 22,<sup>319–321</sup> Li<sub>7</sub>P<sub>3</sub>S<sub>11</sub>,<sup>318</sup> Li<sub>6</sub>PS<sub>5</sub>X

(X = Cl, Br, I),<sup>322,323</sup> and Li<sub>3</sub>OX (X = Cl, Br)<sup>324</sup> are good examples; they form electronically insulating products such as Li<sub>3</sub>N, Li<sub>2</sub>S, Li<sub>3</sub>P, and Li<sub>2</sub>O, upon reduction or decomposition. However, there is a limited pool of such SEs that exhibit both good Li metal compatibility and high Li-ion conductivity. To prevent strong reaction with alkali metal anodes, most solid conductors require the addition of artificially constructed passivation layers.

An artificial passivation layer can be constructed through the introduction of elements that generate stable binary compounds after reaction with Li/Na metal. For example, high-dose nitrogen doping in materials has been predicted to be beneficial for Li metal stability in many Li-M-O ternary systems such as Li-Mg-O, Li-Al-O, and Li-Ti-O.<sup>302</sup> Li<sub>9</sub>S<sub>3</sub>N was also predicted to passivate Li metal through the generation of Li<sub>3</sub>N and Li<sub>2</sub>S.<sup>325</sup> Oxygen or halide doping was demonstrated to stabilize the interface between sulfide conductors and Li metal.<sup>323,326–328</sup> It was also recently demonstrated that one can introduce hydrates on the surface of the electrolyte pellet through controlled air exposure and form a passivating interface stable with metal anodes.<sup>317</sup>

Another concern at the Li metal-SE interface is the loss of interface contact. Several recent reports have shown void formation at this interface, particularly when high stripping current densities are applied.<sup>329–331</sup> While high stack pressure has been shown to be able to suppress this loss of contact,<sup>329</sup> this is not practical for large format cells. An alloying anode layer has also shown beneficial effects toward more uniform Li plating.<sup>331,332</sup>

**3.4.1. Dendrites in ASSBs.** Li metal is prone to penetrate even hard solid conductors and short the cell. While this phenomenon is often referred to as “dendrite formation”, it is not clear yet whether the mechanism is the same as in liquid electrolytes where accelerated growth occurs at a protrusion tip because of current focusing. However, to remain consistent with the prevalent terminology in the ASSB field, we will use the term “dendrites” here to refer to Li protrusions into the solid-state conductor. Currently, this is a significant problem for practical solid-state batteries with a Li metal anode because high energy density cells will require a very thin solid separator layer (see Figure 13). Hence, to create cells that do not short over hundreds of cycles, any tendency for Li penetration into the SE needs to be eliminated. The dendrite growth in SEs is complex as it mixes mechanical and chemical issues, electron and ion conductivity, microstructure, and interface roughness and contact issues. It is currently not even clear that one of these mechanisms dominates, and multiple factors may conspire to enable Li to grow through a SE.

It was previously expected that SEs would block dendritic growth because of their high elastic and shear moduli and high Li-ion transfer number. In 2005, Monroe and Newman modeled a Li metal/polymer SE interface and demonstrated that dendrite nucleation can be mechanically suppressed when the shear modulus of the SE is more than twice that of Li metal.<sup>336</sup> However, the mechanical perspective derived from this model for dendrite suppression may not be simply transplanted to other ASSBs that use inorganic SEs, and it is now accepted that a large shear modulus is not sufficient to prevent dendrite penetration in inorganic SEs. For example, the critical current density for dendrite formation at room temperature is much lower in some inorganic SEs such as LLZO (0.05–0.9 mA cm<sup>-2</sup>)<sup>337–340</sup> and LPS (0.4–1 mA cm<sup>-2</sup>)<sup>341,342</sup> than in liquid cells (4–10 mA cm<sup>-2</sup>),<sup>343,344</sup> even though both of the SEs

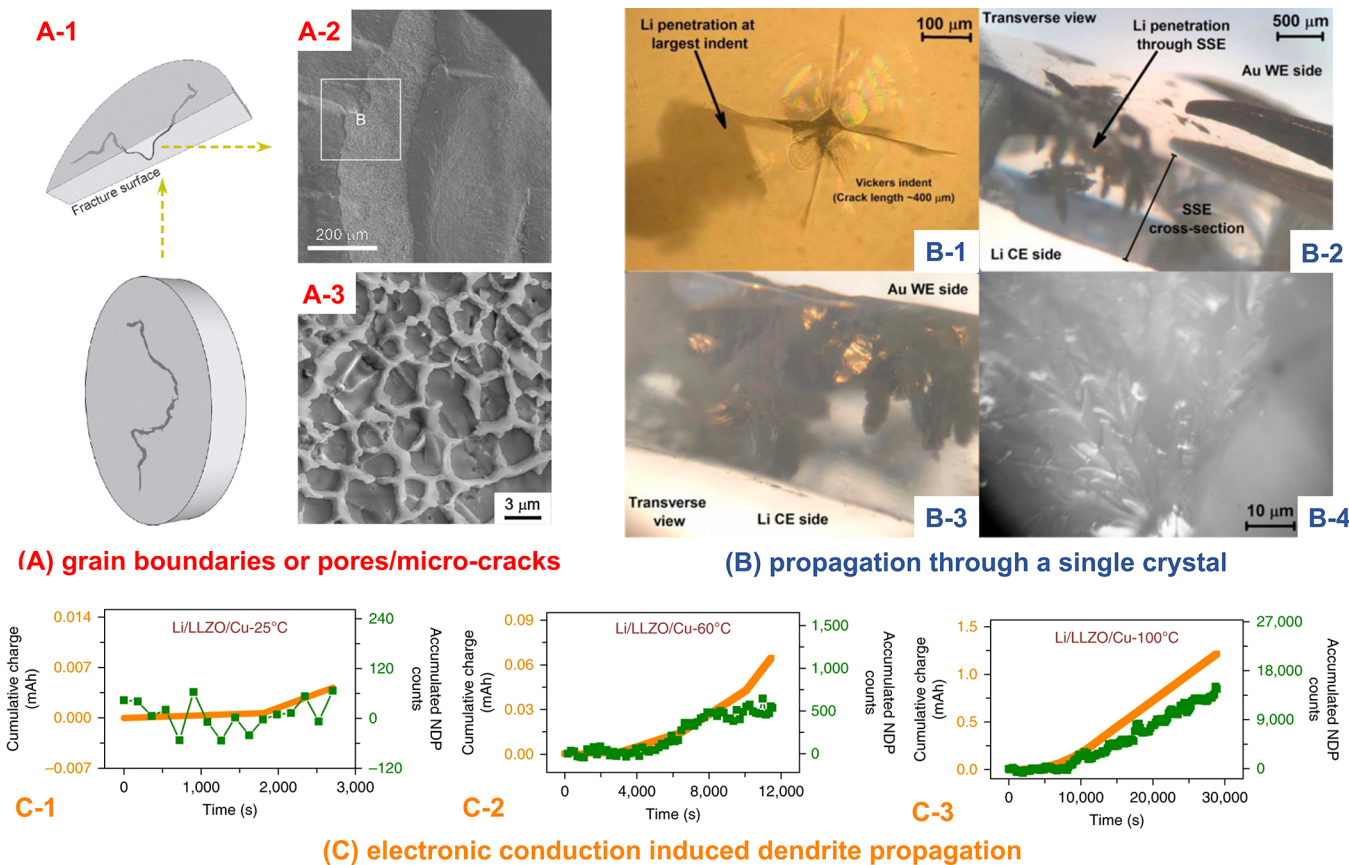


**Figure 23.** Different mechanisms proposed for dendrite propagation in a garnet SE. (a1–a3) Cross-section images of a fractured LLZO pellet after shorted by dendrite, showing the Li propagation through grain boundaries. Illustration of the location of fractured surface (a1), SEM image of the Li accumulated at grain boundary (a2), and SEM image of the overall web structure in cycled LLZO (a3). Reproduced with permission from ref 214. Copyright 2017 Elsevier. (b1–b4) optical microscopy image of subsurface lithium filament within the single crystal garnet SE. A magnified plan view showing a Vickers indent and associated corner-cracks, from one of which a lithium metal filament has grown. (b2,b3) Transverse views of the solid electrolyte showing the leaf-like morphology of the lithium metal filaments that have penetrated into, or completely through, the single crystal garnet SE. (b4) Magnified optical microscopy image of the leaf-like growth morphology of a lithium metal-filled crack, taken in transverse view. Reproduced with permission from ref 345. Copyright 2018 ECS. (c1–c3) Correlations between cumulative charges (orange line) and the accumulated NDP counts (green dots) in the total region (surface and bulk) of the LiCoO<sub>2</sub>/LLZO/Cu cell tested at 25 °C (c1), 60 °C (c2), and 100 °C (c3). Reproduced with permission from ref 350. Copyright 2019 Springer Nature.

possess much higher elastic and shear moduli than Li metal. This also suggests that critical current density may not be the best way to measure the intrinsic resistance of an SE to Li penetration. The contact area between the Li anode and an SE is generally poorly characterized, and it is likely that around areas of contact the local current density is significantly higher than the macroscopically averaged current density.

There are multiple other mechanisms that have been proposed to explain the dendrite formation and growth in ASSBs. One possible mechanism is that Li dendrites first nucleate at “hot-spots” on the rough surface of the SE separator and then propagate along the grain boundaries and/or through the connected pores or preexisting microcracks in the SE. As an example, in 2017, Sakamoto et al. observed intergranular Li dendrites that preferentially deposited along the grain boundaries of LLZO (Figure 23a1–a3).<sup>214</sup> However, Li dendrites were also observed in a LLZO single crystal,<sup>215,345</sup> leading to a widespread discussion on whether grain boundary is the main structural feature that promotes dendrite propagation. Different critical current densities have been measured in single-crystal LLZO pellets with different defect sizes and densities on the surface (Figure 23b1–b4),<sup>345</sup> suggesting that other factors such as surface morphology also play a role in dendrite

propagation, an argument that is strengthened by inhomogeneous Li plating observed at surface defects.<sup>346</sup> Increased Li-ion diffusivity at the grain boundaries has also been claimed to be a reason for the dendrite formation<sup>347–349</sup> although this is not obvious given that bulk conductivity in ionic conductors is already very high. Unlike in low conducting solids, it cannot be presumed that grain boundary conductivity is higher than bulk conductivity in SE materials.

Another recently proposed mechanism attributed the growth of Li inside LLZO and LPS pellets to their electronic conductivities after monitoring the dynamic evolution of the Li concentration profiles in different SEs.<sup>350</sup> A higher electronic conductivity in the SE pellet was shown to correspond to a higher rate of Li deposition within the SE pellet, suggesting that an internal electron network in the SE assists dendrite propagation. For example, as shown in Figure 23c1–c3, an increased Li plating within the SE pellet (the difference between total charge and Li plated at the counter electrode) was detected as the SE’s electronic conductivity is increased by raising the temperature. The electronic conductivity in the SE can lead to Li metal deposition in voids or possibly in grain boundaries. If and when these deposited Li inside the SE interconnect, the cell will be shorted. Although the electronic conductivity should always

be minimized in SEs, a threshold for the electronic conductivity that initiates dendrites is not known and must be further investigated.

### 3.5. Practical Considerations for Full-Cell Fabrication

In addition to the interfacial stability issues, many practical challenges remain for the large-scale production of ASSBs. Unlike Na/K- or multivalent (Mg, Ca,...)-ion batteries, which will likely be fabricated using a method similar to that for current LIBs, ASSBs require substantial modifications to the well-developed LIB production processes. As illustrated in Figure 17, reaching high energy density in ASSB fabrication requires an increase in the cathode loading, improvement of the interparticle contact, and reduction of the separator thickness. Existing ASSB fabrication methods still have difficulties meeting these requirements.

**3.5.1. Composite Electrode Morphology.** To achieve high energy density, the optimal electrode composite morphology should be dense with intimate cathode/electrolyte contact and with minimal SE. In traditional LIBs, the liquid electrolyte flows and fills all the pores in the composite electrode, ensuring good contact with active material particles. However, in ASSBs, long-range Li diffusion requires crossing solid particle–particle boundaries and therefore requires intimate particle–particle contact. Achieving such intimate contact is not trivial because most of the inorganic SEs do not easily deform or “flow”.

Mixing the active material and SE and pressing the electrode mixture with the separator is the most common approach to make a composite electrode at the lab scale. This method is particularly suited for sulfide SEs because their low yield strength allows them to undergo large deformation under 100 MPa level pressure and thus form a dense cathode/SE composite.<sup>206,351–356</sup> However, the pressing pressure must be selected carefully because low pressure will result in high porosity and insufficient contact, and high pressure could lead to cracking of the cathode particles.<sup>355,357</sup>

The development of solution-processed sulfide SEs has made improved cathode/SE contact possible through solution coating or infiltrating methods.<sup>267,358–360</sup> Solution coating of a thin SE layer on the cathode particle allows better cathode/SE contact and results in significant improvement of the cell performance.<sup>359,361,362</sup> Similarly, infiltrating liquefied Li<sub>6</sub>PS<sub>5</sub>Cl SE into conventional slurry-casted composite LIB cathodes results in intimate cathode/SE contact. Full cells fabricated using this infiltration method were able to fully utilize the cathode (LiCoO<sub>2</sub>) capacity with only ~30 vol % SE in the cathode composite, outperforming dry and slurry mixed composite cathodes.<sup>363</sup> However, solution processing has only been demonstrated with LiCoO<sub>2</sub>, which exhibits good electronic conductivity and does not require additional conductive additives. Applying these solution-processing methods to the state-of-art cathode materials (such as Ni-rich NMC) would require additional efforts to incorporate conductive additives such as carbon.

Achieving good cathode contact is more challenging for oxide SEs than for sulfide SEs. Oxide SEs such as LLZO do not deform easily under pressure because of their large Young's modulus (~140 GPa) and hardness (~8 GPa).<sup>364–366</sup> While high-temperature sintering can densify pellets, it can also cause unwanted reactions between the cathode and SE, resulting in high interfacial resistance and poor cell performance.<sup>367,368</sup> The addition of an ionic-conductive low-melting-temperature binder such as Li<sub>3</sub>BO<sub>3</sub> has been shown to improve the cathode/SE

contact and reduce the interfacial resistance.<sup>369</sup> Similarly, polymers such as poly(ethylene oxide) (PEO) have been used to improve the interfacial contact in oxide-SE-based composite cathodes.<sup>370,371</sup> Further research to identify a binding material with good ionic conductivity and low melting temperature could result in better particle–particle contacts in oxide-SE-based cathode composites.

Maintaining the mechanical integrity of the composite cathode and intimate contact between the active material and SE is another challenge because of the volume change of the cathode particles during cycling. Crack and void development in composite electrodes has been observed in ASSB, which almost certainly contributes to capacity decay.<sup>287,288,372</sup> Reducing the cathode particle size and developing low-strain or zero-strain cathode materials are two potential routes to decrease the cathode surface displacement during cycling and improve the mechanical stability, although small particle size of the cathode may lead to lower cathode utilization when not matched with smaller SE particle size.<sup>208</sup>

The cathode loading must be increased to reach high energy density (see Figure 13). Current cathode loadings in the literature are typically 60–70 wt % and are not high enough to realize a high energy density in ASSBs.<sup>206,315,373</sup> Several studies have separately shown that the particle sizes of the cathode active material and SE affect the morphology of the cold-pressed cathode composite and the full-cell performance.<sup>354,374–377</sup> According to recent work, the ratio of the cathode to conductor particle size rather than the absolute particle size of each component is the critical parameter.<sup>208</sup>

Methods by which the cathode components are mixed has also been found to influence performance. Slurry mixing of the components, as in traditional LIB cathode fabrication, has been shown to worse performance than dry mixing for ASSBs.<sup>378</sup> This finding was attributed to the additional binder used in slurry mixing, which may impede the ionic percolation.<sup>378</sup> Therefore, a ASSB composite cathode may require the use of no binder or alternative binders that are also ionic conductors. Higher-energy dry mixing methods such as ball milling have been shown to provide a more homogeneous cathode composite and better electrochemical performance than the hand-mixing method.<sup>378</sup>

**3.5.2. Thin Solid Electrolyte Separator.** The porous polymer separators in state-of-the-art LIBs are typically thinner than 10 μm to maximize the volumetric energy density. As shown in Figure 13, the thick SE separator layer (several hundreds of micrometers) used in current ASSBs significantly reduces their volumetric energy densities. For ASSBs to achieve much higher energy density than current LIBs, a thin separator (preferably <50 μm) is required.

Many thin-film fabrication methods have been applied to successfully produce thin SE separators at the lab scale, including radio frequency magnetron sputtering,<sup>379–381</sup> pulsed laser deposition,<sup>382–384</sup> and atomic layer deposition.<sup>385–387</sup> Although such advanced methods can produce very thin films (submicrometer in many cases), high cost, and low throughput prevent their applications in large-scale productions. Thin SE separators can also be made by tape casting, which is a scalable process and widely used in current LIB production. Less-than-100-μm-thick tape-casted SE films have been demonstrated for both oxide<sup>294</sup> and sulfide<sup>295</sup> SEs. It should be noted that a densification step is required after tape casting, and the densification method will differ for oxide (sintering) and sulfide (cold-pressing) SEs. Incorporating polymer binders or scaffolds during slurry casting, although slightly lowering the ionic

conductivity of the separator, has also been shown to greatly improve the mechanical properties and processability of the SE thin film.<sup>295,373</sup>

### 3.6. Outlook for ASSBs

The improved safety and potential leap in the volumetric energy density make ASSBs a strong contender to surpass LIBs. The extensive search for fast ion conductors has not only resulted in many superionic conductors but also led to an expanded understanding of the structural and chemical factors governing ion transport in solids.

With these advancements in ionic conductivity, the chemical and mechanical stability of various interfaces in ASSBs has become the main concern for the stable cycling of ASSBs. Although the search for a promising SE with good conductivity ( $\sigma > 10^{-4}$  S cm<sup>-1</sup>) and both good cathodic (stable with Li metal) and anodic (>4.5 V) stabilities remains ongoing, other methods have been used to alleviate these interfacial issues. Cathode coatings can stabilize the cathode–SE interface and allow the use of SEs beyond their intrinsic stability windows. However, the SE decomposition at other electron sources could still be detrimental to the long-term cyclability of ASSBs. Li metal dendrite formation is another challenge for high-energy-density ASSBs. It is clear that high mechanical strength alone cannot prevent dendrite growth, and the effect of other factors such as the electronic conductivity and separator microstructure must be further investigated.

The practical issues associated with ASSB fabrication mainly arise from the difficulty in making and retaining intimate particle–particle contact. For the composite electrode, forming an intimate interface between the SE and active material without a side reaction is challenging, particularly for mechanically hard SEs such as garnet oxides. To reduce the separator thickness, binders could be used to improve the mechanical stability of the thin SE separator. Although the processing conditions will vary depending on the mechanical properties of the SE used, significant modifications to the current LIB production process are expected for ASSB fabrication.

Finally, there are also several unexplored and less obvious potentials benefits of ASSB. Can they, for example, work with different cathode chemistries that might have been discarded for their reactivity or solubility problems in liquid electrolytes? Cathodes that use Mn as an electrochemically active element<sup>23,40</sup> may in particular be of interest for ASSBs as their redox metal is abundant and inexpensive but suffer from the solubility of Mn<sup>2+</sup> in the liquid electrolyte. With so many problems and opportunities, it can be expected that, if successful, ASSBs will go through multiple iterations of improvement.

## 4. MULTIVALENT (MG AND CA) BATTERIES

### 4.1. Introduction

Multivalent batteries have been pursued as high volumetric energy density alternative to LIBs. Although it is difficult to compete with the gravimetric energy density of lithium active materials, as lithium is one of the lightest elements in the periodic table, multivalent chemistries may have an advantage with respect to volumetric energy density. Each multivalent ion carries multiple charges ( $M^{n+}$  where  $n > 1$ ), yielding larger capacity when the same number of working ions is stored in a given electrode volume compared with monovalent ions ( $M^{1+}$ ) such as lithium. This argument for multivalent ions only translates into higher capacity when an electrode material is limited by insertion site availability but not by redox capability.

The core promise of higher energy density with multivalent batteries is tied to the possibility of utilizing multivalent metal anodes. Whereas conventional LIBs generally adopt lower-energy-density graphite anodes to avoid cell shorting caused by the dendritic growth of lithium metal, multivalent metals are less prone to dendrite formation and, thus, multivalent batteries can avoid this compromise between energy density and safety.

Several multivalent electrochemical systems (Mg<sup>2+</sup>, Ca<sup>2+</sup>, Zn<sup>2+</sup>, Al<sup>3+</sup>, etc.) have been studied; however, the discussion presented here will be limited to Mg and Ca battery chemistries with a greater focus on Mg because of the larger body of work available. While isolated Al<sup>3+</sup> intercalation has been demonstrated in one system,<sup>388</sup> many examples of Al<sup>3+</sup> intercalation likely involve cointercalation of solvent or anion molecules. Because the mobility of Al<sup>3+</sup> is even more challenging than that of the divalent ions systems we will not discuss them further.<sup>389</sup> Zn batteries have also received attention<sup>27</sup> due to their ability to operate in aqueous electrolytes, but their inherently lower voltage limits energy density.<sup>390</sup> Zn has a reduction potential of −0.76 V vs SHE, whereas those of Mg and Ca are −2.37 V vs SHE and −2.87 V vs SHE, respectively.<sup>27</sup> Thus, both Mg and Ca chemistries have promise for the realization of high-energy-density multivalent batteries but Ca electrolytes will need to be developed to support stable metal cycling at these lower reducing potentials, which has already proven difficult for Mg metal.<sup>391</sup>

To maximize the potential energy density of multivalent batteries, three Mg and Ca cell design requirements must be met. (1) Metal anodes must be used as they have higher gravimetric and volumetric energy densities than current Li-ion intercalation anodes.<sup>390,391</sup> (2) Electrolytes that are compatible with all battery components over a wide voltage range must be adopted. Finally, (3) cathodes with sufficiently high voltages (i.e., at least >3 V vs M/M<sup>2+</sup>), capacity, and multivalent-ion mobility must be used to achieve the desired energy density at reasonable cycling rates. Given these criteria, the remainder of this section will focus on examining the materials-level progress and remaining challenges for Mg and Ca anodes, nonaqueous liquid organic electrolytes, and cathodes.

To more quantitatively understand the materials design challenges, we have evaluated the impact on cell level performance using a basic cell model. The results from various anodes and cathodes are shown in Figure 25 and Figure 26, respectively. The objective of this analysis is not to determine accurate cell-level energy densities of various multivalent systems as the model assumptions fail to account for cell-design optimizations required to maximize the performance of any new multivalent battery. Rather, these comparisons serve to provide a fair metric for illustrating the effect of active material selection on cell-level energy density and assess the viability of reaching targets such as 750 Wh L<sup>-1</sup> and 350 Wh kg<sup>-1</sup>.<sup>10–13</sup> Assumptions for the electrolyte, separator, current collectors, and electrode properties were derived from similar components used in LIBs, and are outlined in more detail in the Supporting Information. The impact of various anodes was evaluated by using cell models with hypothetical Mg and Ca cathodes with densities of 4.2 g cm<sup>-3</sup>, average voltages of 3.1 V (vs Mg/Mg<sup>2+</sup> or Ca/Ca<sup>2+</sup>), and capacities of 165 mAh g<sup>-1</sup> for Mg and 175 mAh g<sup>-1</sup> for Ca. These values result in a cell-level volumetric energy density of 750 Wh L<sup>-1</sup> when paired with a Mg or Ca metal anode. Hence, one can also think of these hypothetical cathodes as design targets for multivalent battery research. When comparing cathodes, a metal Mg or Ca anode was assumed to assess the

cathode's effect on full cell energy density. These results confirm that using a metal anode and a cathode above 3 V is required for multivalent batteries to compete with LIBs on energy density.

#### 4.2. Mg and Ca Anodes

**4.2.1. Metal Anode Electrodeposition and Surface Morphology.** One advantage of multivalent batteries is derived from their potential to cycle metal anodes without dendrite formation.<sup>392–400</sup> Although all metals can grow dendrites at high enough current density or if deposition is inhomogeneous due to geometric effects or passivation, avoiding dendrite formation at reasonable current density is critical to overcome the safety hazards from shorting that affect Li-metal batteries.

The characteristic surface morphologies associated with Li and Mg deposition at current densities of 0.5, 1.0, and 2.0 mA cm<sup>-2</sup> have been compared with scanning electron microscopy (SEM) (Figure 24).<sup>392</sup> Mg deposition was performed in a Grignard

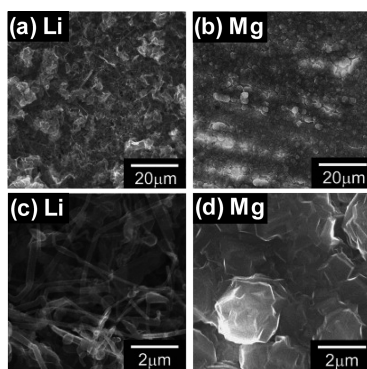


**Figure 24.** SEM images of Li (left column) and Mg (right column) morphology after deposition at 1.0 mA cm<sup>-2</sup> at magnification of 500× (top row) and 5000× (bottom row). Reproduced with permission from ref 392. Copyright 2010 Elsevier.

reagent-based electrolyte (ethyl magnesium chloride and dimethyl aluminum chloride in tetrahydrofuran), while Li deposition was performed in a conventional electrolyte solution of LiPF<sub>6</sub> in EC/DEC. In contrast to the dendritic growth of Li observed at low current density (<1.0 mA cm<sup>-2</sup>), uniform round-shaped Mg deposits were formed without any dendritic morphology.<sup>392</sup> Further evidence of the practical viability of Mg metal anodes has also been provided with cyclic voltammetry cycling of Mg against platinum working electrodes, and most impressively with coin cells where a Mg metal anode was cycled against a Mg<sub>x</sub>Mo<sub>6</sub>S<sub>8</sub> Chevrel cathode more than 2000 times.<sup>393–399</sup>

Although multivalent metal anodes are less prone to dendrite formation than Li metal, ensuring smooth metal plating remains a technical bottleneck for both Mg and Ca systems.<sup>390</sup> Mg dendritic growth<sup>404</sup> or cell failure, attributed to shorting from a Mg metal anode,<sup>405</sup> have been reported. Such issues may arise when electrolyte decomposition leads to the formation of ionically insulating layers on the Mg surface. Local penetration of these insulating layers can then lead to very high local current density and dendrite formation.

Ca electrodeposition is even more challenging than Mg because of the greater reducing potential of Ca and the similar tendency for the decomposition of conventional electrolytes to trigger the formation of ionically insulating layers on the metal anode surface.<sup>406,407</sup> As a result, only a few reports exist on the stripping/plating of Ca metal at room temperature,<sup>408–411</sup>

and no conclusive statements regarding Ca dendrite growth can so far be made. The most concrete source for the claim that Ca is less prone to dendritic growth is a comparison of Ca-SOCl<sub>2</sub> and Li-SOCl<sub>2</sub> primary battery systems.<sup>412</sup> However, the Ca system in this study exhibited a very low Coulombic efficiency (5%), and reversible Ca electrodeposition was not demonstrated.<sup>390,413</sup> For both Mg and Ca systems (especially Ca systems), more rigorous investigations are needed to fully establish the range of cycling conditions under which Mg and Ca metal anodes can operate without dendrite formation.

#### 4.2.2. Alternative Mg and Ca Anodes Compromise

**Energy Density.** Cycling of metal anodes with incompatible electrolytes or electrolyte contaminants, such as water and O<sub>2</sub>, can lead to undesired reactions.<sup>414–418</sup> To overcome these issues, alternative Mg and Ca anodes have been investigated, as they can generally be combined with conventional electrolytes, such as Mg(TFSI)<sub>2</sub> in acetonitrile or diglyme. Examples of these alternative anodes include bismuth-based (Bi) alloys,<sup>419–424</sup> tin-based (Sn, SnSb) alloys,<sup>422,425–428</sup> and titanate-based (Li<sub>4</sub>Ti<sub>5</sub>O<sub>12</sub>, NaTi<sub>3</sub>O<sub>7</sub>) anodes<sup>429–431</sup> for Mg systems, and tin-based (Sn) alloys<sup>432–434</sup> for Ca systems, several of which are discussed in greater depth in a review focused on Mg anode–electrolyte interfaces by Attias et al.<sup>435</sup> A comparison of the specific capacity and capacity density (at the fully discharged state of the electrode material) of these Mg and Ca anode alternatives is compared in Figure 25a. The experimental reduction potentials are reported except for the Ca–Sn alloy, for which the potential was derived from a density functional theory (DFT) calculation. Densities were obtained from the Inorganic Crystal Structure Database (ICSD) or from DFT-computed lattice parameters. The density of the SnSb alloy, which is thought to transform into the Mg<sub>2</sub>Sn and Mg<sub>3</sub>Sb<sub>2</sub> phases, was determined by taking the weighted average of these products. This data was then combined with the hypothetical cathodes specified earlier to determine the cell-level gravimetric and volumetric energy densities in Figure 25b. For comparison, the cell-level energy density for a Li-graphite anode paired with a NMC622 cathode is also included (see Supporting Information, *Supplemental Note S1* for further details).

It is apparent from the cell-level data in Figure 25b that every anode alternative has a significantly lower specific-gravimetric capacity and volumetric capacity than the metal anodes, confirming that multivalent batteries with these alternative anodes do not offer a significant energy density increase over LIBs. While investigation of anode alternatives may be beneficial for the electrochemical evaluation of other Mg or Ca cell components, future research efforts should be dedicated to improving the stable cycling of Mg and Ca metal anodes, which provide the best path forward for high-energy-density multivalent batteries.

#### 4.3. Mg and Ca Liquid Organic Electrolytes

**4.3.1. Monovalent vs Multivalent Electrolytes.** The selection of suitable multivalent electrolytes must consider several unique challenges not encountered in LIBs. In commercial LIBs, commonly used nonaqueous electrolytes form an ionically conducting, and electronically insulating, surface layer (known as a solid electrolyte interphase or SEI) on the graphite anode. In contrast, Mg and Ca tend to form very stable and ionically insulating surface structures when exposed to oxygen and/or water.<sup>27,414,415,436</sup> Furthermore, the higher charge density of multivalent ions leads to the formation of specific solvation structures with larger desolvation energy

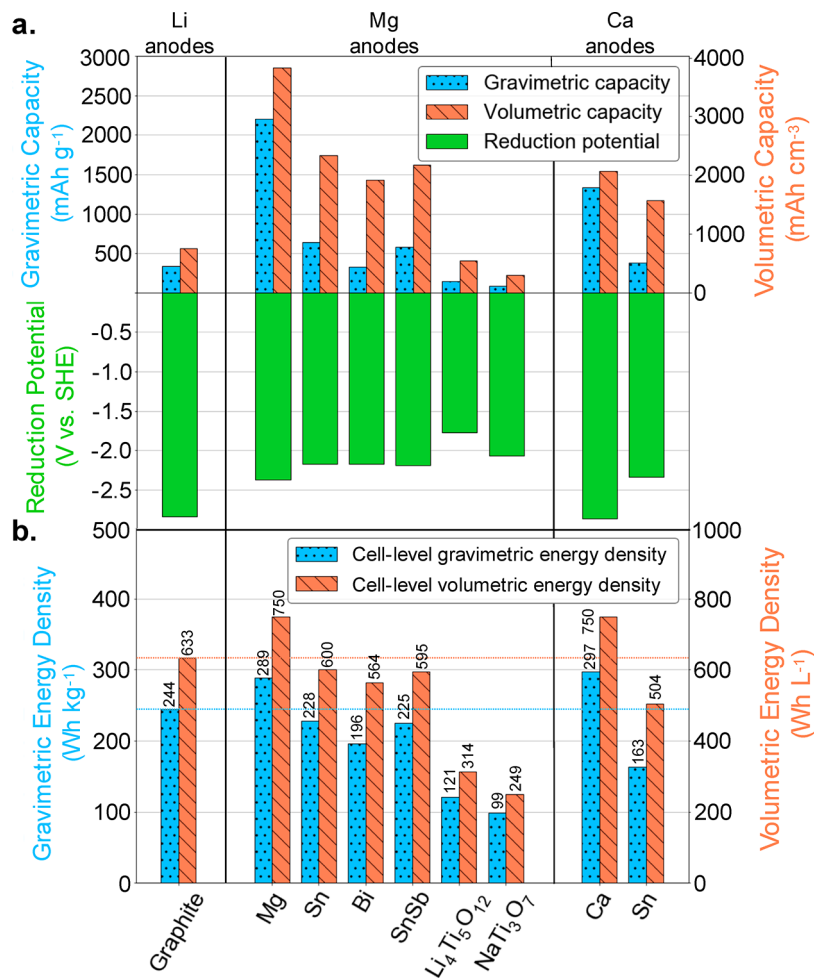


**Figure 25.** (a) Theoretical gravimetric capacities (blue dotted bars) and volumetric capacities (orange striped bars) and reduction potentials vs SHE (green solid bars) of various Mg and Ca anodes compared with those of Li-ion graphite anode. (b) Estimated cell-level gravimetric (blue dotted bars) and volumetric (orange striped bars) energy densities determined using the parameters given in the text.

barriers, thereby resulting in sluggish interfacial kinetics. Finally, the design of Mg electrolytes that are stable across a large operating voltage window has historically focused on improving their low anodic stability as it greatly limits the maximum cathode voltage. However, it has recently been proposed that the presence of partially reduced M<sup>+</sup> species resulting from the two-step charge transfer process required for divalent metal electrodeposition ( $M^{2+} \rightarrow M^{1+} \rightarrow M$ ) affects the cathodic stability of the electrolyte and must also be considered as part of the design.<sup>437</sup> These issues highlight the greater complexity of the charge-transfer, transport, and decomposition mechanisms in multivalent electrolyte systems compared with those in Li systems. The following section will cover several critical lessons learned from improving Mg electrolytes regarding the anode–electrolyte interphase, solvation structures, anodic and cathodic stability, and corrosiveness. These lessons can be more broadly applied to other multivalent electrolytes such as Ca systems, which are in an earlier stage of development.

**4.3.2. Progress in Mg Electrolytes. 4.3.2.1. Anode–Electrolyte Interphase.** Mg electrochemical deposition was first reported using Grignard-derived electrolytes in the early 20th century.<sup>438</sup> By the end of the 20th century, the best Mg electrolyte performance reported was achieved using 0.25 M Mg(AlCl<sub>2</sub>BuEt)<sub>2</sub> in tetrahydrofuran (THF), with reversible stripping and plating of Mg and a maximum stable voltage of 2.2

V vs Mg/Mg<sup>2+</sup> with nearly 100% Coulombic efficiency.<sup>396</sup> Research efforts then focused on expanding the electrochemical stability window of electrolytes and avoiding the formation of surface layers that block Mg conduction. These efforts led to incremental improvements using halogen-based electrolytes such as the “all-phenyl complex” (APC) electrolytes ( $\text{Ph}_x\text{MgCl}_{2-x}$  and  $\text{Ph}_y\text{AlCl}_{3-y}$  with different proportions in THF), which are magnesium organohaloaluminates,<sup>439</sup> and inorganic magnesium aluminum chloride complex (MACC) electrolytes (mixture of MgCl<sub>2</sub> and AlCl<sub>3</sub> in DME or THF).<sup>440</sup> Later, See et al. verified that chloride ions enhance Mg deposition by depassivating the electrode surface.<sup>441</sup> However, other reports have suggested that chloride ions can catalyze the deposition of 3d transition metals, such as Cu<sup>2+</sup> and Fe<sup>3+</sup>.<sup>442–444</sup> Specifically, Cl<sup>-</sup> was observed to stabilize the intermediate partially reduced Cu<sup>+</sup> species and therefore facilitated Cu<sup>2+</sup> deposition. A similar mechanism may also account for the success of Mg electrolyte systems with chloride ions, especially considering the Mg–Cl complexes formed in these systems.<sup>417,437</sup>

Interphase engineering has been proposed as another strategy to enhance reversible Mg electrodeposition through careful design of a layer between the electrode and electrolyte. In a recent study, Son et al. constructed this type of artificial interphase with a polymeric film composed of thermally cyclized

polyacrylonitrile and Mg trifluoromethanesulfonate that was elastic,  $Mg^{2+}$  conducting, and electronically insulating.<sup>445</sup> The authors demonstrated improved cycling stability when this polymeric film was applied to Mg metal particles cycled with a  $V_2O_5$  cathode in  $Mg(TFSI)_2/PC$ . The polymer-coated anode cell retained 70% of its capacity while the capacity of the bare anode cell quickly decayed to zero due to the formation of a  $Mg^{2+}$  passivating interphase from electrolyte decomposition at the anode. This report presents promising evidence for improving cycling performance by coating anode particles with protective and ionically conducting layers.

**4.3.2.2. Solvation Structures.** There has been a body of work to better understand multivalent-ion solvation structures, and readers are referred to a review on multivalent electrolyte solvation structures by Rajput et al. for a more in-depth summary of these computational and experimental research efforts.<sup>437</sup> In multivalent electrolyte systems, the conducting ions generally favor stronger associated solvation structures, which affects the bulk electrolyte transport properties as well as interfacial transport. For example, conducting ions can exist as “free ions,” referring to conducting ions surrounded by solvent molecules (in their first solvation shell) with no shared solvent molecules with associated ions. They can also exist as “contact ion pairs” when a counter-charged ion is present in the first solvation shell or “aggregates” if more than one counter-charged ion is present. A comparison of monovalent and multivalent TFSI salts in diglyme electrolytes characterized by X-ray scattering and molecular dynamics simulations led to the conclusion that significantly more contact ion pairs and aggregates are present in multivalent electrolytes than in their monovalent counterparts.<sup>446</sup> Contact ion pairs and especially aggregates are typically believed to hinder ion transport and decrease the overall ionic conductivity because of the larger size and desolvation barriers of these complexes.<sup>437,447</sup> Therefore, designing electrolytes based on this understanding of solvation structures is critical to improving the ion-transport properties of multivalent electrolytes.

Promising results have been reported for electrolytes based upon salts that contain anions which weakly coordinate with Mg. Weakly coordinating anions are believed to result in solvation structures with little or no ion pairing that better support Mg electrodeposition because the anion is less exposed to undesirable reactions with the Mg cation during the plating process and decreases the desolvation penalty.<sup>448</sup> For example, a  $Mg[B(fip)_4]_2$  (where fip is  $OC(H)(CF_3)_2$ ) electrolyte with weakly coordinated  $[B(fip)_4]^-$  anions exhibits high anodic stability (>4.5 V), high ionic conductivity ( $\sim 11 \text{ mS cm}^{-1}$ ), and reversible Mg electrodeposition.<sup>449</sup> Similarly, another  $Mg[TPFA]_2$  electrolyte (where TPFA is  $Al(OC(CF_3)_3)_4$ ) with the weakly coordinating anion  $[TPFA]^-$  was proven to have reversible Mg electrodeposition with a high oxidative stability of >5 V against Pt as well.<sup>448</sup> In these electrolytes, it is believed the anion’s electron-withdrawing  $CF_3$  groups are beneficial because they weakly coordinate with Mg which improves Mg stripping/plating from a kinetics standpoint, protects the anion from possible parasitic  $Mg^+$ -related decomposition reactions, and offering good oxidative stability. The favorable solvation structure is one aspect proposed to contribute to the success of these Mg electrolytes.

**4.3.2.3. Stability Against Oxidation.** Multivalent electrolytes with high anodic stability would enable the use of high-voltage cathodes, which our cell-level analysis shows to be a critical factor to achieve multivalent batteries with high energy density.

First-generation magnesium organohaloaluminate electrolytes suffered from unfavorable oxidation because of the weak Al–C bonds, which break via  $\beta$ -H elimination.<sup>417,450</sup> The anodic stability of these electrolytes is limited to 2.2 V vs  $Mg/Mg^{2+}$ <sup>451</sup> and has been gradually improved through substitution or by optimizing the anion structure.<sup>417,452–454</sup> For example, Muldoon et al. substituted some phenol ( $-Ph$ ) groups in  $Mg_2(\mu\text{-Cl})_3\cdot6THF[BPh_4]$  with fluorocarbon ( $-C_6F_5$ ) groups to form  $Mg_2(\mu\text{-Cl})_3\cdot6THF[B(C_6F_5)_3Ph]$ , which increases the maximum stable voltage from 2.6 to 3.7 V vs  $Mg/Mg^{2+}$ . The electronegativity of the fluorocarbon group effectively decreases the HOMO level of the anion, which increases its stability against oxidation and correlates with increasing the anodic window of the electrolyte.<sup>417</sup> At present, one of the best groups of electrolytes in terms of anodic stability has been reported is carba-*clos*-dodecaborate-based Mg electrolytes. For example,  $Mg[(HCB_{11}H_{11})]_2$  exhibits excellent stability between 0 and 4.6 V vs  $Mg/Mg^{2+}$  with a Coulombic efficiency of 96% when tested with a platinum working electrode. High-throughput computational screening of possible substitutions revealed that the anodic stability could be further improved by including electron-withdrawing groups, such as  $CF_3$ , F, and  $NO_2$ .<sup>453</sup> The electrochemical window was increased by 300 mV to 4.9 V vs  $Mg/Mg^{2+}$  (without sacrificing cathodic stability) using  $Mg[(FCB_{11}H_{11})]_2$ , a fluorinated variation of the carba-*clos*-dodecaborate, when tested against a Pt electrode.

**4.3.2.4. Stability Against Reduction.** To improve the electrolyte cathodic stability and enable reversible multivalent-metal-ion stripping and plating, a more complete understanding can be attained by considering all the species involved in the two-electron transfer process ( $M^{2+} \rightarrow M^+ \rightarrow M$ ). For example, electrolytes with  $Mg(TFSI)_2$  salts fail to support reversible Mg electrodeposition.<sup>455</sup> During plating, the solvated divalent ion must undergo a transient, partially charged valence state (e.g.,  $Mg^+$  or  $Ca^+$ ) as it approaches the metal surface. The process is fundamentally different from that of monovalent systems (e.g., Li and Na), where no intermediate reactive cation state exists, as a one-electron transfer is sufficient for plating. Rajput et al. coupled first-principles and atomistic simulations to show that the partial reduction at the multivalent cation center (e.g.,  $Mg^{2+} \rightarrow Mg^+$ ) competes with the charge-transfer (plating) process and activates surrounding solvent and salt molecules (e.g., the  $TFSI^-$  anion, which becomes highly susceptible to decomposition).<sup>456</sup> More recently, Seguin et al. investigated the decomposition pathway for this proposed mechanism for a number of organic solvents including glymes, sulfones, and acetonitrile (ACN) using first-principles simulations.<sup>457</sup> Although the glymes exhibited reasonably similar, high barriers for decomposition, the sulfones exhibited the lowest barrier and, notably, ACN readily accepts the electron from the partially reduced  $Mg^+$ , hindering efficient Mg plating. The authors further emphasized that although most of the solvents exhibit exergonic bond dissociation (i.e., they tend to decompose thermodynamically), in the case of the glyme series, the required energy barriers kinetically limit decomposition. In future electrolyte designs, the thermodynamics and kinetics of all solvent and salt molecules when interacting with both stable cations (e.g.,  $Mg^{2+}$  and  $Ca^{2+}$ ) and partially reduced cations (e.g.,  $Mg^+$  and  $Ca^+$ ) should be considered.

**4.3.2.5. Cell Component Compatibility.** Apart from electrolyte ion transport and electrochemical stability issues, the corrosive nature of some Mg electrolytes has presented a challenge. It has been demonstrated that electrolytes containing

halogen ions (such as  $\text{Cl}^-$ ) are corrosive, which results in the degradation of common current collector materials such as Cu, Al, and stainless steel.<sup>417,418</sup> To avoid these issues, boron-based electrolytes have been proposed as a more promising alternative to halogen-based electrolytes for Mg batteries. Examples include the previously discussed carba-closo-dodecaborate class of electrolytes ( $\text{Mg}[(\text{HCB}_{11}\text{H}_{11})]_2$  and  $\text{Mg}[(\text{FCB}_{11}\text{H}_{11})]_2$ ) and a tris(2H-hexafluoroisopropyl) borate (THFPB)-based electrolyte, which has a stability window of 0–3.8 V vs Mg/Mg<sup>2+</sup> with a Coulombic efficiency of 99.8% without current collector corrosion.<sup>453,458,459</sup> With these demonstrated successful examples, more advanced boron-based Mg electrolytes offer one future development direction for Mg electrolytes with high stability, fast electrodeposition, and less corrosion.

**4.3.3. Development of Ca Electrolytes.** There has been significantly less work on Ca liquid organic electrolytes than on Mg electrolytes. Similar to early challenges with detrimental surface layers in Mg systems, many early experiments with Ca electrolytes, such as  $\text{Ca}(\text{ClO}_4)_2$  and  $\text{Ca}(\text{BF}_4)_2$ , were unsuccessful because of the formation of reaction layers on the Ca metal anode that block Ca conduction. Reversible Ca electrodeposition was long believed to be impossible until Ponrouch et al. recently demonstrated the first partially reversible stripping/plating of Ca with  $\text{Ca}(\text{BF}_4)_2$ -containing ethylene carbonate and propylene carbonate at elevated temperature (100 °C), albeit with electrolyte decomposition byproducts such as  $\text{CaF}_2$  and  $\text{Ca}(\text{OH})_2$  accumulating upon extended cycling.<sup>406</sup> Two years later, Wang et al. reported the first reversible cycling of Ca at room temperature with  $\text{Ca}(\text{BH}_4)_2$  in THF.<sup>408</sup> This success was attributed to the spontaneous formation of  $\text{CaH}_2$  on the Ca metal, which formed a protective layer instead of an ionically insulating one. A later study on the electrodeposition of Ca on Au and Pt working electrodes with  $\text{Ca}(\text{BH}_4)_2$  in THF electrolytes provided further insight into the importance of  $\text{CaH}_2$  in the mechanism for Ca electrodeposition.<sup>460</sup> The authors proposed that the formation of  $\text{CaH}_2$  originates from dehydrogenating the  $\text{Ca}(\text{BH}_4)_2$  salt rather than any derivatives from solvent decomposition.

The number of publications reporting room temperature Ca electrodeposition continues to increase. A new fluorinated alkoxyborate Ca electrolyte  $\text{Ca}(\text{B(Ohfip)}_4)_2\text{-DME}$  (where hfip represents  $\text{CH}(\text{CF}_3)_2$ ) was reported with an anodic stability of >4.1 V vs Ca/Ca<sup>2+</sup> in DME although prolonged cycling was limited by cell failure from dendrite growth.<sup>409</sup> The low initial Coulombic efficiency and evidence of the codeposition of  $\text{CaF}_2$  reinforce the detriment of ionically insulating surface layers. The authors concluded that the formation of  $\text{CaF}_2$  was from electrolyte anion decomposition and cycling could be improved by forming a more ionically conductive SEI, such as  $\text{CaH}_2$ . Inspired by its analogous Mg variation,  $\text{Ca}[\text{B}(\text{hfip})_4]_2$  in DME was also studied and exhibited reversible deposition of Ca at room temperature with an oxidative stability >4.5 V. While a low Coulombic efficiency of 80% was observed with cyclic voltammetry (after five conditioning cycles with lower Coulombic efficiency), the authors also reported symmetric cell cycling for more than 250 h. However, evidence of  $\text{CaF}_2$  codeposition (although a smaller amount at 7%) was also found in this electrolyte system.<sup>411</sup> While the remarkably rapid progress in Ca electrochemistry since 2015 is quite compelling, designing around forming a suitable anode–electrolyte interphase will be key in further advancement of Ca electrolytes.

#### 4.4. Mg and Ca Cathodes

##### 4.4.1. Prominent Mg and Ca Intercalation Cathodes.

Improvements in electrolytes for Mg are creating urgency for the development of higher voltage cathodes. The basic cell model previously discussed indicates that a cell-level energy density of 750 Wh L<sup>-1</sup> can be reached with a 3.1 V/175 mAh g<sup>-1</sup> Mg cathode and a 3.1 V/181 mAh g<sup>-1</sup> Ca cathode. The same cell model was applied to select multivalent cathodes in Figure 26.

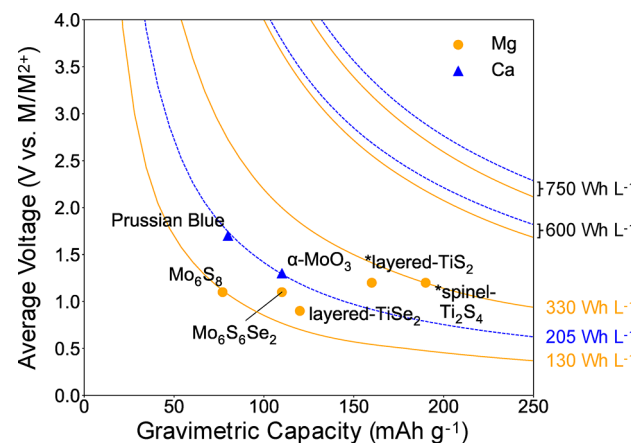


**Figure 26.** Measured average working voltage (vs Mg/Mg<sup>2+</sup> or Ca/Ca<sup>2+</sup> depending on the battery chemistry) and gravimetric capacity for demonstrated Mg cathodes (orange circles) and Ca cathodes (blue triangles). Estimated cell-level iso-energy density curves are shown for both Mg (orange solid lines) and Ca (blue dashed lines). The cathodes for which reversible cycling was only demonstrated at elevated temperatures (>30 °C) are labeled with an asterisk (\*). The calculated Prussian Blue average voltage vs Ca/Ca<sup>2+</sup> was estimated by using the thermodynamically calculated CaSn voltage of 0.8 V vs Ca/Ca<sup>2+</sup> to adjust the experimentally reported average voltage which used a Sn anode (which the authors assume forms a CaSn alloy).

Energy density was determined by assuming a density of 4.2 g/cm<sup>3</sup> for all materials, a value comparable to that of Chevrel  $\text{Mo}_6\text{S}_8$ . A remarkable fact is that the capacity density (i.e., the amount of charge stored per cc) with a  $\text{Ti}_2\text{S}_4$  spinel cathode (275 mAh/cc) is about 50% higher than the equivalent number for Li-ion systems. This data further confirms that increasing the cathode voltage is critical for multivalent batteries to achieve viable energy density.

As extensive reviews have already been written on Mg cathodes,<sup>27,461</sup> we only briefly discuss here some of the best functioning materials, and fundamental mobility issues for multivalent-ions in solids.

**4.4.1.1. Chevrel  $\text{Mg}_x\text{Mo}_6\text{S}_8$  and  $\text{Mg}_x\text{Mo}_6\text{S}_6\text{Se}_2$ .** The Chevrel phase ( $\text{Mg}_x\text{Mo}_6\text{T}_8$ , where T = S, Se, or their combination), which consists of a  $\text{Mo}_6$  octahedral cluster inside a  $\text{S}_8$  cube, was the first state-of-the-art Mg cathode class for room-temperature cycling with a theoretical capacity of 129 mAh g<sup>-1</sup> at 1.1 V.<sup>27,396</sup> The first functional Mg metal battery used a Chevrel  $\text{Mg}_x\text{Mo}_6\text{S}_8$  ( $0 < x < 2$ ) cathode<sup>396</sup> in an electrolyte of 0.25 M  $\text{Mg}(\text{AlCl}_2\text{BuEt})_2$  in THF. Only 75–80% of the Mg could be extracted which was attributed to the limited Mg mobility in a fraction of the working-ion sites resulting from the ring-trapping mechanism specific to the Chevrel structure.<sup>451</sup> Theoretical studies showed that substitution of S with Se increases the lattice size and distorts the geometry of the structure to disrupt the ring-trapping mechanism,<sup>462,463</sup> and Chevrel  $\text{Mg}_x\text{Mo}_6\text{S}_6\text{Se}_2$  was developed as the best cathode in this material class with an initial

capacity of 110 mAh g<sup>-1</sup> at 1.1 V vs Mg/Mg<sup>2+</sup> in 0.25 M Mg(AlCl<sub>3</sub>BuEt)<sub>2</sub>/THF as the electrolyte.<sup>451</sup> Attempts to increase the voltage of the Chevrel compounds have not been successful.

**4.4.1.2. Layered Mg<sub>x</sub>TiS<sub>2</sub> and Mg<sub>x</sub>TiSe<sub>2</sub>.** Reversible Mg intercalation has been demonstrated in both layered Mg<sub>x</sub>TiS<sub>2</sub><sup>464</sup> and layered Mg<sub>x</sub>TiSe<sub>2</sub> ( $0 < x < 0.5$ ), with average voltages of 1.2 V (TiS<sub>2</sub>) and 0.9 V (TiSe<sub>2</sub>) vs Mg/Mg<sup>2+</sup> and gravimetric capacities of 115 mAh g<sup>-1</sup> (TiS<sub>2</sub>) and 110 mAh g<sup>-1</sup> (TiSe<sub>2</sub>) using APC/tetraglyme as the electrolyte. It should also be noted that although 85% of the theoretical capacity for layered TiSe<sub>2</sub> (130 mAh g<sup>-1</sup>) could be obtained by cycling at room temperature, only 48% of the theoretical capacity of layered TiS<sub>2</sub> (239 mAh g<sup>-1</sup>) could be extracted even at 60 °C.

**4.4.1.3. Spinel Mg<sub>x</sub>Ti<sub>2</sub>S<sub>4</sub>.** Multiple spinels (Mg<sub>x</sub>B<sub>2</sub>X<sub>4</sub>, where  $0 < x < 1$ , B is a transition metal, and X = O or S) have been studied as Mg cathodes. The most promising electrochemical performance so far reported is for Mg<sub>x</sub>Ti<sub>2</sub>S<sub>4</sub> at 60 °C with an average voltage of 1.1 V (vs Mg/Mg<sup>2+</sup>) and capacity of 190 mAh g<sup>-1</sup>, which approaches 80% of the theoretical value (239 mAh g<sup>-1</sup>).<sup>466,467</sup> The best results were obtained with a Mg metal anode cycled at a rate of C/5 between 0.5–1.8 V in an APC/THF electrolyte. Similar to the findings for layered Mg<sub>x</sub>TiS<sub>2</sub>, testing at an elevated temperature of 60 °C improved the electrochemical performance of spinel Mg<sub>x</sub>Ti<sub>2</sub>S<sub>4</sub>.<sup>461</sup>

**4.4.1.4. Other Mg Cathodes.** In addition to the Chevrel class, layered TiS<sub>2</sub> and TiSe<sub>2</sub>, and spinels, several other Mg cathode materials have been studied; however, reversible Mg intercalation has not been unambiguously proven with materials-level experimental characterization in nonaqueous liquid organic electrolytes. These other materials include layered V<sub>2</sub>O<sub>5</sub>,<sup>27,390,461,468</sup> α-MoO<sub>3</sub>,<sup>27,469,470</sup> and olivine silicates<sup>37,471–474</sup> (e.g., FeSiO<sub>4</sub>, MnSiO<sub>4</sub>, CoSiO<sub>4</sub>). They have been excluded from further discussion to focus on cathodes with stronger experimental evidence demonstrating their relevance for full cells with Mg metal anodes and nonaqueous liquid organic electrolytes.

**4.4.1.5. Layered α-Ca<sub>x</sub>MoO<sub>3</sub>.** Room-temperature reversible Ca intercalation has been demonstrated in α-Ca<sub>x</sub>MoO<sub>3</sub> ( $0 < x < 1$ ), which consists of nonplanar double layers of MoO<sub>6</sub> octahedra. Intercalation of Ca into the molybdate structure was experimentally verified for the first cycle using ex situ XRD, Raman, EDX, and XPS measurements.<sup>475,476</sup> Cabello et al. measured a gravimetric capacity of 80–100 mAh g<sup>-1</sup> and an average voltage of 1.3 V vs Ca/Ca<sup>2+</sup> using a Swagelok-type three electrode testing setup with voltage limits of 0.5–2.2 V vs Ca/Ca<sup>2+</sup> in 0.5 M Ca(TFSI)<sub>2</sub> in 1,2-dimethoxyethane (DME) electrolyte with Ca metal embedded in steel meshes as the negative electrode and pseudoreference electrode.<sup>475</sup> Tojo et al. also performed electrochemical testing of this material with cyclic voltammetry but with 0.5 M Ca(TFSI)<sub>2</sub> in acetonitrile and achieved a higher capacity of 120 mAh g<sup>-1</sup>, although it is unlikely that the TFSI/ACN electrolyte is stable against Ca metal. The authors attributed part of their measured capacity to irreversible structural damage and electrolyte decomposition; however, little further evidence was presented to rigorously support either of these claims.<sup>476</sup>

**4.4.1.6. Prussian Blue Ca<sub>x</sub>MnFe(CN)<sub>6</sub>.** In 2015, Lipson et al. reported that Ca can intercalate in the manganese hexacyanoferrate (MnFe(CN)<sub>6</sub> or MFCN) Prussian Blue structure ( $0 < x < 0.5$ ), where the transition metal is connected by C–N bonds, forming a cubic cage-like structure.<sup>477</sup> Cycling tests were performed using desodiated MnFe(CN)<sub>6</sub> as the cathode,

calcined tin as the anode, and 0.2 M Ca(PF<sub>6</sub>)<sub>2</sub> in a nonaqueous 3:7 EC:PC electrolyte with cell voltage limits of 0–4 V. Intercalation of Ca into the Prussian Blue structure was experimentally verified for the first cycle using ex situ XRD, EDX, and XANES measurements showing a lattice expansion and contraction of the crystalline structure with intercalation.<sup>477</sup> The initial capacity measured was 80 mAh g<sup>-1</sup> (80% of the theoretical capacity of 100 mAh g<sup>-1</sup>), and an insertion voltage of ~3.4 V against Ca metal was determined using cyclic voltammetry. The capacity significantly decreased in the first 15 of 35 shown cycles.

**4.4.2. Cathode Multivalent-Ion Mobility.** The poor transport of multivalent ions in solids has been identified as one of the main hurdles for multivalent cathode materials. The high charge density of divalent ions leads to stronger electrostatic interactions with the intercalation host and raise the barrier for motion. This effect can be more prevalent at higher concentration of the multivalent ion due to the added repulsion between them. The stronger interaction between multivalent ions is also more likely to lead to ion vacancy ordering when the concentration of the working ion becomes high enough. Such ordering will create an additional energy barrier for motion.<sup>478,479</sup> While many factors can contribute to poor transport, the focus has been on understanding how to lower the intrinsically high barriers for divalent ion hopping in materials. It has been estimated that the migration barriers for reasonable diffusion of the working ion at room temperature must be below 525 meV for micrometer-sized particles or below 650 meV for nanosized particles.<sup>27,461,480,481</sup> For comparison, the theoretically calculated migration barriers for the materials discussed in the previous section are 270 meV for Mg in Chevrel Mo<sub>6</sub>S<sub>8</sub>,<sup>482</sup> >1060 meV for Mg in layered TiS<sub>2</sub>,<sup>483,484</sup> 650 meV for Mg in layered TiSe<sub>2</sub>,<sup>485</sup> and 550–615 meV for Mg in spinel Ti<sub>2</sub>S<sub>4</sub>.<sup>466,486</sup> The high migration values for Mg in layered TiS<sub>2</sub> and spinel Ti<sub>2</sub>S<sub>4</sub> underscore the fact that these materials are limited by their ion mobility and thus require elevated temperatures to yield high capacities and reversible Mg intercalation.

Two strategies have been proposed in the literature to address the issue of solid-state mobility in multivalent cathodes: (1) anion substitution with larger, more polarizable atoms, and (2) improving the understanding of the effect of the coordination environment in the host lattice.

**4.4.2.1. Anion Substitution.** Multivalent-ion mobility can be enhanced by the use of large, highly polarizable anions in the host structure. This strategy improves the mobility in two ways: (1) more polarizable anions increase the screening of the multivalent ions and (2) larger anions increase the cell volume, both of which reduce the electrostatic interaction between the multivalent-ion and host lattice. Figure 27 shows the effect of anion substitution on the ab initio calculated Mg and Ca migration barriers in the Chevrel Mo<sub>6</sub>X<sub>8</sub>, layered TiX<sub>2</sub>, and spinel M<sub>2</sub>X<sub>4</sub> structures (where X = O, S, and Se).

In general, the data in Figure 27 shows that migration barriers decrease as the polarizability of the anion increases ( $O < S < Se$ ). The computed migration barriers in Mo<sub>6</sub>Se<sub>8</sub> are lower than in Mo<sub>6</sub>S<sub>8</sub> for both Mg and Ca<sup>482</sup> consistent with the better performance of Mg<sub>x</sub>Mo<sub>6</sub>Se<sub>2</sub> over that of Mg<sub>x</sub>Mo<sub>6</sub>S<sub>8</sub> in Mg cells.<sup>451</sup> The layered Ti-compounds shows a similar effect as layered TiSe<sub>2</sub> shows better electrochemical performance at room temperature than layered TiS<sub>2</sub>.<sup>461</sup> These experimental observations are supported by the calculated migration barriers of >1060 meV for Mg in layered TiS<sub>2</sub><sup>483,484</sup> and 650 meV for Mg

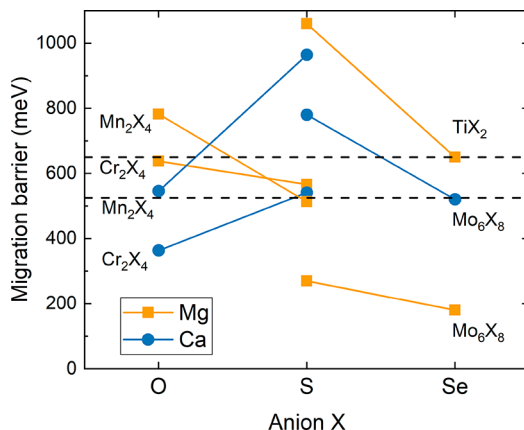


**Figure 27.** Mg and Ca migration barriers for different anions in the Chevrel and spinel structure and layered  $\text{TiX}_2$ , plotted using data from ref 480–482,484–486. The calculated barriers are based on the migration of a single cation in an empty host structure. The dashed lines at 525 and 650 meV indicate the migration barrier limits for micrometer and nanosized particles, respectively.

in layered  $\text{TiSe}_2$ .<sup>485</sup> In the spinel, improvements in changing from O to S is only seen for  $\text{Mg}^{2+}$ .<sup>480,481,486</sup> The high migration barrier in  $\text{Mg}_x\text{Mn}_2\text{O}_4$  is consistent with experimental observations of limited deintercalation (<3% Mg) at room temperature.<sup>27,487</sup> Substituting S for O in the Cr spinel lowers the computed Mg migration barrier from 637 meV in  $\text{Mg}_x\text{Cr}_2\text{O}_4$  to 566 meV in  $\text{Mg}_x\text{Cr}_2\text{S}_4$ . Even though these barriers indicate the possibility of Mg deintercalation at room temperature, very little capacity has been reported for  $\text{Mg}_x\text{Cr}_2\text{S}_4$ , even at 55 and 90 °C.<sup>488</sup> The limited capacity of the spinel  $\text{Mg}_x\text{Cr}_2\text{S}_4$  has yet to be explained but may be related to the competition between Cr and S oxidation in this compound.<sup>489</sup> Similar trends for the effect of anion substitution on migration barriers have also been reported for chalcogenide spinels, with a number of sulfide, selenide, and telluride variations considered for use as Mg conductors for solid electrolytes.<sup>281</sup>

Surprisingly, Figure 27 indicates that the Ca migration barriers increase in spinels when replacing oxygen with the more polarizable sulfide anion,<sup>480,486</sup> indicating that factors other than screening also influence mobility. This effect is related to the relative energy of the tetrahedral and octahedral site in spinels and is illustrated in Figure 28. In going from  $\text{Mn}_2\text{O}_4$  to  $\text{Mn}_2\text{S}_4$ , the octahedral site energy for  $\text{Mg}^{2+}$  is lowered with respect to the tetrahedral one. This equalizing of the site energy, together with the better screening at the activated state, lowers the migration barrier, but for  $\text{Ca}^{2+}$ , the energy lowering of the octahedral site when going from O to S is so pronounced it sits well below the tetrahedral site in  $\text{CaMn}_2\text{S}_4$ , which leads to a significant increase in the barrier.

This example illustrates that good mobility not only requires good screening by the anion but also a flat site energy landscape. The latter condition makes the effect of chemical substitutions and volume changes on the multivalent-ion mobility difficult to intuitively predict. While larger volume may reduce the overall interactions between species, as the example of the  $\text{Ca}_x\text{M}_2\text{O}_4$  shows it can also lead to greater inhomogeneity of the energy landscape, thereby increasing the barrier. Structural disorder effects such as inversion in spinels have also been argued to cause low mobility.<sup>490</sup> Although substituting more polarizable anions leads to better screening of the multivalent-ion's electrostatic interactions, and in general a lower barrier, it needs to be kept in

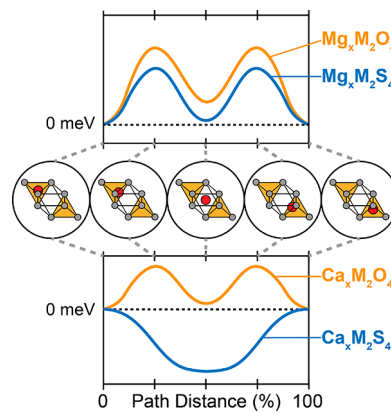


**Figure 28.** A qualitative representation of the different Mg (top) and Ca (bottom) migration barrier profiles observed in oxide (orange) and sulfide (blue) spinels. The graphics of connected tetrahedra and octahedra show the change in coordination environment of the working ion (circle colored red) as it moves along the migration path in the spinel structure.

mind that the anions with high polarizability are also more easily oxidized,<sup>303</sup> which may limit the voltage of the cathode.

**4.4.2.2. Host Lattice Coordination Environment.** The idea that a flatter energy landscape will promote higher mobility has led to a second design strategy in which coordination changes along the multivalent-ion migration path are optimized. The strategy relies on the idea that all cations have a preferred coordination environment (6 for Mg, 8 for Ca, and 4 for Zn),<sup>481</sup> which has been corroborated by an analysis of a large number of compounds in the Inorganic Crystal Structure Database.<sup>491</sup> Ion mobility can then be enhanced by finding structures where the activated state is close to the preferred coordination (lowering its energy), and the stable site does not have the preferred coordination (increasing its energy). From this perspective, the spinel is a perfect diffusion host for  $\text{Mg}^{2+}$  but is terrible for  $\text{Zn}^{2+}$ .<sup>461,481</sup> The cation arrangement in the spinel creates electrostatic conditions which make the tetrahedral site extremely favorable. The path for  $\text{Mg}^{2+}$  to migrate between tetrahedral sites goes through an octahedral site where the  $\text{Mg}^{2+}$  ions experiences its most favorable coordination, thereby lowering the migration barrier.<sup>481</sup>  $\text{Zn}^{2+}$  on the other hand prefers 4-fold coordination, and as a result its energy increases when it migrates through the octahedral site. Indeed, the computed barrier for  $\text{Zn}^{2+}$  is typically 200–300 meV higher than for  $\text{Mg}^{2+}$  in oxide spinels.<sup>480</sup> This coordination effect on the barrier has also been documented in other crystal structures and is currently one of the most powerful criteria with which to look for host structures with good multivalent-ion mobility. As shown in Figure 29, the migration barriers are higher if the multivalent ion is intercalated into a coordination environment where the multivalent ion is very favorable, as it is more difficult for the ion to migrate out of the favorable (and thus more stable) site. However, starting with the mobile ion in less favorable coordination may lead to more facile site disorder in synthesis or upon cycling, as has been argued for the spinels.<sup>481</sup>

**4.4.3. Challenges in Synthesizing Mg and Ca Cathodes with Low Migration Barriers.** A number of other promising cathode structures with low migration barriers for multivalent ion diffusion have been predicted but have been difficult to synthesize.<sup>493–495</sup> There is an inherent challenge in synthesizing compounds in which the working ion is located in an unfavored coordination environment site, and in many cases cathode

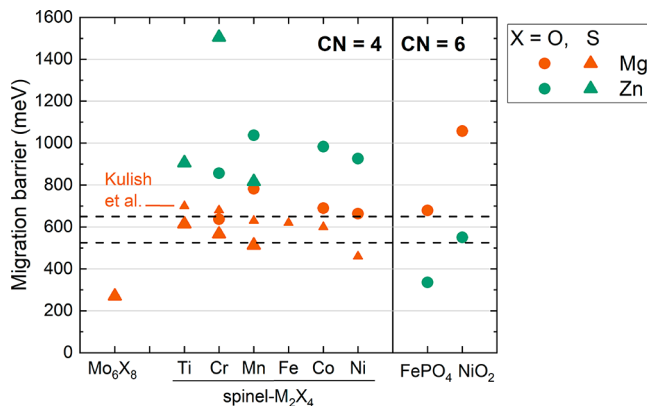


**Figure 29.** Mg and Zn migration barriers in various spinels and other structures grouped by stable insertion site coordination number.<sup>480–482,486,492</sup> The calculated barriers are based on the migration of a single cation in an empty host structure. The dashed lines at 525 and 650 meV indicate the migration barrier limits for micrometer and nanosized particles, respectively.

compounds that can cycle  $\text{Mg}^{2+}$  ions have been derived through soft-chemistry routes from other compounds. For example,  $\text{Mo}_6\text{S}_8$  is synthesized by leaching Cu from  $\text{CuMo}_3\text{S}_4$ <sup>396</sup> as is the  $\text{Ti}_2\text{S}_4$  spinel, which is obtained by oxidative removal of Cu from  $\text{CuTi}_2\text{S}_4$ .<sup>466,496</sup> It appears that none of the best Mg-cathode materials are synthesized in the discharged state (i.e., containing the Mg ion). Some materials have been predicted to have good mobility as metastable phases, but have not been successfully synthesized. For example, postspinels were previously identified as a promising class of Mg cathode materials because of their low migration barriers (e.g. 200–300 meV).<sup>493</sup> However, it has been challenging to synthesize these materials because of the high pressures required for their direct synthesis and/or ion-exchange needed to achieve the Mg-containing material.<sup>494</sup> Another material of interest is  $\text{MgMo}_3\text{P}_3\text{O}_{13}$ , which has the lowest reported calculated Mg migration of 80 meV.<sup>495</sup> In  $\text{MgMo}_3\text{P}_3\text{O}_{13}$ , edge-sharing  $\text{MoO}_6$  octahedra are interconnected by predominantly corner-sharing  $\text{MoO}_5$  trigonal bipyramids,  $\text{MoO}_4$  tetrahedra, and  $\text{PO}_4$  tetrahedra. The low migration barrier is believed to be attributable to the facile rotation of the corner-sharing  $\text{PO}_4$  groups, which can accommodate the Mg at different positions as it moves within the host lattice to maintain a constant coordination environment of 4 along the migration path.<sup>495</sup> According to ab initio calculations, this material is not a ground state,<sup>495</sup> and despite the promising low migration barrier, this structure has not been synthesized.

#### 4.5. Summary and Outlook for Multivalent Batteries

Although neither Mg nor Ca batteries are poised to overtake LIBs with the materials that have been reported to date, significant advancements in multivalent batteries have been made since results for the first reported prototype Mg battery were published in 2000.<sup>396</sup> For example, the maximum stable voltage of Mg electrolytes, which can support reversible cycling with Mg metal anodes, has increased from 2.2 V vs  $\text{Mg}/\text{Mg}^{2+}$  using Grignard-derived electrolytes such as  $\text{Mg}(\text{AlCl}_2\text{BuEt})_2$  in THF to >3.5 V vs  $\text{Mg}/\text{Mg}^{2+}$  using a number of boron-based Mg electrolyte options.<sup>417</sup> A better understanding of the reaction mechanisms and solvation structures at the molecular level, including complexes with partially reduced  $\text{M}^+$  species, has driven the advancements responsible for increasing the

operating voltage window for Mg electrolytes. While consistent progress in understanding novel challenges in Mg electrolytes has led the field to the development of several nonhalogen Mg electrolytes, these improvements have not yet been validated in a fully functioning Mg battery cell, partially due to the lack of reliable high-voltage cathodes. Identifying cathodes that will ultimately dictate the battery voltage and capacity for high-energy-density multivalent batteries is thus left as the greatest remaining challenge. Although no Mg or Ca battery chemistry has yet emerged as a clear viable alternative prototype that can outperform LIBs, there continues to be progress in improving and identifying new materials that will provide a more promising path forward to reach battery cell-level performance targets such as 750 Wh L<sup>-1</sup> and 350 Wh kg<sup>-1</sup>.

From a research perspective, one of the most important areas of progress that has evolved with the advancement of Mg batteries is an improved understanding of electrochemical processes at the molecular and atomic scale. Applying strategies derived from LIBs only resulted in limited successes in multivalent batteries because they often failed to account for the challenges specific to the electrochemistry resulting from the stronger interactions inherent to more charge-dense, multivalent ions. For example, the multistep charge-transfer process involved in divalent metal electrodeposition requires electrolytes that can withstand decomposition against partially reduced and highly reactive  $\text{M}^+$  species. Understanding the different types of solvation structures and complexes present in multivalent electrolytes is the key for improving ion transport in multivalent electrolytes. It has also been difficult to identify materials that can facilitate multivalent-ion solid-state diffusion, and overcoming this limitation is critical to identifying better Mg and Ca cathodes. Many of the mechanisms that control performance in multivalent batteries are simply more complex than those in monovalent chemistries. Therefore, a molecular-and atomic-scale understanding of these mechanisms informed by complementary advanced experimental characterization techniques with computational calculations and simulations is needed to rationally inform improvements to multivalent batteries at the materials level. Although Ca electrochemistry is much less explored and still in significantly earlier stages of development than Mg electrochemistry, the accelerated development of Ca batteries is anticipated with this improved understanding of electrochemical processes at the atomic and molecular scale.

Mg and Ca cathode candidates that reach the required energy density and electrochemical performance targets have yet to be identified given the greater challenge in finding materials with sufficient Mg or Ca mobility. The following two design strategies to reduce migration barriers will be useful in this ongoing search for Mg and Ca cathodes for high-energy-density multivalent batteries.

- (1) Multivalent ions lead to stronger electrostatic interactions between the working ion and host lattice than Li ions. Using larger, more polarizable anions such as sulfur instead of oxygen, which can better screen the charge-dense multivalent ion, can improve the structural stability and increase the cell volume.
- (2) Working ions that intercalate into stable sites with favorable coordination environments are likely to have higher migration barriers. Structures with insertion sites that have unfavored coordination environments for Mg (not 6-fold) or Ca (not 8-fold) are preferred.

## 5. SUMMARY AND OUTLOOK

LIBs have improved greatly in terms of their energy density, cycle life, power, cost, and safety since their invention in the early 1970s and commercialization in 1992 by Sony,<sup>497</sup> which has enabled their tremendous success in various applications including personal electronics and electric vehicles (EVs). However, current commercial LIBs are unlikely to meet all the performance, cost, and scaling targets required for energy storage. For EVs to reach driving distances beyond 500 km, an energy density of 500 Wh L<sup>-1</sup> is needed at the battery-module level (or 750 Wh L<sup>-1</sup> at the cell level).<sup>498–500</sup> In addition, commercial LIBs are currently 5–10 times more expensive than the cost target for stationary applications (10–20 USD kWh<sup>-1</sup> or lower for cost-competitive energy storage for power grids<sup>501</sup>). With growing concerns about the availability of natural sources of lithium, cobalt, and nickel,<sup>20,21</sup> it may be difficult for Li-ion to scale to multiple TWh/production per year. These limitations are strong motivators in the search for alternative chemistries for the next-generation mid-/large-scale batteries. It is unlikely that any given new technology will fully replace Li-ion, and alternatives should be thought of as opportunities for energy storage to grow into applications and to a scale that is difficult for Li-ion. The requirements of stationary batteries are quite different from those of power batteries used in EVs. Long cycle life (>8000 full cycles), low cost, and high energy efficiency (>90% at system level) are the most important parameters to consider. NIBs and KIBs, which rely on naturally abundant sodium and potassium resources, are likely to provide a significant advantage in terms of cost for stationary applications such as power grids. For examples, many vanadium-containing polyanionic cathodes (e.g., NVPF and KVPF) provide acceptable energy density as well as good cycling stability and rate performance. While vanadium cost today is high and comparable to cobalt/nickel, the presence of unrecovered V in oil residue makes it potentially a prevalent resource. However, Mn- and Fe-based Na-ion and K-ion cathodes are more likely to reach low cost for power-grid applications because of the use of earth-abundant materials. As shown in Figure 1, Mn-based NASICON materials (e.g., Na<sub>2</sub>MnTi(PO<sub>4</sub>)<sub>3</sub><sup>126</sup> and Na<sub>2</sub>MnZr-(PO<sub>4</sub>)<sub>3</sub><sup>502</sup>) and Fe- and/or Mn-based PBAs (e.g., Na<sub>1.92</sub>FeFe-(CN)<sub>6</sub><sup>138</sup> and K<sub>1.75</sub>Mn[Fe(CN)<sub>6</sub>]<sub>0.93</sub><sup>89</sup>) combine excellent potential for reasonable energy content and low cost. The energy densities of NASICONs and their analogues can be further increased by careful selection of the redox species and fine-tuning of the structures to enable maximum Na intercalation. To improve the stability of PBAs, a better understanding of the evolution of defects and molecular H<sub>2</sub>O in the structure with cycling is needed.

Another driving force for the investigation of “beyond Li-ion” technologies is the need for higher energy density to meet the demands of large-scale electric transportation applications, including EVs and electric aircrafts. Li-metal-based ASSBs provide a promising path to achieve high volumetric energy density using established Li-ion cathodes and have attracted significant attention as automotive battery candidates for use after 2020.<sup>500</sup> Various Li-ion superionic solid electrolytes with conductivity close to or higher than that of their liquid counterparts have been developed, thereby supporting fast ionic conduction needed for high-power applications. The use of SEs also improves safety by avoiding electrolyte leaks or fires and circumvents the need for a cooling mechanism in EVs.<sup>500</sup> However, in practice, the relatively low loading of active

materials and potential interfacial reactions in cathode composites pose a significant challenge to reach high energy density. An effective cathode coating is important for the protection of the interparticle interfaces, especially in thiophosphate-based ASSBs. While stable cycling of Li metal was demonstrated using a LIPON thin-film electrolyte in the late 1990s, the formation of Li dendrites is today still observed in more practical bulk-type solid electrolytes, including LPS and garnet. A clear understanding of the Li metal anode behavior in ASSBs is necessary before safe and stable cycling Li at high current rate can be realized. Even though all the pieces needed to realize high-energy-density ASSBs (Li metal anode, thin separator, and high cathode loading) have been demonstrated at the lab scale, their commercialization will require further engineering efforts to achieve and maintain intimate contact between all of their components.

Mg-metal batteries remain a wild card and can potentially provide a unique combination of high energy density and low cost as a “beyond Li-ion” battery technology. The use of Mg metal as an anode, which is less prone to dendritic growth than Li, leads to higher energy densities with less safety concerns. In addition, the manufacturing knowledge already established by the LIB industry can be applied to reduce the costs of Mg-metal batteries and accelerate their commercialization. However, multivalent batteries using Mg cathodes that have been studied to date fall short of their promise as high-energy-density devices. Given the progress achieved in developing Mg electrolytes with expanded electrochemical stability windows, the most pressing issue for Mg batteries is the search for high-energy-density Mg cathodes. In addition to voltage and capacity, evaluation of the solid-state mobility must be prioritized in the search for improved multivalent cathodes. Researchers should also prioritize developing Mg cathodes prepared from inexpensive elements to maintain cost-competitiveness with LIBs. Identifying a suitable Mg cathode and fully validating all of the cell components with a functional high-energy-density prototype battery are the next most important challenges that must be overcome to establish a Mg system as a viable beyond Li-ion technology. Recent studies focused on Ca electrochemistry and evaluating possible Ca active materials have led to growing interest in assessing the feasibility of Ca batteries. These initial results and the low reduction potential of Ca present a compelling justification to further pursue Ca batteries.

Although the challenges faced by the reviewed “beyond Li-ion” technologies (i.e., NIBs/KIBs, ASSBs, and multivalent batteries) appear to be very different, some share the same scientific principles and can be studied using similar approaches. For example, understanding the structural and chemical factors governing the ion diffusion in solids is not only critical for finding SEs for ASSBs but is also integral to the search for multivalent cathode materials. Therefore, strategies to reduce migration barriers, such as anion substitution with larger and more polarizable anions and providing an unfavorable coordination environment for Li or Mg that promotes ion diffusion, can be applied in the search for both fast Li-ion conductors and high-performance multivalent battery cathodes. Another important insight is the understanding the effect of increased working ion interactions. Although the layered oxide compounds are well suited for LIB cathodes, they cannot deliver high energy density when used in Na/K or multivalent batteries because of the increased interactions between the working ions and between the working ion and the host structure. The strong Na–Na/K–K interaction rapidly raises the chemical potential

vs the Na/K content in the layered structures, which results in much steeper voltage curves for Na/K cathodes and, hence, a limited energy density. For multivalent cathodes, the charge-dense multivalent ions give rise to a stronger interaction with the host structure, resulting in poor mobility in a number of layered oxide cathodes. Therefore, structures that can better screen working-ion interactions, such as NASICON, spinel, and PBA structures, are more appealing when selecting cathode materials for Na/K and multivalent batteries. Although polyanion cathodes possess poorer volumetric energy density than layered oxides for Li systems, this disadvantage is much reduced when used in Na/K systems (Figure 5). This finding indicates that one cannot simply apply past experience with LIBs when exploring “beyond Li-ion” chemistries.

In summary, each of the “beyond Li-ion” technologies reviewed in this article provides certain advantages over current LIBs. However, no alternative is currently superior to LIBs in all respects, and none of these emerging technologies are likely to completely replace LIBs in the near future. The large material cost reduction makes NIBs and KIBs strong candidates for large-scale stationary applications. The next steps for their commercialization include increasing the energy density of NASICON and fluorophosphate cathodes, dehydration of PBA cathodes to achieve long cycle life, and further optimization of hard carbon anodes. Li-metal ASSBs take advantage of the already established Li cathodes and provide significantly increased energy density and enhanced safety, making them ideal for portable electronics and EV applications. However, the commercialization of Li-metal ASSBs remains at the early stage. Further improvements include achieving improved interfacial stability, Li dendrite suppression, thin electrolyte processing, and full-cell packaging. Multivalent ion batteries can potentially provide a unique combination of high energy density and low cost. However, a promising high-energy-density multivalent cathode chemistry must first be established before pursuing their commercialization.

One final issue that all new technologies face is the lack of investment and industry effort to bring them to mass production. Even technologies that are in principle inexpensive require significant scale to realize their cost benefits. It is likely that this massive investment will only arrive when the real pressure points of Li-ion technology are approached. Whether this pressure will come from cost, safety, energy density, or resource availability, is as yet unclear, but may determine which of the beyond Li-ion technologies gets most industry support. Currently, only solid-state lithium batteries seem to have widespread industry interest, indicating a continued focus on energy density and safety but not on cost or resource constraints.

Currently, LIBs remain the most versatile technology for a wide range of applications including small-scale applications and early state vehicle electrification. “Beyond Li-ion” technologies have been brought to the stage as potential next-generation batteries that may be better suited for mid-/large-scale applications; however, further investigations are needed to fully launch these technologies into the commercial market.

## ASSOCIATED CONTENT

### SI Supporting Information

The Supporting Information is available free of charge at <https://pubs.acs.org/doi/10.1021/acs.chemrev.0c00767>.

Energy density calculation for LIBs, NIBs, KIBs, Li metal ASSBs and multivalent cells ([PDF](#))

## Special Issue Paper

This paper is an additional review for *Chem. Rev.* 2020, volume 120, issue 14, “[Beyond Li-Ion Battery Chemistry](#)”.

## AUTHOR INFORMATION

### Corresponding Authors

Gerbrand Ceder – Department of Materials Science and Engineering, University of California Berkeley, Berkeley, California 94720, United States; Materials Sciences Division, Lawrence Berkeley National Laboratory, Berkeley, California 94720, United States;  [orcid.org/0000-0001-9275-3605](https://orcid.org/0000-0001-9275-3605); Email: [gceder@berkeley.edu](mailto:gceder@berkeley.edu)

Kristin Persson – Department of Materials Science and Engineering, University of California Berkeley, Berkeley, California 94720, United States; Materials Sciences Division, Lawrence Berkeley National Laboratory, Berkeley, California 94720, United States; Email: [kristinpersson@berkeley.edu](mailto:kristinpersson@berkeley.edu)

### Authors

Yaosen Tian – Department of Materials Science and Engineering, University of California Berkeley, Berkeley, California 94720, United States; Materials Sciences Division, Lawrence Berkeley National Laboratory, Berkeley, California 94720, United States

Guobo Zeng – Department of Materials Science and Engineering, University of California Berkeley, Berkeley, California 94720, United States; Materials Sciences Division, Lawrence Berkeley National Laboratory, Berkeley, California 94720, United States

Ann Rutt – Materials Sciences Division, Lawrence Berkeley National Laboratory, Berkeley, California 94720, United States

Tan Shi – Materials Sciences Division, Lawrence Berkeley National Laboratory, Berkeley, California 94720, United States;  [orcid.org/0000-0003-0312-2639](https://orcid.org/0000-0003-0312-2639)

Haegyeom Kim – Materials Sciences Division, Lawrence Berkeley National Laboratory, Berkeley, California 94720, United States;  [orcid.org/0000-0002-5962-8244](https://orcid.org/0000-0002-5962-8244)

Jingyang Wang – Department of Materials Science and Engineering, University of California Berkeley, Berkeley, California 94720, United States; Materials Sciences Division, Lawrence Berkeley National Laboratory, Berkeley, California 94720, United States;  [orcid.org/0000-0002-0174-9334](https://orcid.org/0000-0002-0174-9334)

Julius Koettgen – Materials Sciences Division, Lawrence Berkeley National Laboratory, Berkeley, California 94720, United States

Yingzhi Sun – Department of Materials Science and Engineering, University of California Berkeley, Berkeley, California 94720, United States; Materials Sciences Division, Lawrence Berkeley National Laboratory, Berkeley, California 94720, United States

Bin Ouyang – Department of Materials Science and Engineering, University of California Berkeley, Berkeley, California 94720, United States; Materials Sciences Division, Lawrence Berkeley National Laboratory, Berkeley, California 94720, United States;  [orcid.org/0000-0002-8181-6815](https://orcid.org/0000-0002-8181-6815)

Tina Chen – Department of Materials Science and Engineering, University of California Berkeley, Berkeley, California 94720, United States; Materials Sciences Division, Lawrence Berkeley National Laboratory, Berkeley, California 94720, United States;  [orcid.org/0000-0003-0254-8339](https://orcid.org/0000-0003-0254-8339)

**Zhengyan Lun** – Department of Materials Science and Engineering, University of California Berkeley, Berkeley, California 94720, United States; Materials Sciences Division, Lawrence Berkeley National Laboratory, Berkeley, California 94720, United States;  [orcid.org/0000-0002-0186-6864](https://orcid.org/0000-0002-0186-6864)

**Ziqin Rong** – Materials Sciences Division, Lawrence Berkeley National Laboratory, Berkeley, California 94720, United States

Complete contact information is available at:

<https://pubs.acs.org/10.1021/acs.chemrev.0c00767>

### Author Contributions

Y.T., G.Z., A.R., T.S., and H.K. coauthorship.

### Notes

The authors declare no competing financial interest.

### Biographies

Yaosen Tian obtained a Ph.D. in materials science and engineering in 2020 under the supervision of Prof. Gerbrand Ceder at UC Berkeley, where he worked on the development of superionic Li/Na-ion solid conductors and interface characterizations in all-solid-state batteries. Currently, he is working as a senior scientist for an energy-storage technology start-up.

Guobo Zeng completed his Bachelor's study at Central South University, then obtained his Master's and Ph.D. degrees from ETH Zurich, supervised by Prof. Reinhard Nesper and Prof. Markus Niederberger, respectively. During his Ph.D., he focused on rational electrode materials synthesis and design towards better Li-/Na-ion batteries. He then worked as a postdoc, later as a scientist at Swiss Federal Laboratories for Materials Science and Technology (EMPA) under Dr. Matthias Koebel, where he focused on composite aerogels design for high-power battery applications. He later won the Swiss National Science Foundation fellowship and joined to Prof. Gerbrand Ceder group in LBNL, where he worked on design and synthesis of advanced Na-ion and multivalent ion batteries.

Ann Rutt is a third year Ph.D. student in Prof. Kristin Persson's group at UC Berkeley in Materials Science & Engineering. Her work focuses on searching for new multivalent cathodes using computational methods. Before graduate school, Ann worked with aqueous batteries in research and development.

Tan Shi obtained his Ph.D. in materials science and engineering from UC Berkeley under the supervision of Prof. Gerbrand Ceder. His research aims to improve the energy density and cycle life of the all-solid-state battery via the optimization of battery microstructure and interfacial stability.

Haegyeom Kim is a Staff Scientist of the Materials Sciences Division at Lawrence Berkeley National Laboratory. He obtained his Master's degree in Graduate School of EEWs (Energy Environment, Water, and Sustainability) from KAIST (Korea Advanced Institute of Science and Technology) and his Ph.D. in Materials Science from Seoul National University under supervision of Prof. Kisuk Kang. He worked as a postdoc in Prof. Gerbrand Ceder's group in LBNL on the development of beyond Li-ion batteries. Dr. Kim has published more than 70 scientific papers on energy storage materials and has received several awards, including ECS Battery Division Postdoctoral Associate Research Award, ECS Energy Technology Division Graduate Student Award, ECS Student Award of the Korea Section, The Best Graduate Thesis Award (Seoul National University), and he was recently among the select group of people chosen as Highly Cited Researchers. His research interest lies in the design of novel energy storage materials

based on the fundamental understanding of structure–property relationships and materials synthesis mechanism.

Jingyang Wang is currently a fifth year Ph.D. candidate at the Department of Materials Science & Engineering, University of California, Berkeley, under the supervision of Professor Gerbrand Ceder. His research focuses on the design, characterization, and synthesis mechanism of novel energy storage materials for beyond Li-ion batteries, including Na-ion cathode materials and Na solid-state conductors.

Julius Koettgen studied Chemistry at the RWTH Aachen University where he received his Master's degree (2012) and Ph.D. (2017) with highest honors under the supervision of Professor Manfred Martin. He then continued his experimental and computational work on oxygen ion conductors for solid oxide fuel cells as a postdoctoral researcher in Aachen. In 2018, Julius switched his focus and investigated Mg and Ca batteries at the Lawrence Berkeley National Laboratory with Professor Gerbrand Ceder. Since 2020, Julius works on the development and simulation of battery cells at Volkswagen AG.

Yingzhi Sun is a fourth year Ph.D. student under the supervision of Prof. Gerbrand Ceder at UC Berkeley. His work mainly focuses on exploring new superionic conductors for solid-state Li/Na-ion batteries and investigating the mechanism of fast Li/Na-ion migration.

Bin Ouyang is a postdoctoral scholar working at Materials Science & Engineering Department in University of California, Berkeley, with Prof. Gerbrand Ceder. He received his B.Eng. in Materials Science and Engineering at Central South University in Changsha, China, after which he obtained his Ph.D. degree at McGill University in Montreal, Canada. His research focus is on data driven screening of energy related materials.

Tina Chen is a sixth year Ph.D. student under the supervision of Prof. Gerbrand Ceder at UC Berkeley. Her research focuses on understanding and improving the electrochemical performance of Li- and Mg-ion batteries through computational methods that model the thermodynamics and kinetics of the systems.

Zhengyan Lun is currently a Ph.D. student at Materials Science & Engineering Department in University of California, Berkeley, supervised by Professor Gerbrand Ceder. He obtained his Bachelor's degree in University of Science and Technology of China majoring in materials physics. His research interests include the design and characterization of high-energy next-generation battery electrode materials with an emphasis on the Li-excess cation-disordered rock salt cathodes, design and synthesis of novel electrocatalysts, and advanced characterization techniques.

Ziqin Rong obtained his Ph.D. and Master's degrees from MIT, mentored by Prof. Gerbrand Ceder. In his Ph.D. thesis, he designed and implemented a high-throughput DFT machinery for diffusivity computations, with which he used to search for optimal multivalent battery cathode materials. After graduation, he worked as a postdoc in Prof. Ceder's lab on the predictive synthesis project, which aims to extract formatted synthesis knowledge from millions of online academic publications.

Kristin Persson is the Director of the Molecular Foundry, a user facility at Lawrence Berkeley National Lab (LBNL), a Professor at the University of California, Berkeley, and a Faculty Senior Scientist at LBNL where she leads a research group of over 40 members. She is the Director and cofounder of the Materials Project ([www.materialsproject.org](http://www.materialsproject.org)), one of the most visible of the Materials Genome initiative (MGI) funded programs attracting >150 000 users worldwide with more than 3000 unique users accessing the site every day. She is a leader in the MGI community, and she serves as an Associate Editor for Chemistry of

Materials, on the NSF Advisory Committee for Cyberinfrastructure, on the MRS Program Development Subcommittee, and is the appointed MGf ambassador for The Metal, Minerals, and Materials Society (TMS). She has published over 190 papers in peer-reviewed journals with an associated h-index of 67 and is a sought-after speaker (>27 talks in the last two years). She has received the 2018 DOE Secretary of Energy's Achievement Award, the 2017 TMS Faculty Early Career Award, the LBNL Director's 2013 award for Exceptional Scientific Achievement, and she is a 2018 Kavli Fellow.

Gerbrand Ceder is The Chancellor's Professor of Materials Science & Engineering at UC Berkeley. He received his Ph.D. in Materials Science from UC Berkeley in 1991. His research interests lie in novel materials design and development using computational and experimental methods as well as machine learning for energy generation and storage. He was elected to the National Academy of Engineering in 2017, for "the development of practical computational materials design and its application to the improvement of energy storage technology". He has served on several DOE committees, including the workgroup preparing the Basic Needs for Electrical Energy Storage report and has advised the government's Office of Science and Technology Policy on the role of computation in materials development, leading to the Materials Genome Initiative. He is a Lead Scientist for new battery technologies at the Joint Center for Energy Storage (JCESR) of the U.S. Department of Energy, and the Chief Scientist of the Energy Frontier Research Center at the National Renewable Energy Laboratory. He is a Fellow of the Materials Research Society and a member of the Royal Flemish Academy of Arts and Sciences. He has received several awards, including the Materials Theory Award from MRS, the MRS Medal, the Morris Cohen Award and the Hardy Award from TMS, the Battery Research Award from the ECS, and the research award from the International Battery Association. He is a cofounder of Computational Modeling Consultants, Pellion Technologies, and The Materials Project.

## ACKNOWLEDGMENTS

This work was supported by the Assistant Secretary for Energy Efficiency and Renewable Energy, Vehicle Technologies Office, of the U.S. Department of Energy under contract no. DE-AC02-05CH11231, under the Advanced Battery Materials Research (BMR) Program, Samsung Advanced Institute of Technology, and the BIC (Battery Innovative Contest) program of LG Chem Ltd., under contract no. 20181787. This work was also supported as part of the Joint Center for Energy Storage Research (JCESR), an Energy Innovation Hub funded by the U.S. Department of Energy, Office of Science, Basic Energy Sciences.

## REFERENCES

- (1) Cano, Z. P.; Banham, D.; Ye, S.; Hintennach, A.; Lu, J.; Fowler, M.; Chen, Z. Batteries and Fuel Cells for Emerging Electric Vehicle Markets. *Nat. Energy* **2018**, *3*, 279–289.
- (2) *Electric Flight: Laying the Groundwork for Zero-Emission Aviation*; Airbus; 2019; <https://www.airbus.com/innovation/future-technology/electric-flight.html> (accessed 2019-11-24).
- (3) Kuhn, H.; Seitz, A.; Lorenz, L.; Isikveren, A. T.; Sizmann, A. *Progress and Perspectives of Electric Air Transport*, 2012; Vol. 6.
- (4) Kwade, A.; Haselrieder, W.; Leithoff, R.; Modlinger, A.; Dietrich, F.; Droeder, K. Current Status and Challenges for Automotive Battery Production Technologies. *Nat. Energy* **2018**, *3*, 290–300.
- (5) *Global EV Outlook 2019*; IEA, 2019; <https://www.iea.org/publications/reports/globalevoutlook2019/> (accessed 2019-08-09).
- (6) Crabtree, G. The Coming Electric Vehicle Transformation: A Future Electric Transportation Market Will Depend on Battery Innovation. *Science* **2019**, *366*, 422–424.
- (7) Browne, N.; Pokharel, B. South Australia's Power Sector: Renewables, Batteries and the Future Role of Gas. *APPEA J.* **2018**, *58*, 505.
- (8) PG&E Proposes Four New Cost-effective Energy Storage Projects to CPUC; Pacific Gas and Electric Company, 2018; [https://www.pge.com/en/about/newsroom/newsdetails/index.page?title=20180629\\_pge\\_proposes\\_four\\_new\\_cost-effective\\_energy\\_storage\\_projects\\_to\\_cpuc](https://www.pge.com/en/about/newsroom/newsdetails/index.page?title=20180629_pge_proposes_four_new_cost-effective_energy_storage_projects_to_cpuc) (accessed 2019-11-24).
- (9) Weston, D. Hornsdale battery has "significant impact" on market *Windpower Monthly* 2018, <https://www.windpowernonthly.com/article/1520406/hornsdale-battery-significant-impact-market> (accessed 2019-11-24).
- (10) Andre, D.; Kim, S. J.; Lamp, P.; Lux, S. F.; Maglia, F.; Paschos, O.; Stiasny, B. Future Generations of Cathode Materials: An Automotive Industry Perspective. *J. Mater. Chem. A* **2015**, *3*, 6709–6732.
- (11) Gröger, O.; Gasteiger, H. A.; Suchsland, J.-P. Review—Electromobility: Batteries or Fuel Cells? *J. Electrochem. Soc.* **2015**, *162*, A2605–A2622.
- (12) 2015 Annual Merit Review, Vehicle Technologies Office; U.S. Department of Energy, 2015.
- (13) Schmuck, R.; Wagner, R.; Hörpel, G.; Placke, T.; Winter, M. Performance and Cost of Materials for Lithium-Based Rechargeable Automotive Batteries. *Nat. Energy* **2018**, *3*, 267–278.
- (14) Kasavajjula, U.; Wang, C.; Appleby, A. J. Nano- and Bulk-Silicon-Based Insertion Anodes for Lithium-Ion Secondary Cells. *J. Power Sources* **2007**, *163*, 1003–1039.
- (15) Li, H.; Wang, Z.; Chen, L.; Huang, X. Research on Advanced Materials for Li-Ion Batteries. *Adv. Mater.* **2009**, *21*, 4593–4607.
- (16) Su, X.; Wu, Q.; Li, J.; Xiao, X.; Lott, A.; Lu, W.; Sheldon, B. W.; Wu, J. Silicon-Based Nanomaterials for Lithium-Ion Batteries: A Review. *Adv. Energy Mater.* **2014**, *4*, 1300882.
- (17) Philippe, B.; Dedryvère, R.; Allouche, J.; Lindgren, F.; Gorgoi, M.; Rensmo, H.; Gonbeau, D.; Edström, K. Nanosilicon Electrodes for Lithium-Ion Batteries: Interfacial Mechanisms Studied by Hard and Soft X-Ray Photoelectron Spectroscopy. *Chem. Mater.* **2012**, *24*, 1107–1115.
- (18) Chan, C. K.; Peng, H.; Liu, G.; McIlwrath, K.; Zhang, X. F.; Huggins, R. A.; Cui, Y. High-Performance Lithium Battery Anodes Using Silicon Nanowires. *Nat. Nanotechnol.* **2008**, *3*, 31–35.
- (19) Szczech, J. R.; Jin, S. Nanostructured Silicon for High Capacity Lithium Battery Anodes. *Energy Environ. Sci.* **2011**, *4*, 56–72.
- (20) Olivetti, E. A.; Ceder, G.; Gaustad, G. G.; Fu, X. Lithium-Ion Battery Supply Chain Considerations: Analysis of Potential Bottlenecks in Critical Metals. *Joule* **2017**, *1*, 229–243.
- (21) Fu, X.; Beatty, D. N.; Gaustad, G. G.; Ceder, G.; Roth, R.; Kirchain, R. E.; Bustamante, M.; Babbitt, C.; Olivetti, E. A. Perspectives on Cobalt Supply through 2030 in the Face of Changing Demand. *Environ. Sci. Technol.* **2020**, *54*, 2985–2993.
- (22) Lun, Z.; Ouyang, B.; Cai, Z.; Clément, R. J.; Kwon, D. H.; Huang, J.; Papp, J. K.; Balasubramanian, M.; Tian, Y.; McCloskey, B. D.; Ji, H.; Kim, H.; Kitchaev, D. A.; Ceder, G. Design Principles for High-Capacity Mn-Based Cation-Disordered Rocksalt Cathodes. *Chem.* **2020**, *6*, 153–168.
- (23) Lee, J.; Kitchaev, D. A.; Kwon, D. H.; Lee, C. W.; Papp, J. K.; Liu, Y. S.; Lun, Z.; Clément, R. J.; Shi, T.; McCloskey, B. D.; Guo, J.; Balasubramanian, M.; Ceder, G. Reversible Mn<sup>2+</sup>/Mn<sup>4+</sup> Double Redox in Lithium-Excess Cathode Materials. *Nature* **2018**, *556*, 185–190.
- (24) Lun, Z.; Ouyang, B.; Kitchaev, D. A.; Clément, R. J.; Papp, J. K.; Balasubramanian, M.; Tian, Y.; Lei, T.; Shi, T.; McCloskey, B. D.; Lee, J.; Ceder, G. Improved Cycling Performance of Li-Excess Cation-Disordered Cathode Materials upon Fluorine Substitution. *Adv. Energy Mater.* **2019**, *9*, 1802959.
- (25) Lun, Z.; Ouyang, B.; Kwon, D. H.; Ha, Y.; Foley, E. E.; Huang, T. Y.; Cai, Z.; Kim, H.; Balasubramanian, M.; Sun, Y.; Huang, J.; Tian, Y.; Kim, H.; McCloskey, B. D.; Yang, W.; Clément, R. J.; Ji, H.; Ceder, G.

- Cation-Disordered Rocksalt-Type High-Entropy Cathodes for Li-Ion Batteries. *Nat. Mater.* **2020**. DOI: 10.1038/s41563-020-00816-0
- (26) Lee, J.; Urban, A.; Li, X.; Su, D.; Hautier, G.; Ceder, G. Unlocking the Potential of Cation-Disordered Oxides for Rechargeable Lithium Batteries. *Science (Washington, DC, U. S.)* **2014**, *343*, 519–522.
- (27) Canepa, P.; Sai Gautam, G.; Hannah, D. C.; Malik, R.; Liu, M.; Gallagher, K. G.; Persson, K. A.; Ceder, G. Odyssey of Multivalent Cathode Materials: Open Questions and Future Challenges. *Chem. Rev.* **2017**, *117*, 4287–4341.
- (28) Bhide, A.; Hofmann, J.; Katharina Dürr, A.; Janek, J.; Adelhelm, P. Electrochemical Stability of Non-Aqueous Electrolytes for Sodium-Ion Batteries and Their Compatibility with Na<sub>0.7</sub>CoO<sub>2</sub>. *Phys. Chem. Chem. Phys.* **2014**, *16*, 1987–1998.
- (29) Peters, J. F.; Peña Cruz, A. P.; Weil, M. Exploring the Economic Potential of Sodium-Ion Batteries. *Batteries* **2019**, *5*, 10.
- (30) Ahmed, S.; Gallagher, K. G.; Nelson, P. A.; Susarla, N.; Dees, D. W. *Batpac Model Software*; Argonne National Laboratory, 2016.
- (31) Aurbach, D.; McCloskey, B. D.; Nazar, L. F.; Bruce, P. G. Advances in Understanding Mechanisms Underpinning Lithium-Air Batteries. *Nature Energy* **2016**, *1*, 16128.
- (32) Pang, Q.; Liang, X.; Kwok, C. Y.; Nazar, L. F. Advances in Lithium-Sulfur Batteries Based on Multifunctional Cathodes and Electrolytes. *Nat. Energy* **2016**, *1*, 16132.
- (33) Lu, J.; Li, L.; Park, J. B.; Sun, Y. K.; Wu, F.; Amine, K. Aprotic and Aqueous Li-O<sub>2</sub> Batteries. *Chem. Rev.* **2014**, *114*, 5611–5640.
- (34) Peng, H. J.; Huang, J. Q.; Zhang, Q. A Review of Flexible Lithium-Sulfur and Analogous Alkali Metal-Chalcogen Rechargeable Batteries. *Chem. Soc. Rev.* **2017**, *46*, 5237–5288.
- (35) Manthiram, A.; Fu, Y.; Chung, S. H.; Zu, C.; Su, Y. S. Rechargeable Lithium-Sulfur Batteries. *Chem. Rev.* **2014**, *114*, 11751–11787.
- (36) SMM Annual Report; SMM Information & Technology Co, Ltd, 2020; <https://www.metal.com/>.
- (37) www.100ppi.com; SunSirs, 2020; <http://www.100ppi.com/mprice/>.
- (38) Power and Renewables; Wood MacKenzie, Verisk Analytics, 2020; <https://www.woodmac.com/Research/Products/Power-and-Renewables/>.
- (39) Delmas, C.; Fouassier, C.; Hagenmuller, P. Structural Classification and Properties of the Layered Oxides. *Physica B+C* **1980**, *99*, 81–85.
- (40) Clément, R. J.; Lun, Z.; Ceder, G. Cation-Disordered Rocksalt Transition Metal Oxides and Oxyfluorides for High Energy Lithium-Ion Cathodes. *Energy Environ. Sci.* **2020**, *13*, 345–373.
- (41) Wu, E. J.; Tepesch, P. D.; Ceder, G. Size and Charge Effects on the Structural Stability of LiMO<sub>2</sub> (M = Transition Metal) Compounds. *Philos. Mag. B* **1998**, *77*, 1039–1047.
- (42) Hewston, T. A.; Chamberland, B. L. A Survey of First-Row Ternary Oxides LiMO<sub>2</sub> (M = Sc-Cu). *J. Phys. Chem. Solids* **1987**, *48*, 97–108.
- (43) Didier, C.; Guignard, M.; Denage, C.; Szajwaj, O.; Ito, S.; Saadoune, I.; Darriet, J.; Delmas, C. Electrochemical Na-Deintercalation from NaVO<sub>2</sub>. *Electrochim. Solid-State Lett.* **2011**, *14*, A75–A78.
- (44) Komaba, S.; Takei, C.; Nakayama, T.; Ogata, A.; Yabuuchi, N. Electrochemical Intercalation Activity of Layered NaCrO<sub>2</sub> vs LiCrO<sub>2</sub>. *Electrochim. Commun.* **2010**, *12*, 355–358.
- (45) Ma, X.; Chen, H.; Ceder, G. Electrochemical Properties of Monoclinic NaMnO<sub>2</sub>. *J. Electrochem. Soc.* **2011**, *158*, A1307.
- (46) Shacklette, L. W.; Jow, T. R.; Townsend, L. Rechargeable Electrodes from Sodium Cobalt Bronzes. *J. Electrochem. Soc.* **1988**, *135*, 2669–2674.
- (47) Liu, L.; Li, X.; Bo, S. H.; Wang, Y.; Chen, H.; Twu, N.; Wu, D.; Ceder, G. High-Performance P2-Type Na<sub>2</sub>/3(Mn<sub>1</sub>/2Fe<sub>1</sub>/4Co<sub>1</sub>/4)O<sub>2</sub> Cathode Material with Superior Rate Capability for Na-Ion Batteries. *Adv. Energy Mater.* **2015**, *5*, 1500944.
- (48) Wu, D.; Li, X.; Xu, B.; Twu, N.; Liu, L.; Ceder, G. NaTiO<sub>2</sub>: A Layered Anode Material for Sodium-Ion Batteries. *Energy Environ. Sci.* **2015**, *8*, 195–202.
- (49) Yabuuchi, N.; Yoshida, H.; Komaba, S. Crystal Structures and Electrode Performance of Alpha-NaFeO<sub>2</sub> for Rechargeable Sodium Batteries. *Electrochemistry* **2012**, *80*, 716–719.
- (50) Han, M. H.; Gonzalo, E.; Singh, G.; Rojo, T. A Comprehensive Review of Sodium Layered Oxides: Powerful Cathodes for Na-Ion Batteries. *Energy Environ. Sci.* **2015**, *8*, 81–102.
- (51) Wang, P. F.; You, Y.; Yin, Y. X.; Guo, Y. G. Layered Oxide Cathodes for Sodium-Ion Batteries: Phase Transition, Air Stability, and Performance. *Adv. Energy Mater.* **2018**, *8*, 1701912.
- (52) Kim, H.; Ji, H.; Wang, J.; Ceder, G. Next-Generation Cathode Materials for Non-Aqueous Potassium-Ion Batteries. *Trends Chem.* **2019**, *1*, 682–692.
- (53) Katcho, N. A.; Carrasco, J.; Saurel, D.; Gonzalo, E.; Han, M.; Aguesse, F.; Rojo, T. Origins of Bistability and Na Ion Mobility Difference in P2- and O3-Na<sub>2</sub>/3Fe<sub>2</sub>/3Mn<sub>1</sub>/3O<sub>2</sub> Cathode Polymorphs. *Adv. Energy Mater.* **2017**, *7*, 1601477.
- (54) Mo, Y.; Ong, S. P.; Ceder, G. Insights into Diffusion Mechanisms in P2 Layered Oxide Materials by First-Principles Calculations. *Chem. Mater.* **2014**, *26*, 5208–5214.
- (55) Yabuuchi, N.; Komaba, S. Recent Research Progress on Iron- and Manganese-Based Positive Electrode Materials for Rechargeable Sodium Batteries. *Sci. Technol. Adv. Mater.* **2014**, *15*, 043501.
- (56) Yu, C.-Y.; Park, J.-S.; Jung, H.-G.; Chung, K.-Y.; Aurbach, D.; Sun, Y.-K.; Myung, S.-T. NaCrO<sub>2</sub> Cathode for High-Rate Sodium-Ion Batteries. *Energy Environ. Sci.* **2015**, *8*, 2019–2026.
- (57) Wang, P. F.; You, Y.; Yin, Y. X.; Guo, Y. G. An O3-Type NaNi<sub>0.5</sub>Mn<sub>0.5</sub>O<sub>2</sub> Cathode for Sodium-Ion Batteries with Improved Rate Performance and Cycling Stability. *J. Mater. Chem. A* **2016**, *4*, 17660–17664.
- (58) Yao, H. R.; Wang, P. F.; Gong, Y.; Zhang, J.; Yu, X.; Gu, L.; Ouyang, C.; Yin, Y. X.; Hu, E.; Yang, X. Q.; Stavitski, E.; Guo, Y. G.; Wan, L. J. Designing Air-Stable O3-Type Cathode Materials by Combined Structure Modulation for Na-Ion Batteries. *J. Am. Chem. Soc.* **2017**, *139*, 8440–8443.
- (59) Caballero, A.; Hernán, L.; Morales, J.; Sánchez, L.; Santos Peña, J.; Aranda, M. A. G. Synthesis and Characterization of High-Temperature Hexagonal P2-Na<sub>0.6</sub>Mn<sub>2</sub> and Its Electrochemical Behaviour as Cathode in Sodium Cells. *J. Mater. Chem.* **2002**, *12*, 1142–1147.
- (60) Wang, P. F.; Yao, H. R.; Liu, X. Y.; Zhang, J. N.; Gu, L.; Yu, X. Q.; Yin, Y. X.; Guo, Y. G. Ti-Substituted NaNi<sub>0.5</sub>Mn<sub>0.5</sub>-XTixO<sub>2</sub> Cathodes with Reversible O3-P3 Phase Transition for High-Performance Sodium-Ion Batteries. *Adv. Mater.* **2017**, *29*, 1700210.
- (61) Talaie, E.; Duffort, V.; Smith, H. L.; Fultz, B.; Nazar, L. F. Structure of the High Voltage Phase of Layered P2-Na<sub>2</sub>/3-z[Mn<sub>1</sub>/2Fe<sub>1</sub>/2]O<sub>2</sub> and the Positive Effect of Ni Substitution on Its Stability. *Energy Environ. Sci.* **2015**, *8*, 2512–2523.
- (62) Yue, J. L.; Zhou, Y. N.; Yu, X.; Bak, S. M.; Yang, X. Q.; Fu, Z. W. O3-Type Layered Transition Metal Oxide Na(NiCoFeTi)<sub>1</sub>/4O<sub>2</sub> as a High Rate and Long Cycle Life Cathode Material for Sodium Ion Batteries. *J. Mater. Chem. A* **2015**, *3*, 23261–23267.
- (63) Yabuuchi, N.; Kajiyama, M.; Iwatate, J.; Nishikawa, H.; Hitomi, S.; Okuyama, R.; Usui, R.; Yamada, Y.; Komaba, S. P2-Type Nax[Fe<sub>1</sub>/2Mn<sub>1</sub>/2]O<sub>2</sub> Made from Earth-Abundant Elements for Rechargeable Na<sup>+</sup> Batteries. *Nat. Mater.* **2012**, *11*, 512–517.
- (64) Lee, D. H.; Xu, J.; Meng, Y. S. An Advanced Cathode for Na-Ion Batteries with High Rate and Excellent Structural Stability. *Phys. Chem. Chem. Phys.* **2013**, *15*, 3304–3312.
- (65) Hasa, I.; Buchholz, D.; Passerini, S.; Scrosati, B.; Hassoun, J. High Performance Na<sub>0.5</sub>[Ni<sub>0.23</sub>Fe<sub>0.13</sub>Mn<sub>0.63</sub>]O<sub>2</sub> Cathode for Sodium-Ion Batteries. *Adv. Energy Mater.* **2014**, *4*, 1400083.
- (66) Shibata, T.; Fukuzumi, Y.; Kobayashi, W.; Moritomo, Y. Fast Discharge Process of Layered Cobalt Oxides Due to High Na<sup>+</sup> Diffusion. *Sci. Rep.* **2015**, *5*, 9006.
- (67) Yoshida, H.; Yabuuchi, N.; Komaba, S. NaFe<sub>0.5</sub>Co<sub>0.5</sub>O<sub>2</sub> as High Energy and Power Positive Electrode for Na-Ion Batteries. *Electrochim. Commun.* **2013**, *34*, 60–63.

- (68) Kim, H.; Seo, D. H.; Kim, J. C.; Bo, S. H.; Liu, L.; Shi, T.; Ceder, G. Investigation of Potassium Storage in Layered P3-Type  $K_0.5MnO_2$  Cathode. *Adv. Mater.* **2017**, *29*, 1702480.
- (69) Ramasamy, H. V.; Senthilkumar, B.; Barpanda, P.; Lee, Y. S. Superior Potassium-Ion Hybrid Capacitor Based on Novel P3-Type Layered  $K_0.45Mn_0.5Co_0.5O_2$  as High Capacity Cathode. *Chem. Eng. J.* **2019**, *368*, 235–243.
- (70) Kim, H.; Seo, D. H.; Urban, A.; Lee, J.; Kwon, D. H.; Bo, S. H.; Shi, T.; Papp, J. K.; McCloskey, B. D.; Ceder, G. Stoichiometric Layered Potassium Transition Metal Oxide for Rechargeable Potassium Batteries. *Chem. Mater.* **2018**, *30*, 6532–6539.
- (71) Toumar, A. J.; Ong, S. P.; Richards, W. D.; Dacek, S.; Ceder, G. Vacancy Ordering in  $O_3$ -Type Layered Metal Oxide Sodium-Ion Battery Cathodes. *Phys. Rev. Appl.* **2015**, *4*, 064002.
- (72) Bianchini, M.; Wang, J.; Clément, R.; Ceder, G. A First-Principles and Experimental Investigation of Nickel Solubility into the P2  $NaxCo_2$  Sodium-Ion Cathode. *Adv. Energy Mater.* **2018**, *8*, 1801446.
- (73) Thorne, J. S.; Zheng, L.; Lee, C. L. D.; Dunlap, R. A.; Obrovac, M. N. Synthesis and Electrochemistry of  $O_3$ -Type  $NaFeO_2-NaCo_0.5-Ni_0.5O_2$  Solid Solutions for Na-Ion Positive Electrodes. *ACS Appl. Mater. Interfaces* **2018**, *10*, 22013–22022.
- (74) Zhao, J.; Zhao, L.; Dimov, N.; Okada, S.; Nishida, T. Electrochemical and Thermal Properties of  $\alpha$ - $NaFeO_2$  Cathode for Na-Ion Batteries. *J. Electrochem. Soc.* **2013**, *160*, A3077–A3081.
- (75) Lee, E.; Brown, D. E.; Alp, E. E.; Ren, Y.; Lu, J.; Woo, J. J.; Johnson, C. S. New Insights into the Performance Degradation of Fe-Based Layered Oxides in Sodium-Ion Batteries: Instability of  $Fe^{3+}/Fe^{4+}$  Redox in  $\alpha$ - $NaFeO_2$ . *Chem. Mater.* **2015**, *27*, 6755–6764.
- (76) Li, Y.; Gao, Y.; Wang, X.; Shen, X.; Kong, Q.; Yu, R.; Lu, G.; Wang, Z.; Chen, L. Iron Migration and Oxygen Oxidation during Sodium Extraction from  $NaFeO_2$ . *Nano Energy* **2018**, *47*, 519–526.
- (77) Hasa, I.; Passerini, S.; Hassoun, J. Toward High Energy Density Cathode Materials for Sodium-Ion Batteries: Investigating the Beneficial Effect of Aluminum Doping on the P2-Type Structure. *J. Mater. Chem. A* **2017**, *5*, 4467–4477.
- (78) He, P.; Yu, H.; Li, D.; Zhou, H. Layered Lithium Transition Metal Oxide Cathodes towards High Energy Lithium-Ion Batteries. *J. Mater. Chem.* **2012**, *22*, 3680–3695.
- (79) Xu, B.; Qian, D.; Wang, Z.; Meng, Y. S. Recent Progress in Cathode Materials Research for Advanced Lithium Ion Batteries. *Mater. Sci. Eng., R* **2012**, *73*, 51–65.
- (80) Yuan, D.; Hu, X.; Qian, J.; Pei, F.; Wu, F.; Mao, R.; Ai, X.; Yang, H.; Cao, Y. P2-Type  $Na_0.67Mn_0.65Fe_0.2Ni_0.15O_2$  Cathode Material with High-Capacity for Sodium-Ion Battery. *Electrochim. Acta* **2014**, *116*, 300–305.
- (81) Oh, S. M.; Myung, S. T.; Hwang, J. Y.; Scrosati, B.; Amine, K.; Sun, Y. K. High Capacity  $O_3$ -Type  $Na[Li_{0.05}(Ni_{0.25}Fe_{0.25}Mn_{0.5})_{0.95}]O_2$  Cathode for Sodium Ion Batteries. *Chem. Mater.* **2014**, *26*, 6165–6171.
- (82) Kim, H.; Kim, J. C.; Bo, S. H.; Shi, T.; Kwon, D. H.; Ceder, G. K-Ion Batteries Based on a P2-Type  $K_0.6CoO_2$  Cathode. *Adv. Energy Mater.* **2017**, *7*, 1700098.
- (83) Ohzuku, T.; Ueda, A. Solid-State Redox Reactions of  $LiCoO_2$  ( $R3m$ ) for 4 V Secondary Lithium Cells. *J. Electrochem. Soc.* **1994**, *141*, 2972–2977.
- (84) Ding, J. J.; Zhou, Y. N.; Sun, Q.; Yu, X. Q.; Yang, X. Q.; Fu, Z. W. Electrochemical Properties of P2-Phase  $Na_0.74CoO_2$  Compounds as Cathode Material for Rechargeable Sodium-Ion Batteries. *Electrochim. Acta* **2013**, *87*, 388–393.
- (85) Barker, J.; Gover, R. K. B.; Burns, P.; Bryan, A.; Saidi, M. Y.; Swoyer, J. L. Structural and Electrochemical Properties of Lithium Vanadium Fluorophosphate,  $LiVPO_4F$ . *J. Power Sources* **2005**, *146*, 516–520.
- (86) Ge, X.; Li, X.; Wang, Z.; Guo, H.; Yan, G.; Wu, X.; Wang, J. Facile Synthesis of  $NaVPO_4F/C$  Cathode with Enhanced Interfacial Conductivity towards Long-Cycle and High-Rate Sodium-Ion Batteries. *Chem. Eng. J.* **2019**, *357*, 458–462.
- (87) Okubo, M.; Asakura, D.; Mizuno, Y.; Kim, J. D.; Mizokawa, T.; Kudo, T.; Honma, I. Switching Redox-Active Sites by Valence Tautomerism in Prussian Blue Analogues  $AxMny[Fe(CN)_6] \cdot nH_2O$  ( $A$ : K, Rb): Robust Frameworks for Reversible Li Storage. *J. Phys. Chem. Lett.* **2010**, *1*, 2063–2071.
- (88) Song, J.; Wang, L.; Lu, Y.; Liu, J.; Guo, B.; Xiao, P.; Lee, J. J.; Yang, X. Q.; Henkelman, G.; Goodenough, J. B. Removal of Interstitial  $H_2O$  in Hexacyanometallates for a Superior Cathode of a Sodium-Ion Battery. *J. Am. Chem. Soc.* **2015**, *137*, 2658–2664.
- (89) Bie, X.; Kubota, K.; Hosaka, T.; Chihara, K.; Komaba, S. A Novel K-Ion Battery: Hexacyanoferrate(II)/Graphite Cell. *J. Mater. Chem. A* **2017**, *5*, 4325–4330.
- (90) Kondrakov, A. O.; Schmidt, A.; Xu, J.; Geßwein, H.; Möning, R.; Hartmann, P.; Sommer, H.; Brezesinski, T.; Janek, J. Anisotropic Lattice Strain and Mechanical Degradation of High- and Low-Nickel NCM Cathode Materials for Li-Ion Batteries. *J. Phys. Chem. C* **2017**, *121*, 3286–3294.
- (91) Barpanda, P.; Lander, L.; Nishimura, S. I.; Yamada, A. Polyanionic Insertion Materials for Sodium-Ion Batteries. *Adv. Energy Mater.* **2018**, *8*, 1703055.
- (92) Fang, C.; Huang, Y.; Zhang, W.; Han, J.; Deng, Z.; Cao, Y.; Yang, H. Routes to High Energy Cathodes of Sodium-Ion Batteries. *Adv. Energy Mater.* **2016**, *6*, 1501727.
- (93) Zeng, G.; Caputo, R.; Carriazo, D.; Luo, L.; Niederberger, M. Tailoring Two Polymorphs of  $LiFePO_4$  by Efficient Microwave-Assisted Synthesis: A Combined Experimental and Theoretical Study. *Chem. Mater.* **2013**, *25*, 3399–3407.
- (94) Kundu, D.; Talaie, E.; Duffort, V.; Nazar, L. F. The Emerging Chemistry of Sodium Ion Batteries for Electrochemical Energy Storage. *Angew. Chem., Int. Ed.* **2015**, *54*, 3431–3448.
- (95) Fang, Y.; Zhang, J.; Xiao, L.; Ai, X.; Cao, Y.; Yang, H. Phosphate Framework Electrode Materials for Sodium Ion Batteries. *Adv. Sci.* **2017**, *4*, 1600392.
- (96) Barpanda, P.; Oyama, G.; Nishimura, S. I.; Chung, S. C.; Yamada, A. A 3.8-V Earth-Abundant Sodium Battery Electrode. *Nat. Commun.* **2014**, *5*, 4358.
- (97) Li, S.; Guo, J.; Ye, Z.; Zhao, X.; Wu, S.; Mi, J. X.; Wang, C. Z.; Gong, Z.; McDonald, M. J.; Zhu, Z.; Ho, K. M.; Yang, Y. Zero-Strain  $Na_2FeSiO_4$  as Novel Cathode Material for Sodium-Ion Batteries. *ACS Appl. Mater. Interfaces* **2016**, *8*, 17233–17238.
- (98) Barker, J.; Saidi, M. Y.; Swoyer, J. L. A Sodium-Ion Cell Based on the Fluorophosphate Compound  $NaVPO_4F$ . *Electrochim. Solid-State Lett.* **2003**, *6*, A1–A4.
- (99) Recham, N.; Chotard, J.-N.; Dupont, L.; Djellab, K.; Armand, M.; Tarascon, J.-M. Ionothermal Synthesis of Sodium-Based Fluorophosphate Cathode Materials. *J. Electrochem. Soc.* **2009**, *156*, A993.
- (100) Tripathi, R.; Wood, S. M.; Islam, M. S.; Nazar, L. F. Na-Ion Mobility in Layered  $Na_2FePO_4F$  and Olivine  $Na[Fe,Mn]PO_4$ . *Energy Environ. Sci.* **2013**, *6*, 2257–2264.
- (101) Chihara, K.; Kitajou, A.; Gocheva, I. D.; Okada, S.; Yamaki, J. I. Cathode Properties of  $Na_3M_2(PO_4)_2F_3$  [ $M = Ti, Fe, V$ ] for Sodium-Ion Batteries. *J. Power Sources* **2013**, *227*, 80–85.
- (102) Li, H.; Zhang, Z.; Xu, M.; Bao, W.; Lai, Y.; Zhang, K.; Li, J. Triclinic Off-Stoichiometric  $Na_3.12Mn_2.44(P_2O_7)_2/C$  Cathode Materials for High-Energy/Power Sodium-Ion Batteries. *ACS Appl. Mater. Interfaces* **2018**, *10*, 24564–24572.
- (103) Panin, R. V.; Drozhzhin, O. A.; Fedotov, S. S.; Suchkova, E. A.; Khasanova, N. R.; Antipov, E. V. Pyrophosphates  $AMoP_2O_7$  ( $A = Li$  and  $Na$ ): Synthesis, Structure and Electrochemical Properties. *Mater. Res. Bull.* **2018**, *106*, 170–175.
- (104) Wang, Q.; Madsen, A.; Owen, J. R.; Weller, M. T. Direct Hydrofluorothermal Synthesis of Sodium Transition Metal Fluorosulfates as Possible Na-Ion Battery Cathode Materials. *Chem. Commun.* **2013**, *49*, 2121–2123.
- (105) Choi, J. W.; Aurbach, D. Promise and Reality of Post-Lithium-Ion Batteries with High Energy Densities. *Nat. Rev. Mater.* **2016**, *1*, 16013.
- (106) Xiang, X.; Zhang, K.; Chen, J. Recent Advances and Prospects of Cathode Materials for Sodium-Ion Batteries. *Adv. Mater.* **2015**, *27*, 5343–5364.

- (107) Bianchini, M.; Fauth, F.; Brisset, N.; Weill, F.; Suard, E.; Masquelier, C.; Croguennec, L. Comprehensive Investigation of the Na<sub>3</sub>V<sub>2</sub>(PO<sub>4</sub>)<sub>2</sub>F<sub>3</sub>-NaV<sub>2</sub>(PO<sub>4</sub>)<sub>2</sub>F<sub>3</sub> System by Operando High Resolution Synchrotron X-Ray Diffraction. *Chem. Mater.* **2015**, *27*, 3009–3020.
- (108) Zhang, X.; Rui, X.; Chen, D.; Tan, H.; Yang, D.; Huang, S.; Yu, Y. Na<sub>3</sub>V<sub>2</sub>(PO<sub>4</sub>)<sub>3</sub>: An Advanced Cathode for Sodium-Ion Batteries. *Nanoscale* **2019**, *11*, 2556–2576.
- (109) Bianchini, M.; Xiao, P.; Wang, Y.; Ceder, G. Additional Sodium Insertion into Polyanionic Cathodes for Higher-Energy Na-Ion Batteries. *Adv. Energy Mater.* **2017**, *7*, 1700514.
- (110) Broux, T.; Bamine, T.; Fauth, F.; Simonelli, L.; Olszewski, W.; Marini, C.; Ménétrier, M.; Carlier, D.; Masquelier, C.; Croguennec, L. Strong Impact of the Oxygen Content in Na<sub>3</sub>V<sub>2</sub>(PO<sub>4</sub>)<sub>2</sub>F<sub>3</sub>-YO<sub>y</sub> ( $0 \leq y \leq 2$ ) on Its Structural and Electrochemical Properties. *Chem. Mater.* **2016**, *28*, 7683–7692.
- (111) Xu, M.; Xiao, P.; Stauffer, S.; Song, J.; Henkelman, G.; Goodenough, J. B. Theoretical and Experimental Study of Vanadium-Based Fluorophosphate Cathodes for Rechargeable Batteries. *Chem. Mater.* **2014**, *26*, 3089–3097.
- (112) Bianchini, M.; Brisset, N.; Fauth, F.; Weill, F.; Elkaim, E.; Suard, E.; Masquelier, C.; Croguennec, L. Na<sub>3</sub>V<sub>2</sub>(PO<sub>4</sub>)<sub>2</sub>F<sub>3</sub> Revisited: A High-Resolution Diffraction Study. *Chem. Mater.* **2014**, *26*, 4238–4247.
- (113) Qi, Y.; Mu, L.; Zhao, J.; Hu, Y. S.; Liu, H.; Dai, S. Superior Na-Storage Performance of Low-Temperature-Synthesized Na<sub>3</sub>(VO<sub>1-x</sub>PO<sub>4</sub>)<sub>2</sub>F<sub>1+2x</sub> ( $0 \leq x \leq 1$ ) Nanoparticles for Na-Ion Batteries. *Angew. Chem., Int. Ed.* **2015**, *54*, 9911–9916.
- (114) Kim, H.; Seo, D. H.; Bianchini, M.; Clément, R. J.; Kim, H.; Kim, J. C.; Tian, Y.; Shi, T.; Yoon, W. S.; Ceder, G. A New Strategy for High-Voltage Cathodes for K-Ion Batteries: Stoichiometric KVPO<sub>4</sub>F. *Adv. Energy Mater.* **2018**, *8*, 1801591.
- (115) Xu, J.; Ma, C.; Balasubramanian, M.; Meng, Y. S. Understanding Na<sub>2</sub>Ti<sub>3</sub>O<sub>7</sub> as an Ultra-Low Voltage Anode Material for a Na-Ion Battery. *Chem. Commun.* **2014**, *50*, 12564–12567.
- (116) Yan, G.; Mariyappan, S.; Rousse, G.; Jacquet, Q.; Deschamps, M.; David, R.; Mirvaux, B.; Freeland, J. W.; Tarascon, J. M. Higher Energy and Safer Sodium Ion Batteries via an Electrochemically Made Disordered Na<sub>3</sub>V<sub>2</sub>(PO<sub>4</sub>)<sub>2</sub>F<sub>3</sub> Material. *Nat. Commun.* **2019**, *10*, 585.
- (117) Chen, S.; Wu, C.; Shen, L.; Zhu, C.; Huang, Y.; Xi, K.; Maier, J.; Yu, Y. Challenges and Perspectives for NASICON-Type Electrode Materials for Advanced Sodium-Ion Batteries. *Adv. Mater.* **2017**, *29*, 1700431.
- (118) Kawai, K.; Zhao, W.; Nishimura, S. I.; Yamada, A. High-Voltage Cr<sup>4+</sup>/Cr<sup>3+</sup> Redox Couple in Polyanion Compounds. *ACS Appl. Energy Mater.* **2018**, *1*, 928–931.
- (119) Zakharkin, M. V.; Drozhzhin, O. A.; Tereshchenko, I. V.; Chernyshov, D.; Abakumov, A. M.; Antipov, E. V.; Stevenson, K. J. Enhancing Na<sup>+</sup> Extraction Limit through High Voltage Activation of the NASICON-Type Na<sub>4</sub>MnV(PO<sub>4</sub>)<sub>3</sub> Cathode. *ACS Appl. Energy Mater.* **2018**, *1*, 5842–5846.
- (120) Li, H.; Bai, Y.; Wu, F.; Ni, Q.; Wu, C. Na-Rich Na<sub>3+x</sub>V<sub>2-x</sub>Ni<sub>x</sub>(PO<sub>4</sub>)<sub>3</sub>/C for Sodium Ion Batteries: Controlling the Doping Site and Improving the Electrochemical Performances. *ACS Appl. Mater. Interfaces* **2016**, *8*, 27779–27787.
- (121) Liu, R.; Xu, G.; Li, Q.; Zheng, S.; Zheng, G.; Gong, Z.; Li, Y.; Kruskop, E.; Fu, R.; Chen, Z.; Amine, K.; Yang, Y. Exploring Highly Reversible 1.5-Electron Reactions (V<sup>3+</sup>/V<sup>4+</sup>/V<sup>5+</sup>) in Na<sub>3</sub>VCr(PO<sub>4</sub>)<sub>3</sub> Cathode for Sodium-Ion Batteries. *ACS Appl. Mater. Interfaces* **2017**, *9*, 43632–43639.
- (122) Zhou, W.; Xue, L.; Lü, X.; Gao, H.; Li, Y.; Xin, S.; Fu, G.; Cui, Z.; Zhu, Y.; Goodenough, J. B. NaxM<sub>x</sub>V(PO<sub>4</sub>)<sub>3</sub> (M = Mn, Fe, Ni) Structure and Properties for Sodium Extraction. *Nano Lett.* **2016**, *16*, 7836–7841.
- (123) Li, H.; Jin, T.; Chen, X.; Lai, Y.; Zhang, Z.; Bao, W.; Jiao, L. Rational Architecture Design Enables Superior Na Storage in Greener NASICON-Na<sub>4</sub>MnV(PO<sub>4</sub>)<sub>3</sub> Cathode. *Adv. Energy Mater.* **2018**, *8*, 1801418.
- (124) Jian, Z.; Han, W.; Lu, X.; Yang, H.; Hu, Y. S.; Zhou, J.; Zhou, Z.; Li, J.; Chen, W.; Chen, D.; Chen, L. Superior Electrochemical Performance and Storage Mechanism of Na<sub>3</sub>V<sub>2</sub>(PO<sub>4</sub>)<sub>3</sub> Cathode for Room-Temperature Sodium-Ion Batteries. *Adv. Energy Mater.* **2013**, *3*, 156–160.
- (125) Gao, H.; Seymour, I. D.; Xin, S.; Xue, L.; Henkelman, G.; Goodenough, J. B. Na<sub>3</sub>MnZr(PO<sub>4</sub>)<sub>3</sub>: A High-Voltage Cathode for Sodium Batteries. *J. Am. Chem. Soc.* **2018**, *140*, 18192–18199.
- (126) Gao, H.; Li, Y.; Park, K.; Goodenough, J. B. Sodium Extraction from NASICON-Structured Na<sub>3</sub>MnTi(PO<sub>4</sub>)<sub>3</sub> through Mn(III)/Mn(II) and Mn(IV)/Mn(III) Redox Couples. *Chem. Mater.* **2016**, *28*, 6553–6559.
- (127) Zhu, T.; Hu, P.; Wang, X.; Liu, Z.; Luo, W.; Owusu, K. A.; Cao, W.; Shi, C.; Li, J.; Zhou, L.; Mai, L. Realizing Three-Electron Redox Reactions in NASICON-Structured Na<sub>3</sub>MnTi(PO<sub>4</sub>)<sub>3</sub> for Sodium-Ion Batteries. *Adv. Energy Mater.* **2019**, *9*, 1803436.
- (128) Lu, Y.; Wang, L.; Cheng, J.; Goodenough, J. B. Prussian Blue: A New Framework of Electrode Materials for Sodium Batteries. *Chem. Commun.* **2012**, *48*, 6544–6546.
- (129) Pei, Y.; Mu, C.; Li, H.; Li, F.; Chen, J. Low-Cost K<sub>4</sub>Fe(CN)<sub>6</sub> as a High-Voltage Cathode for Potassium-Ion Batteries. *ChemSusChem* **2018**, *11*, 1285–1289.
- (130) Wu, X.; Jian, Z.; Li, Z.; Ji, X. Prussian White Analogues as Promising Cathode for Non-Aqueous Potassium-Ion Batteries. *Electrochem. Commun.* **2017**, *77*, 54–57.
- (131) Shadike, Z.; Shi, D.-R.; Wang, T.; Cao, M.-H.; Yang, S.-F.; Chen, J.; Fu, Z.-W. Long Life and High-Rate Berlin Green FeFe(CN)<sub>6</sub> Cathode Material for a Non-Aqueous Potassium-Ion Battery. *J. Mater. Chem. A* **2017**, *5*, 6393–6398.
- (132) Liao, J.; Hu, Q.; Yu, Y.; Wang, H.; Tang, Z.; Wen, Z.; Chen, C. A Potassium-Rich Iron Hexacyanoferrate/Dipotassium Terephthalate@carbon Nanotube Composite Used for K-Ion Full-Cells with an Optimized Electrolyte. *J. Mater. Chem. A* **2017**, *5*, 19017–19024.
- (133) Chong, S.; Chen, Y.; Zheng, Y.; Tan, Q.; Shu, C.; Liu, Y.; Guo, Z. Potassium Ferrous Ferricyanide Nanoparticles as a High Capacity and Ultralong Life Cathode Material for Nonaqueous Potassium-Ion Batteries. *J. Mater. Chem. A* **2017**, *5*, 22465–22471.
- (134) Mizuno, Y.; Okubo, M.; Kagesawa, K.; Asakura, D.; Kudo, T.; Zhou, H.; Oh-Ishi, K.; Okazawa, A.; Kojima, N. Precise Electrochemical Control of Ferromagnetism in a Cyanide-Bridged Bimetallic Coordination Polymer. *Inorg. Chem.* **2012**, *51*, 10311–10316.
- (135) Okubo, M.; Honma, I. Ternary Metal Prussian Blue Analogue Nanoparticles as Cathode Materials for Li-Ion Batteries. *Dalt. Trans.* **2013**, *42*, 15881–15884.
- (136) Wang, B.; Han, Y.; Wang, X.; Bahlawane, N.; Pan, H.; Yan, M.; Jiang, Y. Prussian Blue Analogs for Rechargeable Batteries. *iScience* **2018**, *3*, 110–133.
- (137) Wang, L.; Song, J.; Qiao, R.; Wray, L. A.; Hossain, M. A.; Chuang, Y.-D.; Yang, W.; Lu, Y.; Evans, D.; Lee, J. J.; Vail, S.; Zhao, X.; Nishijima, M.; Kakimoto, S.; Goodenough, J. B. Rhombohedral Prussian White as Cathode for Rechargeable Sodium-Ion Batteries. *J. Am. Chem. Soc.* **2015**, *137*, 2548–2554.
- (138) You, Y.; Wu, X. L.; Yin, Y. X.; Guo, Y. G. A Zero-Strain Insertion Cathode Material of Nickel Ferricyanide for Sodium-Ion Batteries. *J. Mater. Chem. A* **2013**, *1*, 14061–14065.
- (139) Takachi, M.; Matsuda, T.; Moritomo, Y. Cobalt Hexacyanoferrate as Cathode Material for Na<sup>+</sup> Secondary Battery. *Appl. Phys. Express* **2013**, *6*, 025802.
- (140) Xie, M.; Huang, Y.; Xu, M.; Chen, R.; Zhang, X.; Li, L.; Wu, F. Sodium Titanium Hexacyanoferrate as an Environmentally Friendly and Low-Cost Cathode Material for Sodium-Ion Batteries. *J. Power Sources* **2016**, *302*, 7–12.
- (141) Qian, J.; Wu, C.; Cao, Y.; Ma, Z.; Huang, Y.; Ai, X.; Yang, H. Prussian Blue Cathode Materials for Sodium-Ion Batteries and Other Ion Batteries. *Adv. Energy Mater.* **2018**, *8*, 1702619.
- (142) Shibata, T.; Moritomo, Y. Ultrafast Cation Intercalation in Nanoporous Nickel Hexacyanoferrate. *Chem. Commun.* **2014**, *50*, 12941–12943.

- (143) Takachi, M.; Fukuzumi, Y.; Moritomo, Y. Na<sup>+</sup> Diffusion Kinetics in Nanoporous Metal-Hexacyanoferrates. *Dalt. Trans.* **2016**, *45*, 458–461.
- (144) Ling, C.; Chen, J.; Mizuno, F. First-Principles Study of Alkali and Alkaline Earth Ion Intercalation in Iron Hexacyanoferrate: The Important Role of Ionic Radius. *J. Phys. Chem. C* **2013**, *117*, 21158–21165.
- (145) Wu, X.; Wu, C.; Wei, C.; Hu, L.; Qian, J.; Cao, Y.; Ai, X.; Wang, J.; Yang, H. Highly Crystallized Na<sub>2</sub>CoFe(CN)<sub>6</sub> with Suppressed Lattice Defects as Superior Cathode Material for Sodium-Ion Batteries. *ACS Appl. Mater. Interfaces* **2016**, *8*, 5393–5399.
- (146) You, Y.; Wu, X. L.; Yin, Y. X.; Guo, Y. G. High-Quality Prussian Blue Crystals as Superior Cathode Materials for Room-Temperature Sodium-Ion Batteries. *Energy Environ. Sci.* **2014**, *7*, 1643–1647.
- (147) Zhang, C.; Xu, Y.; Zhou, M.; Liang, L.; Dong, H.; Wu, M.; Yang, Y.; Lei, Y. Potassium Prussian Blue Nanoparticles: A Low-Cost Cathode Material for Potassium-Ion Batteries. *Adv. Funct. Mater.* **2017**, *27*, 1604307.
- (148) Chen, H.; Hautier, G.; Ceder, G. Synthesis, Computed Stability, and Crystal Structure of a New Family of Inorganic Compounds: Carbonophosphates. *J. Am. Chem. Soc.* **2012**, *134*, 19619–19627.
- (149) Hautier, G.; Jain, A.; Chen, H.; Moore, C.; Ong, S. P.; Ceder, G. Novel Mixed Polyanions Lithium-Ion Battery Cathode Materials Predicted by High-Throughput Ab Initio Computations. *J. Mater. Chem.* **2011**, *21*, 17147–17153.
- (150) Liao, J.; Hu, Q.; Che, B.; Ding, X.; Chen, F.; Chen, C. Competing with Other Polyanionic Cathode Materials for Potassium-Ion Batteries via Fine Structure Design: New Layered KVOPO<sub>4</sub> with a Tailored Particle Morphology. *J. Mater. Chem. A* **2019**, *7*, 15244–15251.
- (151) Komaba, S.; Hasegawa, T.; Dahbi, M.; Kubota, K. Potassium Intercalation into Graphite to Realize High-Voltage/High-Power Potassium-Ion Batteries and Potassium-Ion Capacitors. *Electrochem. Commun.* **2015**, *60*, 172–175.
- (152) Jian, Z.; Luo, W.; Ji, X. Carbon Electrodes for K-Ion Batteries. *J. Am. Chem. Soc.* **2015**, *137*, 11566–11569.
- (153) Luo, W.; Wan, J.; Ozdemir, B.; Bao, W.; Chen, Y.; Dai, J.; Lin, H.; Xu, Y.; Gu, F.; Barone, V.; Hu, L. Potassium Ion Batteries with Graphitic Materials. *Nano Lett.* **2015**, *15*, 7671–7677.
- (154) Zhao, J.; Zou, X.; Zhu, Y.; Xu, Y.; Wang, C. Electrochemical Intercalation of Potassium into Graphite. *Adv. Funct. Mater.* **2016**, *26*, 8103–8110.
- (155) Tai, Z.; Zhang, Q.; Liu, Y.; Liu, H.; Dou, S. Activated Carbon from the Graphite with Increased Rate Capability for the Potassium Ion Battery. *Carbon* **2017**, *123*, 54–61.
- (156) Wu, X.; Xing, Z.; Hu, Y.; Zhang, Y.; Sun, Y.; Ju, Z.; Liu, J.; Zhuang, Q. Effects of Functional Binders on Electrochemical Performance of Graphite Anode in Potassium-Ion Batteries. *Ionics* **2019**, *25*, 2563–2574.
- (157) Wang, L.; Yang, J.; Li, J.; Chen, T.; Chen, S.; Wu, Z.; Qiu, J.; Wang, B.; Gao, P.; Niu, X.; Li, H. Graphite as a Potassium Ion Battery Anode in Carbonate-Based Electrolyte and Ether-Based Electrolyte. *J. Power Sources* **2019**, *409*, 24–30.
- (158) Liu, Y.; Merinov, B. V.; Goddard, W. A. Origin of Low Sodium Capacity in Graphite and Generally Weak Substrate Binding of Na and Mg among Alkali and Alkaline Earth Metals. *Proc. Natl. Acad. Sci. U. S. A.* **2016**, *113*, 3735–3739.
- (159) Yoon, G.; Kim, H.; Park, I.; Kang, K. Conditions for Reversible Na Intercalation in Graphite: Theoretical Studies on the Interplay Among Guest Ions, Solvent, and Graphite Host. *Adv. Energy Mater.* **2017**, *7*, 1601519.
- (160) Wang, J.; Sorescu, D. C.; Jeon, S.; Belianinov, A.; Kalinin, S. V.; Baddorf, A. P.; MakSYMovich, P. Atomic Intercalation to Measure Adhesion of Graphene on Graphite. *Nat. Commun.* **2016**, *7*, 13263.
- (161) Hasegawa, G.; Kanamori, K.; Kannari, N.; Ozaki, J.-I.; Nakanishi, K.; Abe, T. Hard Carbon Anodes for Na-Ion Batteries: Toward a Practical Use. *ChemElectroChem* **2015**, *2*, 1917–1920.
- (162) Zhao, X.; Ding, Y.; Xu, Q.; Yu, X.; Liu, Y.; Shen, H. Low-Temperature Growth of Hard Carbon with Graphite Crystal for Sodium-Ion Storage with High Initial Coulombic Efficiency: A General Method. *Adv. Energy Mater.* **2019**, *9*, 1803648.
- (163) Wang, K.; Xu, Y.; Li, Y.; Dravid, V.; Wu, J.; Huang, Y. Sodium Storage in Hard Carbon with Curved Graphene Platelets as the Basic Structural Units. *J. Mater. Chem. A* **2019**, *7*, 3327–3335.
- (164) Irisarri, E.; Amini, N.; Tennison, S.; Ghimbeu, C. M.; Gorka, J.; Vix-Guterl, C.; Ponrouch, A.; Palacin, M. R. Optimization of Large Scale Produced Hard Carbon Performance in Na-Ion Batteries: Effect of Precursor, Temperature and Processing Conditions. *J. Electrochem. Soc.* **2018**, *165*, A4058–A4066.
- (165) Harris, P. J. F. Structure of Non-Graphitising Carbons. *Int. Mater. Rev.* **1997**, *42*, 206–218.
- (166) Franklin Rosalind, E.; Randall John, T. Crystallite Growth in Graphitizing and Non-Graphitizing Carbons. *Proc. R. Soc. London. Ser. A. Math. Phys. Sci.* **1951**, *209*, 196–218.
- (167) Harris, P. J. F.; Tsang, S. C. High-Resolution Electron Microscopy Studies of Non-Graphitizing Carbons. *Philos. Mag. A* **1997**, *76*, 667–677.
- (168) Ban, L. L.; Crawford, D.; Marsh, H. Lattice-Resolution Electron Microscopy in Structural Studies of Non-Graphitizing Carbons from Polyvinylidene Chloride (PVDC). *J. Appl. Crystallogr.* **1975**, *8*, 415–420.
- (169) Stevens, D. A.; Dahn, J. R. High Capacity Anode Materials for Rechargeable Sodium-Ion Batteries. *J. Electrochem. Soc.* **2000**, *147*, 1271.
- (170) Deringer, V. L.; Merlet, C.; Hu, Y.; Lee, T. H.; Kattirtzi, J. A.; Pecher, O.; Csányi, G.; Elliott, S. R.; Grey, C. P. Towards an Atomistic Understanding of Disordered Carbon Electrode Materials. *Chem. Commun.* **2018**, *54*, 5988–5991.
- (171) Alvin, S.; Yoon, D.; Chandra, C.; Cahyadi, H. S.; Park, J. H.; Chang, W.; Chung, K. Y.; Kim, J. Revealing Sodium Ion Storage Mechanism in Hard Carbon. *Carbon* **2019**, *145*, 67–81.
- (172) Bai, P.; He, Y.; Zou, X.; Zhao, X.; Xiong, P.; Xu, Y. Elucidation of the Sodium-Storage Mechanism in Hard Carbons. *Adv. Energy Mater.* **2018**, *8*, 1703217.
- (173) Bommier, C.; Surta, T. W.; Dolgos, M.; Ji, X. New Mechanistic Insights on Na-Ion Storage in Nongraphitizable Carbon. *Nano Lett.* **2015**, *15*, 5888–5892.
- (174) Stratford, J. M.; Allan, P. K.; Pecher, O.; Chater, P. A.; Grey, C. P. Mechanistic Insights into Sodium Storage in Hard Carbon Anodes Using Local Structure Probes. *Chem. Commun.* **2016**, *52*, 12430–12433.
- (175) Morita, R.; Gotoh, K.; Kubota, K.; Komaba, S.; Hashi, K.; Shimizu, T.; Ishida, H. Correlation of Carbonization Condition with Metallic Property of Sodium Clusters Formed in Hard Carbon Studied Using <sup>23</sup>Na Nuclear Magnetic Resonance. *Carbon* **2019**, *145*, 712–715.
- (176) Yun, Y. S.; Park, K. Y.; Lee, B.; Cho, S. Y.; Park, Y. U.; Hong, S. J.; Kim, B. H.; Gwon, H.; Kim, H.; Lee, S.; Park, Y. W.; Jin, H. J.; Kang, K. Sodium-Ion Storage in Pyroprotein-Based Carbon Nanoplates. *Adv. Mater.* **2015**, *27*, 6914–6921.
- (177) Han, J.; Xu, M.; Niu, Y.; Li, G. N.; Wang, M.; Zhang, Y.; Jia, M.; Li, C. M. Exploration of K<sub>2</sub>Ti<sub>8</sub>O<sub>17</sub> as an Anode Material for Potassium-Ion Batteries. *Chem. Commun.* **2016**, *52*, 11274–11276.
- (178) Kishore, B.; Venkatesh, G.; Munichandraiah, N. K<sub>2</sub>Ti<sub>4</sub>O<sub>9</sub>: A Promising Anode Material for Potassium Ion Batteries. *J. Electrochem. Soc.* **2016**, *163*, A2551–A2554.
- (179) Li, N.; Zhang, F.; Tang, Y. Hierarchical T-Nb<sub>2</sub>O<sub>5</sub> Nanostructure with Hybrid Mechanisms of Intercalation and Pseudocapacitance for Potassium Storage and High-Performance Potassium Dual-Ion Batteries. *J. Mater. Chem. A* **2018**, *6*, 17889–17895.
- (180) Dong, S.; Li, Z.; Xing, Z.; Wu, X.; Ji, X.; Zhang, X. Novel Potassium-Ion Hybrid Capacitor Based on an Anode of K<sub>2</sub>Ti<sub>6</sub>O<sub>13</sub> Microscaffolds. *ACS Appl. Mater. Interfaces* **2018**, *10*, 15542–15547.
- (181) Lu, M.; Wang, K.-F.; Ke, H.-D.; Hu, Q.; Liu, Z.-H.; Wu, H.-R. Potassium Vanadate K<sub>2</sub>V<sub>3</sub>O<sub>8</sub> as a Superior Anode Material for Potassium-Ion Batteries. *Mater. Lett.* **2018**, *232*, 224–227.

- (182) Naeyaert, P. J. P.; Avdeev, M.; Sharma, N.; Ben Yahia, H.; Ling, C. D. Synthetic, Structural, and Electrochemical Study of Monoclinic  $\text{Na}_4\text{TiSiO}_{12}$  as a Sodium-Ion Battery Anode Material. *Chem. Mater.* **2014**, *26*, 7067–7072.
- (183) Sun, Y.; Zhao, L.; Pan, H.; Lu, X.; Gu, L.; Hu, Y. S.; Li, H.; Armand, M.; Ikuhara, Y.; Chen, L.; Huang, X. Direct Atomic-Scale Confirmation of Three-Phase Storage Mechanism in  $\text{Li}_4\text{Ti}_5\text{O}_{12}$  Anodes for Room-Temperature Sodium-Ion Batteries. *Nat. Commun.* **2013**, *4*, 1870.
- (184) Shen, K.; Wagemaker, M.  $\text{Na}^{2+}\text{XTi}_6\text{O}_{13}$  as Potential Negative Electrode Material for Na-Ion Batteries. *Inorg. Chem.* **2014**, *53*, 8250–8256.
- (185) Rudola, A.; Sharma, N.; Balaya, P. Introducing a 0.2 v Sodium-Ion Battery Anode: The  $\text{Na}_2\text{Ti}_3\text{O}_7$  to  $\text{Na}_3 - \text{XTi}_3\text{O}_7$  Pathway. *Electrochim. Commun.* **2015**, *61*, 10–13.
- (186) Kim, H.; Kim, J. C.; Bianchini, M.; Seo, D. H.; Rodriguez-Garcia, J.; Ceder, G. Recent Progress and Perspective in Electrode Materials for K-Ion Batteries. *Adv. Energy Mater.* **2018**, *8*, 1702384.
- (187) Kim, Y.; Park, Y.; Choi, A.; Choi, N. S.; Kim, J.; Lee, J.; Ryu, J. H.; Oh, S. M.; Lee, K. T. An Amorphous Red Phosphorus/Carbon Composite as a Promising Anode Material for Sodium Ion Batteries. *Adv. Mater.* **2013**, *25*, 3045–3049.
- (188) Chang, W. C.; Wu, J. H.; Chen, K. T.; Tuan, H. Y. Red Phosphorus Potassium-Ion Battery Anodes. *Adv. Sci.* **2019**, *6*, 1801354.
- (189) Nam, D. H.; Hong, K. S.; Lim, S. J.; Kim, T. H.; Kwon, H. S. Electrochemical Properties of Electrodeposited Sn Anodes for Na-Ion Batteries. *J. Phys. Chem. C* **2014**, *118*, 20086–20093.
- (190) Ma, W.; Wang, J.; Gao, H.; Niu, J.; Luo, F.; Peng, Z.; Zhang, Z. A Mesoporous Antimony-Based Nanocomposite for Advanced Sodium Ion Batteries. *Energy Storage Mater.* **2018**, *13*, 247–256.
- (191) Wang, Q.; Zhao, X.; Ni, C.; Tian, H.; Li, J.; Zhang, Z.; Mao, S. X.; Wang, J.; Xu, Y. Reaction and Capacity-Fading Mechanisms of Tin Nanoparticles in Potassium-Ion Batteries. *J. Phys. Chem. C* **2017**, *121*, 12652–12657.
- (192) Xiong, P.; Bai, P.; Tu, S.; Cheng, M.; Zhang, J.; Sun, J.; Xu, Y. Red Phosphorus Nanoparticle@3D Interconnected Carbon Nanosheet Framework Composite for Potassium-Ion Battery Anodes. *Small* **2018**, *14*, 1802140.
- (193) Gabaudan, V.; Berthelot, R.; Stievano, L.; Monconduit, L. Inside the Alloy Mechanism of Sb and Bi Electrodes for K-Ion Batteries. *J. Phys. Chem. C* **2018**, *122*, 18266–18273.
- (194) Chevrier, V. L.; Ceder, G. Challenges for Na-Ion Negative Electrodes. *J. Electrochem. Soc.* **2011**, *158*, A1011.
- (195) Li, X.; Wu, D.; Zhou, Y. N.; Liu, L.; Yang, X. Q.; Ceder, G. O<sub>3</sub>-Type  $\text{Na}(\text{Mn}_0.25\text{Fe}_0.25\text{Co}_0.25\text{Ni}_0.25)\text{O}_2$ : A Quaternary Layered Cathode Compound for Rechargeable Na Ion Batteries. *Electrochim. Commun.* **2014**, *49*, 51–54.
- (196) Wang, D.; Bie, X.; Fu, Q.; Dixon, D.; Bramnik, N.; Hu, Y. S.; Fauth, F.; Wei, Y.; Ehrenberg, H.; Chen, G.; Du, F. Sodium Vanadium Titanium Phosphate Electrode for Symmetric Sodium-Ion Batteries with High Power and Long Lifespan. *Nat. Commun.* **2017**, *8*, 15888.
- (197) Vaalma, C.; Buchholz, D.; Passerini, S. Non-Aqueous Potassium-Ion Batteries: A Review. *Curr. Opin. Electrochem.* **2018**, *9*, 41–48.
- (198) Rajagopalan, R.; Tang, Y.; Ji, X.; Jia, C.; Wang, H. Advancements and Challenges in Potassium Ion Batteries: A Comprehensive Review. *Adv. Funct. Mater.* **2020**, *30*, 1909486.
- (199) Lacivita, V.; Wang, Y.; Bo, S. H.; Ceder, G. Ab Initio Investigation of the Stability of Electrolyte/Electrode Interfaces in All-Solid-State Na Batteries. *J. Mater. Chem. A* **2019**, *7*, 8144–8155.
- (200) Fan, L.; Wei, S.; Li, S.; Li, Q.; Lu, Y. Recent Progress of the Solid-State Electrolytes for High-Energy Metal-Based Batteries. *Adv. Energy Mater.* **2018**, *8*, 1702657.
- (201) Gao, Z.; Sun, H.; Fu, L.; Ye, F.; Zhang, Y.; Luo, W.; Huang, Y. Promises, Challenges, and Recent Progress of Inorganic Solid-State Electrolytes for All-Solid-State Lithium Batteries. *Adv. Mater.* **2018**, *30*, 1705702.
- (202) Solid Power, BMW Partner to Develop Next-Generation EV Batteries; Reuters, 2019; <https://www.reuters.com/article/us-bmw-solid-power/bmw-partner-to-develop-next-generation-ev-batteries-idUSKBN1EC16V> (accessed 2019-06-17).
- (203) Toyota Set to Sell Long-Range, Fast-Charging Electric Cars in 2022: Paper; Reuters, 2019; <https://www.reuters.com/article/us-toyota-electric-cars-idUSKBN1AA035> (accessed 2019-06-17).
- (204) Hyundai Motor Solely Developing EV Batteries; Korea Herald, 2017; <http://www.koreaherald.com/view.php?ud=20170405000762> (accessed 2019-06-17).
- (205) Han, X.; Gong, Y.; Fu, K.; He, X.; Hitz, G. T.; Dai, J.; Pearse, A.; Liu, B.; Wang, H.; Rubloff, G.; Mo, Y.; Thangadurai, V.; Wachsman, E. D.; Hu, L. Negating Interfacial Impedance in Garnet-Based Solid-State Li Metal Batteries. *Nat. Mater.* **2017**, *16*, 572–579.
- (206) Kato, Y.; Hori, S.; Saito, T.; Suzuki, K.; Hirayama, M.; Mitsui, A.; Yonemura, M.; Iba, H.; Kanno, R. High-Power All-Solid-State Batteries Using Sulfide Superionic Conductors. *Nat. Energy* **2016**, *1*, 16030.
- (207) Fu, K. K.; Gong, Y.; Liu, B.; Zhu, Y.; Xu, S.; Yao, Y.; Luo, W.; Wang, C.; Lacey, S. D.; Dai, J.; Chen, Y.; Mo, Y.; Wachsman, E.; Hu, L. Toward Garnet Electrolyte-Based Li Metal Batteries: An Ultrathin, Highly Effective, Artificial Solid-State Electrolyte/Metallic Li Interface. *Sci. Adv.* **2017**, *3*, e1601659.
- (208) Shi, T.; Tu, Q.; Tian, Y.; Xiao, Y.; Miara, L. J.; Kononova, O.; Ceder, G. High Active Material Loading in All-Solid-State Battery Electrode via Particle Size Optimization. *Adv. Energy Mater.* **2020**, *10*, 1902881.
- (209) Liu, T.; Zhang, Y.; Chen, R.; Zhao, S. X.; Lin, Y.; Nan, C. W.; Shen, Y. Non-Successive Degradation in Bulk-Type All-Solid-State Lithium Battery with Rigid Interfacial Contact. *Electrochim. Commun.* **2017**, *79*, 1–4.
- (210) Arya, A.; Sharma, A. L. Polymer Electrolytes for Lithium Ion Batteries: A Critical Study. *Ionics* **2017**, *23*, 497–540.
- (211) Jensen, C. Tesla Says Car Fire Started in Battery. The New York Times. 2013; p B6.
- (212) Alex, Hern. Samsung Must Act Fast to Keep an Exploding Phone from Blowing up Its Brand. *The Guardian*. 2016.
- (213) Liu, J.; Bao, Z.; Cui, Y.; Dufek, E. J.; Goodenough, J. B.; Khalifah, P.; Li, Q.; Liaw, B. Y.; Liu, P.; Manthiram, A.; Meng, Y. S.; Subramanian, V. R.; Toney, M. F.; Viswanathan, V. V.; Whittingham, M. S.; Xiao, J.; Xu, W.; Yang, J.; Yang, X. Q.; Zhang, J. G. *Pathways for Practical High-Energy Long-Cycling Lithium Metal Batteries*; Nature Publishing Group, 2019; Vol. 4, pp 180–186.
- (214) Cheng, E. J.; Sharafi, A.; Sakamoto, J. Intergranular Li Metal Propagation through Polycrystalline  $\text{Li}_6.25\text{Al}_0.25\text{La}_3\text{Zr}_2\text{O}_{12}$  Ceramic Electrolyte. *Electrochim. Acta* **2017**, *223*, 85–91.
- (215) Porz, L.; Swamy, T.; Sheldon, B. W.; Rettenwander, D.; Frömling, T.; Thaman, H. L.; Berendts, S.; Uecker, R.; Carter, W. C.; Chiang, Y. M. Mechanism of Lithium Metal Penetration through Inorganic Solid Electrolytes. *Adv. Energy Mater.* **2017**, *7*, 1701003.
- (216) Kamaya, N.; Homma, K.; Yamakawa, Y.; Hirayama, M.; Kanno, R.; Yonemura, M.; Kamiyama, T.; Kato, Y.; Hama, S.; Kawamoto, K.; Mitsui, A. A Lithium Superionic Conductor. *Nat. Mater.* **2011**, *10*, 682–686.
- (217) Barroso-Luque, L.; Tu, Q.; Ceder, G. An Analysis of Solid-State Electrodeposition-Induced Metal Plastic Flow and Predictions of Stress States in Solid Ionic Conductor Defects. *J. Electrochem. Soc.* **2020**, *167*, 020534.
- (218) Wang, Y.; Richards, W. D.; Ong, S. P.; Miara, L. J.; Kim, J. C.; Mo, Y.; Ceder, G. Design Principles for Solid-State Lithium Superionic Conductors. *Nat. Mater.* **2015**, *14*, 1026–1031.
- (219) Ohno, S.; Banik, A.; Dewald, G. F.; Kraft, M. A.; Krauskopf, T.; Minafra, N.; Till, P.; Weiss, M.; Zeier, W. G. Materials Design of Ionic Conductors for Solid State Batteries. *Prog. Energy* **2020**, *2*, 022001.
- (220) Zhang, Z.; Shao, Y.; Lotsch, B.; Hu, Y. S.; Li, H.; Janek, J.; Nazar, L. F.; Nan, C. W.; Maier, J.; Armand, M.; Chen, L. New Horizons for Inorganic Solid State Ion Conductors. *Energy Environ. Sci.* **2018**, *11*, 1945–1976.
- (221) Kraft, M. A.; Culver, S. P.; Calderon, M.; Böcher, F.; Krauskopf, T.; Senyshyn, A.; Dietrich, C.; Zevalkink, A.; Janek, J.; Zeier, W. G. Influence of Lattice Polarizability on the Ionic Conductivity in the

- Lithium Superionic Argyrodites Li<sub>6</sub>PSSX (X = Cl, Br, I). *J. Am. Chem. Soc.* **2017**, *139*, 10909–10918.
- (222) He, X.; Zhu, Y.; Mo, Y. Origin of Fast Ion Diffusion in SuperIonic Conductors. *Nat. Commun.* **2017**, *8*, 15893.
- (223) Ceder, G.; Ong, S. P.; Wang, Y. Predictive Modeling and Design Rules for Solid Electrolytes. *MRS Bull.* **2018**, *43*, 746–751.
- (224) Nolan, A. M.; Zhu, Y.; He, X.; Bai, Q.; Mo, Y. Computation-Accelerated Design of Materials and Interfaces for All-Solid-State Lithium-Ion Batteries. *Joule* **2018**, *2*, 2016–2046.
- (225) Richards, W. D.; Miara, L. J.; Wang, Y.; Kim, J. C.; Ceder, G. Interface Stability in Solid-State Batteries. *Chem. Mater.* **2016**, *28*, 266–273.
- (226) Richards, W. D.; Tsujimura, T.; Miara, L. J.; Wang, Y.; Kim, J. C.; Ong, S. P.; Uechi, I.; Suzuki, N.; Ceder, G. Design and Synthesis of the Superionic Conductor Na<sub>10</sub>SnP<sub>2</sub>S<sub>12</sub>. *Nat. Commun.* **2016**, *7*, 11009.
- (227) Zhang, Y.; He, X.; Chen, Z.; Bai, Q.; Nolan, A. M.; Roberts, C. A.; Banerjee, D.; Matsunaga, T.; Mo, Y.; Ling, C. Unsupervised Discovery of Solid-State Lithium Ion Conductors. *Nat. Commun.* **2019**, *10*, 5260.
- (228) Zhu, Z.; Chu, I. H.; Ong, S. P. Li<sub>3</sub>Y(PS<sub>4</sub>)<sub>2</sub> and Li<sub>5</sub>PS<sub>4</sub>Cl<sub>2</sub>: New Lithium Superionic Conductors Predicted from Silver Thio-phosphates Using Efficiently Tiered Ab Initio Molecular Dynamics Simulations. *Chem. Mater.* **2017**, *29*, 2474–2484.
- (229) Wang, Y.; Richards, W. D.; Bo, S. H.; Miara, L. J.; Ceder, G. Computational Prediction and Evaluation of Solid-State Sodium Superionic Conductors Na<sub>7</sub>P<sub>3</sub>X<sub>11</sub> (X = O, S, Se). *Chem. Mater.* **2017**, *29*, 7475–7482.
- (230) Murayama, M.; Sonoyama, N.; Yamada, A.; Kanno, R. Material Design of New Lithium Ionic Conductor, Thio-LISICON, in the Li<sub>2</sub>S-P<sub>2</sub>S System. *Solid State Ionics* **2004**, *170*, 173–180.
- (231) Xu, X.; Wen, Z.; Gu, Z.; Xu, X.; Lin, Z. Lithium Ion Conductive Glass Ceramics in the System Li<sub>1.4</sub>Al<sub>0.4</sub>(Ge<sub>1</sub>-XTix)1.6(PO<sub>4</sub>)<sub>3</sub> (X = 0–1.0). *Solid State Ionics* **2004**, *171*, 207–213.
- (232) Thangadurai, V.; Weppner, W. Li<sub>6</sub>Al<sub>2</sub>Ta<sub>2</sub>O<sub>12</sub> (A = Sr, Ba): Novel Garnet-like Oxides for Fast Lithium Ion Conduction. *Adv. Funct. Mater.* **2005**, *15*, 107–112.
- (233) Yamane, H.; Shibata, M.; Shimane, Y.; Junke, T.; Seino, Y.; Adams, S.; Minami, K.; Hayashi, A.; Tatsumisago, M. Crystal Structure of a Superionic Conductor, Li<sub>7</sub>P<sub>3</sub>S<sub>11</sub>. *Solid State Ionics* **2007**, *178*, 1163–1167.
- (234) Murugan, R.; Thangadurai, V.; Weppner, W. Fast Lithium Ion Conduction in Garnet-Type Li<sub>7</sub>La<sub>3</sub>Zr<sub>2</sub>O<sub>12</sub>. *Angew. Chem., Int. Ed.* **2007**, *46*, 7778–7781.
- (235) Deiseroth, H. J.; Kong, S. T.; Eckert, H.; Vannahme, J.; Reiner, C.; Zaif, T.; Schlosser, M. Li<sub>6</sub>PS<sub>5</sub>X: A Class of Crystalline Li-Rich Solids with an Unusually High Li<sup>+</sup> Mobility. *Angew. Chem., Int. Ed.* **2008**, *47*, 755–758.
- (236) Maekawa, H.; Matsuo, M.; Takamura, H.; Ando, M.; Noda, Y.; Karahashi, T.; Orimo, S. I. Halide-Stabilized LiBH<sub>4</sub>, a Room-Temperature Lithium Fast-Ion Conductor. *J. Am. Chem. Soc.* **2009**, *131*, 894–895.
- (237) Matsuo, M.; Remhof, A.; Martelli, P.; Caputo, R.; Ernst, M.; Miura, Y.; Sato, T.; Oguchi, H.; Maekawa, H.; Takamura, H.; Borgschulte, A.; Züttel, A.; Orimo, S. I. Complex Hydrides with (BH<sub>4</sub>)<sup>-</sup> and (NH<sub>2</sub>)<sup>-</sup> Anions as New Lithium Fast-Ion Conductors. *J. Am. Chem. Soc.* **2009**, *131*, 16389–16391.
- (238) Matsuo, M.; Sato, T.; Miura, Y.; Oguchi, H.; Zhou, Y.; Maekawa, H.; Takamura, H.; Orimo, S. I. Synthesis and Lithium Fast-Ion Conductivity of a New Complex Hydride Li<sub>3</sub>(NH<sub>2</sub>)<sub>2</sub>I with Double-Layered Structure. *Chem. Mater.* **2010**, *22*, 2702–2704.
- (239) Gao, Y. X.; Wang, X. P.; Wang, W. G.; Zhuang, Z.; Zhang, D. M.; Fang, Q. F. Synthesis, Ionic Conductivity, and Chemical Compatibility of Garnet-like Lithium Ionic Conductor Li<sub>5</sub>La<sub>3</sub>Bi<sub>2</sub>O<sub>12</sub>. *Solid State Ionics* **2010**, *181*, 1415–1419.
- (240) Alpen, U. V.; Rabenau, A.; Talat, G. H. Ionic Conductivity in Li<sub>3</sub>N Single Crystals. *Appl. Phys. Lett.* **1977**, *30*, 621–623.
- (241) Ohta, S.; Kobayashi, T.; Asaoka, T. High Lithium Ionic Conductivity in the Garnet-Type Oxide Li<sub>7-X</sub>La<sub>3</sub>(Zr<sub>2-X</sub>, Nb<sub>X</sub>)O<sub>12</sub> (X = 0–2). *J. Power Sources* **2011**, *196*, 3342–3345.
- (242) Li, Y.; Han, J. T.; Wang, C. A.; Xie, H.; Goodenough, J. B. Optimizing Li<sup>+</sup> Conductivity in a Garnet Framework. *J. Mater. Chem.* **2012**, *22*, 15357–15361.
- (243) Zhao, Y.; Daemen, L. L. Superionic Conductivity in Lithium-Rich Anti-Perovskites. *J. Am. Chem. Soc.* **2012**, *134*, 15042–15047.
- (244) Bron, P.; Johansson, S.; Zick, K.; Schmedt auf der Günne, J.; Dehnen, S.; Roling, B. Li<sub>10</sub>SnP<sub>2</sub>S<sub>12</sub>: An Affordable Lithium Superionic Conductor. *J. Am. Chem. Soc.* **2013**, *135*, 15694–15697.
- (245) Liu, Z.; Fu, W.; Payzant, E. A.; Yu, X.; Wu, Z.; Dudney, N. J.; Kiggans, J.; Hong, K.; Rondonone, A. J.; Liang, C. Anomalous High Ionic Conductivity of Nanoporous β-Li<sub>3</sub>PS<sub>4</sub>. *J. Am. Chem. Soc.* **2013**, *135*, 975–978.
- (246) Kuhn, A.; Duppel, V.; Lotsch, B. V. Tetragonal Li<sub>10</sub>GeP<sub>2</sub>S<sub>12</sub> and Li<sub>7</sub>GePS<sub>8</sub>-Exploring the Li Ion Dynamics in LGPS Li Electrolytes. *Energy Environ. Sci.* **2013**, *6*, 3548–3552.
- (247) Rangasamy, E.; Liu, Z.; Gobet, M.; Pilar, K.; Sahu, G.; Zhou, W.; Wu, H.; Greenbaum, S.; Liang, C. An Iodide-Based Li<sub>7</sub>P<sub>2</sub>S<sub>8</sub>I Superionic Conductor. *J. Am. Chem. Soc.* **2015**, *137*, 1384–1387.
- (248) Tang, W. S.; Unemoto, A.; Zhou, W.; Stavila, V.; Matsuo, M.; Wu, H.; Oriomo, S. I.; Udovic, T. J. Unparalleled Lithium and Sodium Superionic Conduction in Solid Electrolytes with Large Monovalent Cage-like Anions. *Energy Environ. Sci.* **2015**, *8*, 3637–3645.
- (249) Tang, W. S.; Yoshida, K.; Soloninina, A. V.; Skoryunov, R. V.; Babanova, O. A.; Skripov, A. V.; Dimitrieva, M.; Stavila, V.; Oriomo, S. I.; Udovic, T. J. Stabilizing Superionic-Conducting Structures via Mixed-Anion Solid Solutions of Monocarba-Closo-Borate Salts. *ACS Energy Lett.* **2016**, *1*, 659–664.
- (250) Richards, W. D.; Wang, Y.; Miara, L. J.; Kim, J. C.; Ceder, G. Design of Li<sub>1</sub>+2:XZn<sub>1</sub>-XPS<sub>4</sub>, a New Lithium Ion Conductor. *Energy Environ. Sci.* **2016**, *9*, 3272–3278.
- (251) Kennedy, J. H.; Yang, Y. Glass-Forming Region and Structure in SiS<sub>2</sub>Li<sub>2</sub>SLiX (X = Br, I). *J. Solid State Chem.* **1987**, *69*, 252–257.
- (252) Wu, J. F.; Chen, E. Y.; Yu, Y.; Liu, L.; Wu, Y.; Pang, W. K.; Peterson, V. K.; Guo, X. Gallium-Doped Li<sub>7</sub>La<sub>3</sub>Zr<sub>2</sub>O<sub>12</sub> Garnet-Type Electrolytes with High Lithium-Ion Conductivity. *ACS Appl. Mater. Interfaces* **2017**, *9*, 1542–1552.
- (253) Yan, Y.; Kühnel, R. S.; Remhof, A.; Duchêne, L.; Reyes, E. C.; Rentsch, D.; Łódziana, Z.; Battaglia, C. A Lithium Amide-Borohydride Solid-State Electrolyte with Lithium-Ion Conductivities Comparable to Liquid Electrolytes. *Adv. Energy Mater.* **2017**, *7*, 1700294.
- (254) Sedlmaier, S. J.; Indris, S.; Dietrich, C.; Yavuz, M.; Dräger, C.; Von Seggern, F.; Sommer, H.; Janek, J. Li<sub>4</sub>PS<sub>4</sub>I: A Li<sup>+</sup> Superionic Conductor Synthesized by a Solvent-Based Soft Chemistry Approach. *Chem. Mater.* **2017**, *29*, 1830–1835.
- (255) Asano, T.; Sakai, A.; Ouchi, S.; Sakaida, M.; Miyazaki, A.; Hasegawa, S. Solid Halide Electrolytes with High Lithium-Ion Conductivity for Application in 4 V Class Bulk-Type All-Solid-State Batteries. *Adv. Mater.* **2018**, *30*, 1803075.
- (256) Aono, H.; Sugimoto, E.; Sadaoka, Y.; Imanaka, N.; Adachi, G.-Y. Ionic Conductivity of Solid Electrolytes Based on Lithium Titanium Phosphate. *J. Electrochem. Soc.* **1990**, *137*, 1023.
- (257) Itoh, M.; Inaguma, Y.; Jung, W. H.; Chen, L.; Nakamura, T. High Lithium Ion Conductivity in the Perovskite-Type Compounds Ln<sub>1</sub>2Li<sub>1</sub>2TiO<sub>3</sub> (Ln = La, Pr, Nd, Sm). *Solid State Ionics* **1994**, *70*–*71*, 203–207.
- (258) Kanno, R.; Murayama, M. Lithium Ionic Conductor Thio-LISICON: The Li<sub>[Sub 2]S-GeS<sub>[Sub 2]</sub>-P<sub>[Sub 2]S<sub>[Sub 5]</sub></sub> System. *J. Electrochem. Soc.* **2001**, *148*, A742.</sub>
- (259) Hayashi, A.; Hama, S.; Morimoto, H.; Tatsumisago, M.; Minami, T. Preparation of Li<sub>2</sub>S-P<sub>2</sub>S<sub>5</sub> Amorphous Solid Electrolytes by Mechanical Milling. *J. Am. Ceram. Soc.* **2001**, *84*, 477–479.
- (260) Thangadurai, V.; Kaack, H.; Weppner, W. J. F. Novel Fast Lithium Ion Conduction in Garnet-Type Li<sub>5</sub>La<sub>3</sub>M<sub>2</sub>O<sub>12</sub> (M = Nb, Ta). *J. Am. Ceram. Soc.* **2003**, *86*, 437–440.
- (261) Murayama, M.; Kanno, R.; Irie, M.; Ito, S.; Hata, T.; Sonoyama, N.; Kawamoto, Y. Synthesis of New Lithium Ionic Conductor Thio-

- LISICON - Lithium Silicon Sulfides System. *J. Solid State Chem.* **2002**, *168*, 140–148.
- (262) Hong, H. Y. P. Crystal Structures and Crystal Chemistry in the System  $\text{Na}_{1+x}\text{Zr}_2\text{Si}_x\text{P}_3\text{-XO}_{12}$ . *Mater. Res. Bull.* **1976**, *11*, 173–182.
- (263) Vogel, E. M.; Cava, R. J.; Rietman, E.  $\text{Na}^+$  Ion Conductivity and Crystallographic Cell Characterization in the Hf-Nasicon System  $\text{Na}_{1+x}\text{Hf}_2\text{Si}_x\text{P}_3\text{-XO}_{12}$ . *Solid State Ionics* **1984**, *14*, 1–6.
- (264) Takahashi, T.; Kuwabara, K.; Shibata, M. Solid-State Ionics - Conductivities of  $\text{Na}^+$  Ion Conductors Based on NASICON. *Solid State Ionics* **1980**, *1*, 163–175.
- (265) Hooper, A. A Study of the Electrical Properties of Single-Crystal and Polycrystalline  $\beta$ -Alumina Using Complex Plane Analysis. *J. Phys. D: Appl. Phys.* **1977**, *10*, 1487–1496.
- (266) Ribes, M.; Barrau, B.; Souquet, J. L. Sulfide Glasses: Glass Forming Region, Structure and Ionic Conduction of Glasses in  $\text{Na}_2\text{SX}_2$  (XSi; Ge),  $\text{Na}_2\text{SP}_2\text{S}_5$  and  $\text{Li}_2\text{SGeS}_2$  Systems. *J. Non-Cryst. Solids* **1980**, *38–39*, 271–276.
- (267) Banerjee, A.; Park, K. H.; Heo, J. W.; Nam, Y. J.; Moon, C. K.; Oh, S. M.; Hong, S. T.; Jung, Y. S.  $\text{Na}_3\text{SbS}_4$ : A Solution Processable Sodium Superionic Conductor for All-Solid-State Sodium-Ion Batteries. *Angew. Chem., Int. Ed.* **2016**, *55*, 9634–9638.
- (268) Song, S.; Duong, H. M.; Korsunsky, A. M.; Hu, N.; Lu, L. A  $\text{Na}^+$  Superionic Conductor for Room-Temperature Sodium Batteries. *Sci. Rep.* **2016**, *6*, 32330.
- (269) Chu, I. H.; Kompella, C. S.; Nguyen, H.; Zhu, Z.; Hy, S.; Deng, Z.; Meng, Y. S.; Ong, S. P. Room-Temperature All-Solid-State Rechargeable Sodium-Ion Batteries with a Cl-Doped  $\text{Na}_3\text{PS}_4$  Superionic Conductor. *Sci. Rep.* **2016**, *6*, 33733.
- (270) Yu, Z.; Shang, S. L.; Seo, J. H.; Wang, D.; Luo, X.; Huang, Q.; Chen, S.; Lu, J.; Li, X.; Liu, Z. K.; Wang, D. Exceptionally High Ionic Conductivity in  $\text{Na}_3\text{P}_0.62\text{As}_0.38\text{S}_4$  with Improved Moisture Stability for Solid-State Sodium-Ion Batteries. *Adv. Mater.* **2017**, *29*, 1605561.
- (271) Duchêne, L.; Kühnel, R. S.; Rentsch, D.; Remhof, A.; Hagemann, H.; Battaglia, C. A Highly Stable Sodium Solid-State Electrolyte Based on a Dodeca/Deca-Borate Equimolar Mixture. *Chem. Commun.* **2017**, *53*, 4195–4198.
- (272) Zhang, Z.; Ramos, E.; Lalère, F.; Assoud, A.; Kaup, K.; Hartman, P.; Nazar, L. F.  $\text{Na}_{11}\text{Sn}_2\text{PS}_{12}$ : A New Solid State Sodium Superionic Conductor. *Energy Environ. Sci.* **2018**, *11*, 87–93.
- (273) Hayashi, A.; Noi, K.; Sakuda, A.; Tatsumisago, M. Superionic Glass-Ceramic Electrolytes for Room-Temperature Rechargeable Sodium Batteries. *Nat. Commun.* **2012**, *3*, 856.
- (274) Matsuo, M.; Kuromoto, S.; Sato, T.; Oguchi, H.; Takamura, H.; Orimo, S. I. Sodium Ionic Conduction in Complex Hydrides with  $[\text{BH}_4]$  - and  $[\text{NH}_2]$  - Anions. *Appl. Phys. Lett.* **2012**, *100*, 203904.
- (275) Udoovic, T. J.; Matsuo, M.; Unemoto, A.; Verdal, N.; Stavila, V.; Skripov, A. V.; Rush, J. J.; Takamura, H.; Orimo, S. I. Sodium Superionic Conduction in  $\text{Na}_2\text{B}_{12}\text{H}_{12}$ . *Chem. Commun.* **2014**, *50*, 3750–3752.
- (276) Udoovic, T. J.; Matsuo, M.; Tang, W. S.; Wu, H.; Stavila, V.; Solonin, A. V.; Skoryunov, R. V.; Babanova, O. A.; Skripov, A. V.; Rush, J. J.; Unemoto, A.; Takamura, H.; Orimo, S. I. Exceptional Superionic Conductivity in Disordered Sodium Decahydro-Closodecaborate. *Adv. Mater.* **2014**, *26*, 7622–7626.
- (277) Tanibata, N.; Noi, K.; Hayashi, A.; Tatsumisago, M. Preparation and Characterization of Highly Sodium Ion Conducting  $\text{Na}_3\text{PS}_4\text{-Na}_4\text{Si}_4\text{S}_4$  Solid Electrolytes. *RSC Adv.* **2014**, *4*, 17120–17123.
- (278) Bo, S. H.; Wang, Y.; Kim, J. C.; Richards, W. D.; Ceder, G. Computational and Experimental Investigations of Na-Ion Conduction in Cubic  $\text{Na}_3\text{PSe}_4$ . *Chem. Mater.* **2016**, *28*, 252–258.
- (279) Wang, Y.; Wang, Q.; Liu, Z.; Zhou, Z.; Li, S.; Zhu, J.; Zou, R.; Wang, Y.; Lin, J.; Zhao, Y. Structural Manipulation Approaches towards Enhanced Sodium Ionic Conductivity in Na-Rich Antiperovskites. *J. Power Sources* **2015**, *293*, 735–740.
- (280) Higashi, S.; Miwa, K.; Aoki, M.; Takechi, K. A Novel Inorganic Solid State Ion Conductor for Rechargeable Mg Batteries. *Chem. Commun.* **2014**, *50*, 1320–1322.
- (281) Canepa, P.; Bo, S.-H.; Sai Gautam, G.; Key, B.; Richards, W. D.; Shi, T.; Tian, Y.; Wang, Y.; Li, J.; Ceder, G. High Magnesium Mobility in Ternary Spinel Chalcogenides. *Nat. Commun.* **2017**, *8*, 1759.
- (282) Sun, Y.; Wang, Y.; Liang, X.; Xia, Y.; Peng, L.; Jia, H.; Li, H.; Bai, L.; Feng, J.; Jiang, H.; Xie, J. Rotational Cluster Anion Enabling Superionic Conductivity in Sodium-Rich Antiperovskite  $\text{Na}_3\text{OBH}_4$ . *J. Am. Chem. Soc.* **2019**, *141*, 5640.
- (283) Moon, C. K.; Lee, H. J.; Park, K. H.; Kwak, H.; Heo, J. W.; Choi, K.; Yang, H.; Kim, M. S.; Hong, S. T.; Lee, J. H.; Jung, Y. S. Vacancy-Driven  $\text{Na}^+$  Superionic Conduction in New Ca-Doped  $\text{Na}_3\text{PS}_4$  for All-Solid-State Na-Ion Batteries. *ACS Energy Lett.* **2018**, *3*, 2504–2512.
- (284) Xu, M.; Park, M. S.; Lee, J. M.; Kim, T. Y.; Park, Y. S.; Ma, E. Mechanisms of  $\text{Li}^+$  Transport in Garnet-Type Cubic  $\text{Li}_{3+x}\text{La}_{3\text{M}}\text{O}_{2\text{x}}$  ( $\text{M} = \text{Te}, \text{Nb}, \text{Zr}$ ). *Phys. Rev. B: Condens. Matter Mater. Phys.* **2012**, *85*, 052301.
- (285) Tian, Y.; Shi, T.; Richards, W. D.; Li, J.; Kim, J. C.; Bo, S. H.; Ceder, G. Compatibility Issues between Electrodes and Electrolytes in Solid-State Batteries. *Energy Environ. Sci.* **2017**, *10*, 1150–1166.
- (286) Han, F.; Zhu, Y.; He, X.; Mo, Y.; Wang, C. Electrochemical Stability of  $\text{Li}_{10}\text{GeP}_2\text{S}_{12}$  and  $\text{Li}_7\text{La}_3\text{Zr}_2\text{O}_{12}$  Solid Electrolytes. *Adv. Energy Mater.* **2016**, *6*, 1501590.
- (287) Koerver, R.; Aygün, I.; Leichtweiss, T.; Dietrich, C.; Zhang, W.; Binder, J. O.; Hartmann, P.; Zeier, W. G.; Janek, J. Capacity Fade in Solid-State Batteries: Interphase Formation and Chemomechanical Processes in Nickel-Rich Layered Oxide Cathodes and Lithium Thiophosphate Solid Electrolytes. *Chem. Mater.* **2017**, *29*, 5574–5582.
- (288) Koerver, R.; Zhang, W.; De Biasi, L.; Schweidler, S.; Kondrakov, A. O.; Kolling, S.; Brezesinski, T.; Hartmann, P.; Zeier, W. G.; Janek, J. Chemo-Mechanical Expansion of Lithium Electrode Materials-on the Route to Mechanically Optimized All-Solid-State Batteries. *Energy Environ. Sci.* **2018**, *11*, 2142–2158.
- (289) Tu, Q.; Barroso-Luque, L.; Shi, T.; Ceder, G. Electrodeposition and Mechanical Stability at Lithium-Solid Electrolyte Interface during Plating in Solid-State Batteries Electrodeposition and Mechanical Stability at Lithium-Solid Electrolyte Interface during Plating in Solid-State Batteries. *Cell Reports Phys. Sci.* **2020**, *1*, 100106.
- (290) Randau, S.; Weber, D. A.; Kötz, O.; Koerver, R.; Braun, P.; Weber, A.; Ivers-Tiffée, E.; Adermann, T.; Kulisch, J.; Zeier, W. G.; Richter, F. H.; Janek, J. Benchmarking the Performance of All-Solid-State Lithium Batteries. *Nat. Energy* **2020**, *5*, 259–270.
- (291) Jiang, Z.; Wang, S.; Chen, X.; Yang, W.; Yao, X.; Hu, X.; Han, Q.; Wang, H. Tape-Casting  $\text{Li}_{0.34}\text{La}_{0.56}\text{TiO}_3$  Ceramic Electrolyte Films Permit High Energy Density of Lithium-Metal Batteries. *Adv. Mater.* **2020**, *32*, 1906221.
- (292) Liu, Y.; Sun, Q.; Wang, D.; Adair, K.; Liang, J.; Sun, X. Development of the Cold Sintering Process and Its Application in Solid-State Lithium Batteries. *J. Power Sources* **2018**, *393*, 193–203.
- (293) Kato, Y.; Shiotani, S.; Morita, K.; Suzuki, K.; Hirayama, M.; Kanno, R. All-Solid-State Batteries with Thick Electrode Configurations. *J. Phys. Chem. Lett.* **2018**, *9*, 607–613.
- (294) Yi, E.; Wang, W.; Kieffer, J.; Laine, R. M. Flame Made Nanoparticles Permit Processing of Dense, Flexible,  $\text{Li}^+$  Conducting Ceramic Electrolyte Thin Films of Cubic- $\text{Li}_7\text{La}_3\text{Zr}_2\text{O}_{12}$  (c-LLZO). *J. Mater. Chem. A* **2016**, *4*, 12947–12954.
- (295) Nam, Y. J.; Cho, S. J.; Oh, D. Y.; Lim, J. M.; Kim, S. Y.; Song, J. H.; Lee, Y. G.; Lee, S. Y.; Jung, Y. S. Bendable and Thin Sulfide Solid Electrolyte Film: A New Electrolyte Opportunity for Free-Standing and Stackable High-Energy All-Solid-State Lithium-Ion Batteries. *Nano Lett.* **2015**, *15*, 3317–3323.
- (296) Seino, Y.; Ota, T.; Takada, K.; Hayashi, A.; Tatsumisago, M. A Sulphide Lithium Super Ion Conductor Is Superior to Liquid Ion Conductors for Use in Rechargeable Batteries. *Energy Environ. Sci.* **2014**, *7*, 627–631.
- (297) Hayashi, A.; Muramatsu, H.; Ohtomo, T.; Hama, S.; Tatsumisago, M. Improvement of Chemical Stability of  $\text{Li}_3\text{PS}_4$  Glass Electrolytes by Adding  $\text{MxO}_y$  ( $\text{M} = \text{Fe}, \text{Zn}$ , and  $\text{Bi}$ ) Nanoparticles. *J. Mater. Chem. A* **2013**, *1*, 6320–6326.

- (298) Rangasamy, E.; Sahu, G.; Keum, J. K.; Rondinone, A. J.; Dudney, N. J.; Liang, C. A High Conductivity Oxide-Sulfide Composite Lithium Superionic Conductor. *J. Mater. Chem. A* **2014**, *2*, 4111–4116.
- (299) Kotobuki, M.; Kanamura, K. Fabrication of All-Solid-State Battery Using Li<sub>5</sub>La<sub>3</sub>Ta<sub>2</sub>O<sub>12</sub> Ceramic Electrolyte. *Ceram. Int.* **2013**, *39*, 6481–6487.
- (300) Kotobuki, M.; Kanamura, K.; Sato, Y.; Yoshida, T. Fabrication of All-Solid-State Lithium Battery with Lithium Metal Anode Using Al<sub>2</sub>O<sub>3</sub>-Added Li<sub>7</sub>La<sub>3</sub>Zr<sub>2</sub>O<sub>12</sub> Solid Electrolyte. *J. Power Sources* **2011**, *196*, 7750–7754.
- (301) Han, F.; Gao, T.; Zhu, Y.; Gaskell, K. J.; Wang, C. A Battery Made from a Single Material. *Adv. Mater.* **2015**, *27*, 3473–3483.
- (302) Zhu, Y.; He, X.; Mo, Y. Strategies Based on Nitride Materials Chemistry to Stabilize Li Metal Anode. *Adv. Sci.* **2017**, *4*, 1600517.
- (303) Xiao, Y.; Miara, L. J.; Wang, Y.; Ceder, G. Computational Screening of Cathode Coatings for Solid-State Batteries. *Joule* **2019**, *3*, 1252–1275.
- (304) Xiao, Y.; Wang, Y.; Bo, S. H.; Kim, J. C.; Miara, L. J.; Ceder, G. Understanding Interface Stability in Solid-State Batteries. *Nature Reviews Materials* **2020**, *5*, 105–126.
- (305) Zhang, W.; Weber, D. A.; Weigand, H.; Arlt, T.; Manke, I.; Schröder, D.; Koerver, R.; Leichtweiss, T.; Hartmann, P.; Zeier, W. G.; Janek, J. Interfacial Processes and Influence of Composite Cathode Microstructure Controlling the Performance of All-Solid-State Lithium Batteries. *ACS Appl. Mater. Interfaces* **2017**, *9*, 17835–17845.
- (306) Culver, S. P.; Koerver, R.; Zeier, W. G.; Janek, J. On the Functionality of Coatings for Cathode Active Materials in Thiophosphate-Based All-Solid-State Batteries. *Adv. Energy Mater.* **2019**, *9*, 1900626.
- (307) Sakuda, A.; Hayashi, A.; Tatsumisago, M. Interfacial Observation between LiCoO<sub>2</sub> Electrode and Li<sub>2</sub>S-P<sub>2</sub>S<sub>5</sub> Solid Electrolytes of All-Solid-State Lithium Secondary Batteries Using Transmission Electron Microscopy. *Chem. Mater.* **2010**, *22*, 949–956.
- (308) Zhu, Y.; He, X.; Mo, Y. First Principles Study on Electrochemical and Chemical Stability of Solid Electrolyte-Electrode Interfaces in All-Solid-State Li-Ion Batteries. *J. Mater. Chem. A* **2016**, *4*, 3253–3266.
- (309) Xu, L.; Tang, S.; Cheng, Y.; Wang, K.; Liang, J.; Liu, C.; Cao, Y. C.; Wei, F.; Mai, L. Interfaces in Solid-State Lithium Batteries. *Joule* **2018**, *2*, 1991–2015.
- (310) Chu, I. H.; Nguyen, H.; Hy, S.; Lin, Y. C.; Wang, Z.; Xu, Z.; Deng, Z.; Meng, Y. S.; Ong, S. P. Insights into the Performance Limits of the Li<sub>7</sub>P<sub>3</sub>S<sub>11</sub> Superionic Conductor: A Combined First-Principles and Experimental Study. *ACS Appl. Mater. Interfaces* **2016**, *8*, 7843–7853.
- (311) Zhao, N.; Khokhar, W.; Bi, Z.; Shi, C.; Guo, X.; Fan, L. Z.; Nan, C. W. Solid Garnet Batteries. *Joule* **2019**, *3*, 1190–1199.
- (312) Ohta, N.; Takada, K.; Sakaguchi, I.; Zhang, L.; Ma, R.; Fukuda, K.; Osada, M.; Sasaki, T. LiNbO<sub>3</sub>-Coated LiCoO<sub>2</sub> as Cathode Material for All Solid-State Lithium Secondary Batteries. *Electrochim. Commun.* **2007**, *9*, 1486–1490.
- (313) Takada, K.; Ohta, N.; Zhang, L.; Xu, X.; Hang, B. T.; Ohnishi, T.; Osada, M.; Sasaki, T. Interfacial Phenomena in Solid-State Lithium Battery with Sulfide Solid Electrolyte. *Solid State Ionics* **2012**, *225*, 594–597.
- (314) Takada, K.; Ohta, N.; Zhang, L.; Fukuda, K.; Sakaguchi, I.; Ma, R.; Osada, M.; Sasaki, T. Interfacial Modification for High-Power Solid-State Lithium Batteries. *Solid State Ionics* **2008**, *179*, 1333–1337.
- (315) Ito, S.; Fujiki, S.; Yamada, T.; Aihara, Y.; Park, Y.; Kim, T. Y.; Baek, S. W.; Lee, J. M.; Doo, S.; Machida, N. A Rocking Chair Type All-Solid-State Lithium Ion Battery Adopting Li<sub>2</sub>O-ZrO<sub>2</sub> Coated LiNi<sub>0.8</sub>Co<sub>0.15</sub>Al<sub>0.05</sub>O<sub>2</sub> and a Sulfide Based Electrolyte. *J. Power Sources* **2014**, *248*, 943–950.
- (316) Zhang, Y.; Tian, Y.; Xiao, Y.; Miara, L. J.; Aihara, Y.; Tsujimura, T.; Shi, T.; Scott, M. C.; Ceder, G. Direct Visualization of the Interfacial Degradation of Cathode Coatings in Solid State Batteries: A Combined Experimental and Computational Study. *Adv. Energy Mater.* **2020**, *10*, 1903778.
- (317) Tian, Y.; Sun, Y.; Hannah, D. C.; Xiao, Y.; Liu, H.; Chapman, K. W.; Bo, S. H.; Ceder, G. Reactivity-Guided Interface Design in Na Metal Solid-State Batteries. *Joule* **2019**, *3*, 1037–1050.
- (318) Wenzel, S.; Weber, D. A.; Leichtweiss, T.; Busche, M. R.; Sann, J.; Janek, J. Interphase Formation and Degradation of Charge Transfer Kinetics between a Lithium Metal Anode and Highly Crystalline Li<sub>7</sub>P<sub>3</sub>S<sub>11</sub> Solid Electrolyte. *Solid State Ionics* **2016**, *286*, 24–33.
- (319) Santhanagopalan, D.; Qian, D.; McGilvray, T.; Wang, Z.; Wang, F.; Camino, F.; Graetz, J.; Dudney, N.; Meng, Y. S. Interface Limited Lithium Transport in Solid-State Batteries. *J. Phys. Chem. Lett.* **2014**, *5*, 298–303.
- (320) Sicolo, S.; Fingerle, M.; Hausbrand, R.; Albe, K. Interfacial Instability of Amorphous LiPON against Lithium: A Combined Density Functional Theory and Spectroscopic Study. *J. Power Sources* **2017**, *354*, 124–133.
- (321) Xie, J.; Imanishi, N.; Zhang, T.; Hirano, A.; Takeda, Y.; Yamamoto, O. Li-Ion Transport in All-Solid-State Lithium Batteries with LiCoO<sub>2</sub> Using NASICON-Type Glass Ceramic Electrolytes. *J. Power Sources* **2009**, *189*, 365–370.
- (322) Wenzel, S.; Sedlmaier, S. J.; Dietrich, C.; Zeier, W. G.; Janek, J. Interfacial Reactivity and Interphase Growth of Argyrodite Solid Electrolytes at Lithium Metal Electrodes. *Solid State Ionics* **2018**, *318*, 102–112.
- (323) Auvergniot, J.; Cassel, A.; Ledeuil, J. B.; Viallet, V.; Seznec, V.; Dedryvère, R. Interface Stability of Argyrodite Li<sub>6</sub>PSSCl toward LiCoO<sub>2</sub>, LiNi<sub>1/3</sub>Co<sub>1/3</sub>Mn<sub>1/3</sub>O<sub>2</sub>, and LiMn<sub>2</sub>O<sub>4</sub> in Bulk All-Solid-State Batteries. *Chem. Mater.* **2017**, *29*, 3883–3890.
- (324) Emly, A.; Kioupakis, E.; Van Der Ven, A. Phase Stability and Transport Mechanisms in Antiperovskite Li<sub>3</sub>OCl and Li<sub>3</sub>OBr Superionic Conductors. *Chem. Mater.* **2013**, *25*, 4663–4670.
- (325) Miara, L. J.; Suzuki, N.; Richards, W. D.; Wang, Y.; Kim, J. C.; Ceder, G. Li-Ion Conductivity in Li<sub>9</sub>S<sub>3</sub>N. *J. Mater. Chem. A* **2015**, *3*, 20338–20344.
- (326) Zhang, Z.; Zhang, L.; Yan, X.; Wang, H.; Liu, Y.; Yu, C.; Cao, X.; van Eijck, L.; Wen, B. All-in-One Improvement toward Li<sub>6</sub>PSSBr-Based Solid Electrolytes Triggered by Compositional Tune. *J. Power Sources* **2019**, *410*, 411, 162–170.
- (327) Suyama, M.; Kato, A.; Sakuda, A.; Hayashi, A.; Tatsumisago, M. Lithium Dissolution/Deposition Behavior with Li<sub>3</sub>PS<sub>4</sub>-LiI Electrolyte for All-Solid-State Batteries Operating at High Temperatures. *Electrochim. Acta* **2018**, *286*, 158–162.
- (328) Wu, E. A.; Kompella, C. S.; Zhu, Z.; Lee, J. Z.; Lee, S. C.; Chu, I. H.; Nguyen, H.; Ong, S. P.; Banerjee, A.; Meng, Y. S. New Insights into the Interphase between the Na Metal Anode and Sulfide Solid-State Electrolytes: A Joint Experimental and Computational Study. *ACS Appl. Mater. Interfaces* **2018**, *10*, 10076–10086.
- (329) Wang, M. J.; Choudhury, R.; Sakamoto, J. Characterizing the Li-Solid-Electrolyte Interface Dynamics as a Function of Stack Pressure and Current Density. *Joule* **2019**, *3*, 2165–2178.
- (330) Kasemchainan, J.; Zekoll, S.; Spencer Jolly, D.; Ning, Z.; Hartley, G. O.; Marrow, J.; Bruce, P. G. Critical Stripping Current Leads to Dendrite Formation on Plating in Lithium Anode Solid Electrolyte Cells. *Nat. Mater.* **2019**, *18*, 1105–1111.
- (331) Krauskopf, T.; Mogwitz, B.; Rosenbach, C.; Zeier, W. G.; Janek, J. Diffusion Limitation of Lithium Metal and Li-Mg Alloy Anodes on LLZO Type Solid Electrolytes as a Function of Temperature and Pressure. *Adv. Energy Mater.* **2019**, *9*, 1902568.
- (332) Lee, Y. G.; Fujiki, S.; Jung, C.; Suzuki, N.; Yashiro, N.; Omoda, R.; Ko, D. S.; Shiratsuchi, T.; Sugimoto, T.; Ryu, S.; Ku, J. H.; Watanabe, T.; Park, Y.; Aihara, Y.; Im, D.; Han, I. T. High-Energy Long-Cycling All-Solid-State Lithium Metal Batteries Enabled by Silver-Carbon Composite Anodes. *Nat. Energy* **2020**, *5*, 299–308.
- (333) Lee, J. Z.; Wynn, T. A.; Schroeder, M. A.; Alvarado, J.; Wang, X.; Xu, K.; Meng, Y. S. Cryogenic Focused Ion Beam Characterization of Lithium Metal Anodes. *ACS Energy Lett.* **2019**, *4*, 489–493.
- (334) Hartmann, P.; Leichtweiss, T.; Busche, M. R.; Schneider, M.; Reich, M.; Sann, J.; Adelhelm, P.; Janek, J. Degradation of NASICON-Type Materials in Contact with Lithium Metal: Formation of Mixed

- Conducting Interphases (MCI) on Solid Electrolytes. *J. Phys. Chem. C* **2013**, *117*, 21064–21074.
- (335) Wenzel, S.; Leichtweiss, T.; Weber, D. A.; Sann, J.; Zeier, W. G.; Janek, J. Interfacial Reactivity Benchmarking of the Sodium Ion Conductors Na<sub>3</sub>PS<sub>4</sub> and Sodium  $\beta$ -Alumina for Protected Sodium Metal Anodes and Sodium All-Solid-State Batteries. *ACS Appl. Mater. Interfaces* **2016**, *8*, 28216–28224.
- (336) Monroe, C.; Newman, J. The Impact of Elastic Deformation on Deposition Kinetics at Lithium/Polymer Interfaces. *J. Electrochem. Soc.* **2005**, *152*, A396.
- (337) Taylor, N. J.; Stangeland-Molo, S.; Haslam, C. G.; Sharafi, A.; Thompson, T.; Wang, M.; Garcia-Mendez, R.; Sakamoto, J. Demonstration of High Current Densities and Extended Cycling in the Garnet Li<sub>7</sub>La<sub>3</sub>Zr<sub>2</sub>O<sub>12</sub> Solid Electrolyte. *J. Power Sources* **2018**, *396*, 314–318.
- (338) Sharafi, A.; Meyer, H. M.; Nanda, J.; Wolfenstine, J.; Sakamoto, J. Characterizing the Li-Li<sub>7</sub>La<sub>3</sub>Zr<sub>2</sub>O<sub>12</sub> Interface Stability and Kinetics as a Function of Temperature and Current Density. *J. Power Sources* **2016**, *302*, 135–139.
- (339) Sharafi, A.; Kazyak, E.; Davis, A. L.; Yu, S.; Thompson, T.; Siegel, D. J.; Dasgupta, N. P.; Sakamoto, J. Surface Chemistry Mechanism of Ultra-Low Interfacial Resistance in the Solid-State Electrolyte Li<sub>7</sub>La<sub>3</sub>Zr<sub>2</sub>O<sub>12</sub>. *Chem. Mater.* **2017**, *29*, 7961–7968.
- (340) Tsai, C. L.; Roddatis, V.; Chandran, C. V.; Ma, Q.; Uhlenbruck, S.; Bram, M.; Heijmans, P.; Guillon, O. Li<sub>7</sub>La<sub>3</sub>Zr<sub>2</sub>O<sub>12</sub> Interface Modification for Li Dendrite Prevention. *ACS Appl. Mater. Interfaces* **2016**, *8*, 10617–10626.
- (341) Garcia-Mendez, R.; Mizuno, F.; Zhang, R.; Arthur, T. S.; Sakamoto, J. Effect of Processing Conditions of 75Li<sub>2</sub>S-25P<sub>2</sub>S<sub>5</sub> Solid Electrolyte on Its DC Electrochemical Behavior. *Electrochim. Acta* **2017**, *237*, 144–151.
- (342) Han, F.; Yue, J.; Zhu, X.; Wang, C. Suppressing Li Dendrite Formation in Li<sub>2</sub>S-P<sub>2</sub>S<sub>5</sub> Solid Electrolyte by LiI Incorporation. *Adv. Energy Mater.* **2018**, *8*, 1703644.
- (343) Qian, J.; Henderson, W. A.; Xu, W.; Bhattacharya, P.; Engelhard, M.; Borodin, O.; Zhang, J. G. High Rate and Stable Cycling of Lithium Metal Anode. *Nat. Commun.* **2015**, *6*, 6362.
- (344) Choudhury, S.; Archer, L. A. Lithium Fluoride Additives for Stable Cycling of Lithium Batteries at High Current Densities. *Adv. Electron. Mater.* **2016**, *2*, 1500246.
- (345) Swamy, T.; Park, R.; Sheldon, B. W.; Rettenwander, D.; Porz, L.; Berendts, S.; Uecker, R.; Carter, W. C.; Chiang, Y.-M. Lithium Metal Penetration Induced by Electrodeposition through Solid Electrolytes: Example in Single-Crystal Li<sub>6</sub>La<sub>3</sub>ZrTaO<sub>12</sub> Garnet. *J. Electrochem. Soc.* **2018**, *165*, A3648–A3655.
- (346) Tian, H.-K.; Qi, Y. Simulation of the Effect of Contact Area Loss in All-Solid-State Li-Ion Batteries. *J. Electrochem. Soc.* **2017**, *164*, E3512–E3521.
- (347) Raj, R.; Wolfenstine, J. Current Limit Diagrams for Dendrite Formation in Solid-State Electrolytes for Li-Ion Batteries. *J. Power Sources* **2017**, *343*, 119–126.
- (348) Sudo, R.; Nakata, Y.; Ishiguro, K.; Matsui, M.; Hirano, A.; Takeda, Y.; Yamamoto, O.; Imanishi, N. Interface Behavior between Garnet-Type Lithium-Conducting Solid Electrolyte and Lithium Metal. *Solid State Ionics* **2014**, *262*, 151–154.
- (349) Ishiguro, K.; Nemori, H.; Sunahiro, S.; Nakata, Y.; Sudo, R.; Matsui, M.; Takeda, Y.; Yamamoto, O.; Imanishi, N. Ta-Doped Li<sub>7</sub>La<sub>3</sub>Zr<sub>2</sub>O<sub>12</sub> for Water-Stable Lithium Electrode of Lithium-Air Batteries. *J. Electrochem. Soc.* **2014**, *161*, A668–A674.
- (350) Han, F.; Westover, A. S.; Yue, J.; Fan, X.; Wang, F.; Chi, M.; Leonard, D. N.; Dudney, N. J.; Wang, H.; Wang, C. High Electronic Conductivity as the Origin of Lithium Dendrite Formation within Solid Electrolytes. *Nat. Energy* **2019**, *4*, 187–196.
- (351) Kato, A.; Nose, M.; Yamamoto, M.; Sakuda, A.; Hayashi, A.; Tatsumisago, M. Mechanical Properties of Sulfide Glasses in All-Solid-State Batteries. *J. Ceram. Soc. Jpn.* **2018**, *126*, 719–727.
- (352) Sakuda, A.; Hayashi, A.; Tatsumisago, M. Sulfide Solid Electrolyte with Favorable Mechanical Property for All-Solid-State Lithium Battery. *Sci. Rep.* **2013**, *3*, 2261.
- (353) McGrogan, F. P.; Swamy, T.; Bishop, S. R.; Eggleton, E.; Porz, L.; Chen, X.; Chiang, Y. M.; Van Vliet, K. J. Compliant Yet Brittle Mechanical Behavior of Li<sub>2</sub>S-P<sub>2</sub>S<sub>5</sub> Lithium-Ion-Conducting Solid Electrolyte. *Adv. Energy Mater.* **2017**, *7*, 1602011.
- (354) Sakuda, A.; Takeuchi, T.; Kobayashi, H. Electrode Morphology in All-Solid-State Lithium Secondary Batteries Consisting of LiNi<sub>1</sub>/3Co<sub>1</sub>/3Mn<sub>1</sub>/3O<sub>2</sub> and Li<sub>2</sub>S-P<sub>2</sub>S<sub>5</sub> Solid Electrolytes. *Solid State Ionics* **2016**, *285*, 112–117.
- (355) Yamamoto, M.; Takahashi, M.; Terauchi, Y.; Kobayashi, Y.; Ikeda, S.; Sakuda, A. Fabrication of Composite Positive Electrode Sheet with High Active Material Content and Effect of Fabrication Pressure for All-Solid-State Battery. *J. Ceram. Soc. Jpn.* **2017**, *125*, 391–395.
- (356) Ohta, N.; Takada, K.; Zhang, L.; Ma, R.; Osada, M.; Sasaki, T. Enhancement of the High-Rate Capability of Solid-State Lithium Batteries by Nanoscale Interfacial Modification. *Adv. Mater.* **2006**, *18*, 2226–2229.
- (357) Choi, S.; Jeon, M.; Ahn, J.; Jung, W. D.; Choi, S. M.; Kim, J. S.; Lim, J.; Jang, Y. J.; Jung, H. G.; Lee, J. H.; Sang, B. I.; Kim, H. Quantitative Analysis of Microstructures and Reaction Interfaces on Composite Cathodes in All-Solid-State Batteries Using a Three-Dimensional Reconstruction Technique. *ACS Appl. Mater. Interfaces* **2018**, *10*, 23740–23747.
- (358) Park, K. H.; Bai, Q.; Kim, D. H.; Oh, D. Y.; Zhu, Y.; Mo, Y.; Jung, Y. S. Design Strategies, Practical Considerations, and New Solution Processes of Sulfide Solid Electrolytes for All-Solid-State Batteries. *Adv. Energy Mater.* **2018**, *8*, 1800035.
- (359) Teragawa, S.; Aso, K.; Tadanaga, K.; Hayashi, A.; Tatsumisago, M. Liquid-Phase Synthesis of a Li<sub>3</sub>PS<sub>4</sub> Solid Electrolyte Using N-Methylformamide for All-Solid-State Lithium Batteries. *J. Mater. Chem. A* **2014**, *2*, 5095–5099.
- (360) Yubuchi, S.; Teragawa, S.; Aso, K.; Tadanaga, K.; Hayashi, A.; Tatsumisago, M. Preparation of High Lithium-Ion Conducting Li<sub>6</sub>P<sub>5</sub>Cl<sub>3</sub> Solid Electrolyte from Ethanol Solution for All-Solid-State Lithium Batteries. *J. Power Sources* **2015**, *293*, 941–945.
- (361) Choi, Y. E.; Park, K. H.; Kim, D. H.; Oh, D. Y.; Kwak, H. R.; Lee, Y. G.; Jung, Y. S. Coatable Li<sub>4</sub>SnS<sub>4</sub> Solid Electrolytes Prepared from Aqueous Solutions for All-Solid-State Lithium-Ion Batteries. *ChemSusChem* **2017**, *10*, 2605–2611.
- (362) Rosero-Navarro, N. C.; Miura, A.; Tadanaga, K. Composite Cathode Prepared by Argyrodite Precursor Solution Assisted by Dispersant Agents for Bulk-Type All-Solid-State Batteries. *J. Power Sources* **2018**, *396*, 33–40.
- (363) Kim, D. H.; Oh, D. Y.; Park, K. H.; Choi, Y. E.; Nam, Y. J.; Lee, H. A.; Lee, S. M.; Jung, Y. S. Infiltration of Solution-Processable Solid Electrolytes into Conventional Li-Ion-Battery Electrodes for All-Solid-State Li-Ion Batteries. *Nano Lett.* **2017**, *17*, 3013–3020.
- (364) Wolfenstine, J.; Allen, J. L.; Sakamoto, J.; Siegel, D. J.; Choe, H. Mechanical Behavior of Li-Ion-Conducting Crystalline Oxide-Based Solid Electrolytes: A Brief Review. *Ionics* **2018**, *24*, 1271–1276.
- (365) Ni, J. E.; Case, E. D.; Sakamoto, J. S.; Rangasamy, E.; Wolfenstine, J. B. Room Temperature Elastic Moduli and Vickers Hardness of Hot-Pressed LLZO Cubic Garnet. *J. Mater. Sci.* **2012**, *47*, 7978–7985.
- (366) Cho, Y. H.; Wolfenstine, J.; Rangasamy, E.; Kim, H.; Choe, H.; Sakamoto, J. Mechanical Properties of the Solid Li-Ion Conducting Electrolyte: Li<sub>0.33</sub>La<sub>0.57</sub>TiO<sub>3</sub>. *J. Mater. Sci.* **2012**, *47*, 5970–5977.
- (367) Miara, L.; Windmüller, A.; Tsai, C. L.; Richards, W. D.; Ma, Q.; Uhlenbruck, S.; Guillon, O.; Ceder, G. About the Compatibility between High Voltage Spinel Cathode Materials and Solid Oxide Electrolytes as a Function of Temperature. *ACS Appl. Mater. Interfaces* **2016**, *8*, 26842–26850.
- (368) Wakasugi, J.; Munakata, H.; Kanamura, K. Thermal Stability of Various Cathode Materials against Li<sub>6.25</sub>Al<sub>0.25</sub>La<sub>3</sub>Zr<sub>2</sub>O<sub>12</sub> Electrolyte. *Electrochemistry* **2017**, *85*, 77–81.
- (369) Ohta, S.; Komagata, S.; Seki, J.; Saeki, T.; Morishita, S.; Asaoka, T. Short Communication All-Solid-State Lithium Ion Battery Using Garnet-Type Oxide and Li<sub>3</sub>BO<sub>3</sub> Solid Electrolytes Fabricated by Screen-Printing. *J. Power Sources* **2013**, *238*, 53–56.

- (370) Chen, R. J.; Zhang, Y. B.; Liu, T.; Xu, B. Q.; Lin, Y. H.; Nan, C. W.; Shen, Y. Addressing the Interface Issues in All-Solid-State Bulk-Type Lithium Ion Battery via an All-Composite Approach. *ACS Appl. Mater. Interfaces* **2017**, *9*, 9654–9661.
- (371) Zhang, J.; Zang, X.; Wen, H.; Dong, T.; Chai, J.; Li, Y.; Chen, B.; Zhao, J.; Dong, S.; Ma, J.; Yue, L.; Liu, Z.; Guo, X.; Cui, G.; Chen, L. High-Voltage and Free-Standing Poly(Propylene Carbonate)/Li6.75-La3Zr1.75Ta0.25O12 Composite Solid Electrolyte for Wide Temperature Range and Flexible Solid Lithium Ion Battery. *J. Mater. Chem. A* **2017**, *5*, 4940–4948.
- (372) Shi, T.; Zhang, Y. Q.; Tu, Q.; Wang, Y.; Scott, M. C.; Ceder, G. Characterization of Mechanical Degradation in an All-Solid-State Battery Cathode. *J. Mater. Chem. A* **2020**, *8*, 17399–17404.
- (373) Inada, T.; Kobayashi, T.; Sonoyama, N.; Yamada, A.; Kondo, S.; Nagao, M.; Kanno, R. All Solid-State Sheet Battery Using Lithium Inorganic Solid Electrolyte, Thio-LISICON. *J. Power Sources* **2009**, *194*, 1085–1088.
- (374) Strauss, F.; Bartsch, T.; De Biasi, L.; Kim, A. Y.; Janek, J.; Hartmann, P.; Brezesinski, T. Impact of Cathode Material Particle Size on the Capacity of Bulk-Type All-Solid-State Batteries. *ACS Energy Lett.* **2018**, *3*, 992–996.
- (375) Calpa, M.; Rosero-Navarro, N. C.; Miura, A.; Tadanaga, K. Electrochemical Performance of Bulk-Type All-Solid-State Batteries Using Small-Sized Li7P3S11 Solid Electrolyte Prepared by Liquid Phase as the Ionic Conductor in the Composite Cathode. *Electrochim. Acta* **2019**, *296*, 473–480.
- (376) Wan, H.; Mwizerwa, J. P.; Qi, X.; Xu, X.; Li, H.; Zhang, Q.; Cai, L.; Hu, Y. S.; Yao, X. Nanoscaled Na3PS4 Solid Electrolyte for All-Solid-State FeS2/Na Batteries with Ultrahigh Initial Coulombic Efficiency of 95% and Excellent Cyclic Performances. *ACS Appl. Mater. Interfaces* **2018**, *10*, 12300–12304.
- (377) Bielefeld, A.; Weber, D. A.; Janek, J. Microstructural Modeling of Composite Cathodes for All-Solid-State Batteries. *J. Phys. Chem. C* **2019**, *123*, 1626–1634.
- (378) Nam, Y. J.; Oh, D. Y.; Jung, S. H.; Jung, Y. S. Toward Practical All-Solid-State Lithium-Ion Batteries with High Energy Density and Safety: Comparative Study for Electrodes Fabricated by Dry- and Slurry-Mixing Processes. *J. Power Sources* **2018**, *375*, 93–101.
- (379) Lobe, S.; Dellen, C.; Finsterbusch, M.; Gehrke, H. G.; Sebold, D.; Tsai, C. L.; Uhlenbruck, S.; Guillou, O. Radio Frequency Magnetron Sputtering of Li7La3Zr2O12 Thin Films for Solid-State Batteries. *J. Power Sources* **2016**, *307*, 684–689.
- (380) Kalita, D. J.; Lee, S. H.; Lee, K. S.; Ko, D. H.; Yoon, Y. S. Ionic Conductivity Properties of Amorphous Li-La-Zr-O Solid Electrolyte for Thin Film Batteries. *Solid State Ionics* **2012**, *229*, 14–19.
- (381) Nong, J.; Xu, H.; Yu, Z.; Zhu, G.; Yu, A. Properties and Preparation of Li-La-Ti-Zr-O Thin Film Electrolyte. *Mater. Lett.* **2015**, *154*, 167–169.
- (382) Saccoccia, M.; Yu, J.; Lu, Z.; Kwok, S. C. T.; Wang, J.; Yeung, K. K.; Yuen, M. M. F.; Ciucci, F. Low Temperature Pulsed Laser Deposition of Garnet Li6.4La3Zr1.4Ta0.6O12 Films as All Solid-State Lithium Battery Electrolytes. *J. Power Sources* **2017**, *365*, 43–52.
- (383) Park, J. S.; Cheng, L.; Zorba, V.; Mehta, A.; Cabana, J.; Chen, G.; Doeff, M. M.; Richardson, T. J.; Park, J. H.; Son, J. W.; Hong, W. S. Effects of Crystallinity and Impurities on the Electrical Conductivity of Li-La-Zr-O Thin Films. *Thin Solid Films* **2015**, *576*, 55–60.
- (384) Ogawa, M.; Kanda, R.; Yoshida, K.; Uemura, T.; Harada, K. High-Capacity Thin Film Lithium Batteries with Sulfide Solid Electrolytes. *J. Power Sources* **2012**, *205*, 487–490.
- (385) Nisula, M.; Shindo, Y.; Koga, H.; Karppinen, M. Atomic Layer Deposition of Lithium Phosphorus Oxynitride. *Chem. Mater.* **2015**, *27*, 6987–6993.
- (386) Kazyak, E.; Chen, K. H.; Wood, K. N.; Davis, A. L.; Thompson, T.; Bielinski, A. R.; Sanchez, A. J.; Wang, X.; Wang, C.; Sakamoto, J.; Dasgupta, N. P. Atomic Layer Deposition of the Solid Electrolyte Garnet Li7La3Zr2O12. *Chem. Mater.* **2017**, *29*, 3785–3792.
- (387) Perng, Y. C.; Cho, J.; Sun, S. Y.; Membreno, D.; Cirigliano, N.; Dunn, B.; Chang, J. P. Synthesis of Ion Conducting  $\text{Li}_x\text{Al}_y\text{Si}_z\text{O}$  Thin Films by Atomic Layer Deposition. *J. Mater. Chem. A* **2014**, *2*, 9566–9573.
- (388) Geng, L.; Lv, G.; Xing, X.; Guo, J. Reversible Electrochemical Intercalation of Aluminum in Mo6S8. *Chem. Mater.* **2015**, *27*, 4926–4929.
- (389) Yang, H.; Li, H.; Li, J.; Sun, Z.; He, K.; Cheng, H. M.; Li, F. The Rechargeable Aluminum Battery: Opportunities and Challenges. *Angew. Chem., Int. Ed.* **2019**, *58*, 11978–11996.
- (390) Ponrouch, A.; Bitenc, J.; Dominko, R.; Lindahl, N.; Johansson, P.; Palacin, M. R. Multivalent Rechargeable Batteries. *Energy Storage Mater.* **2019**, *20*, 253–262.
- (391) Monti, D.; Ponrouch, A.; Araujo, R. B.; Barde, F.; Johansson, P.; Palacin, M. R. Multivalent Batteries—Prospects for High Energy Density: Ca Batteries. *Front. Chem.* **2019**, *7*, 79.
- (392) Matsui, M. Study on Electrochemically Deposited Mg Metal. *J. Power Sources* **2011**, *196*, 7048–7055.
- (393) Wu, Y. A.; Yin, Z.; Farmand, M.; Yu, Y. S.; Shapiro, D. A.; Liao, H. G.; Liang, W. I.; Chu, Y. H.; Zheng, H. In-Situ Multimodal Imaging and Spectroscopy of Mg Electrodeposition at Electrode-Electrolyte Interfaces. *Sci. Rep.* **2017**, *7*, 42527.
- (394) Yoo, H. D.; Shterenberg, I.; Gofer, Y.; Gershinsky, G.; Pour, N.; Aurbach, D. Mg Rechargeable Batteries: An on-Going Challenge. *Energy Environ. Sci.* **2013**, *6*, 2265–2279.
- (395) Besenhard, J. O.; Winter, M. Advances in Battery Technology: Rechargeable Magnesium Batteries and Novel Negative-Electrode Materials for Lithium Ion Batteries. *ChemPhysChem* **2002**, *3*, 155–159.
- (396) Aurbach, D.; Lu, Z.; Schechter, A.; Gofer, Y.; Gizbar, H.; Turgeman, R.; Cohen, Y.; Moshkovich, M.; Levi, E. Prototype Systems for Rechargeable Magnesium Batteries. *Nature* **2000**, *407*, 724–727.
- (397) Shao, Y.; Liu, T.; Li, G.; Gu, M.; Nie, Z.; Engelhard, M.; Xiao, J.; Lv, D.; Wang, C.; Zhang, J.-G.; Liu, J. Coordination Chemistry in Magnesium Battery Electrolytes: How Ligands Affect Their Performance. *Sci. Rep.* **2013**, *3*, 3130.
- (398) Kitada, A.; Kang, Y.; Uchimoto, Y.; Murase, K. Room-Temperature Electrodeposition of Mg Metal from Amide Salts Dissolved in Glyme-Ionic Liquid Mixture. *J. Electrochem. Soc.* **2014**, *161*, D102–D106.
- (399) Kitada, A.; Kang, Y.; Matsumoto, K.; Fukami, K.; Hagiwara, R.; Murase, K. Room Temperature Magnesium Electrodeposition from Glyme-Coordinated Ammonium Amide Electrolytes. *J. Electrochem. Soc.* **2015**, *162*, D389–D396.
- (400) Jäckle, M.; Helmbrecht, K.; Smits, M.; Stottmeister, D.; Groß, A. Self-Diffusion Barriers: Possible Descriptors for Dendrite Growth in Batteries? *Energy Environ. Sci.* **2018**, *11*, 3400–3407.
- (401) Aurbach, D. Review of Selected Electrode-Solution Interactions Which Determine the Performance of Li and Li Ion Batteries. *J. Power Sources* **2000**, *89*, 206–218.
- (402) Aurbach, D.; Zinigrad, E.; Teller, H.; Dan, P. Factors Which Limit the Cycle Life of Rechargeable Lithium (Metal) Batteries. *J. Electrochem. Soc.* **2000**, *147*, 1274.
- (403) Aurbach, D.; Zinigrad, E.; Cohen, Y.; Teller, H. A Short Review of Failure Mechanisms of Lithium Metal and Lithiated Graphite Anodes in Liquid Electrolyte Solutions. *Solid State Ionics* **2002**, *148*, 405–416.
- (404) Davidson, R.; Verma, A.; Santos, D.; Hao, F.; Fincher, C.; Xiang, S.; Van Buskirk, J.; Xie, K.; Pharr, M.; Mukherjee, P. P.; Banerjee, S. Formation of Magnesium Dendrites during Electrodeposition. *ACS Energy Lett.* **2019**, *4*, 375–376.
- (405) Ding, M. S.; Diemant, T.; Behm, R. J.; Passerini, S.; Giffin, G. A. Dendrite Growth in Mg Metal Cells Containing Mg(TFSI)2 /Glyme Electrolytes. *J. Electrochem. Soc.* **2018**, *165*, A1983–A1990.
- (406) Ponrouch, A.; Frontera, C.; Bardé, F.; Palacín, M. R. Towards a Calcium-Based Rechargeable Battery. *Nat. Mater.* **2016**, *15*, 169–172.
- (407) Aurbach, D.; Skaletsky, R.; Gofer, Y. The Electrochemical Behavior of Calcium Electrodes in a Few Organic Electrolytes. *J. Electrochem. Soc.* **1991**, *138*, 3536–3545.
- (408) Wang, D.; Gao, X.; Chen, Y.; Jin, L.; Kuss, C.; Bruce, P. G. Plating and Stripping Calcium in an Organic Electrolyte. *Nat. Mater.* **2018**, *17*, 16–20.

- (409) Shyamsunder, A.; Blanc, L. E.; Assoud, A.; Nazar, L. F. Reversible Calcium Plating and Stripping at Room Temperature Using a Borate Salt. *ACS Energy Lett.* **2019**, *4*, 2271–2276.
- (410) Biria, S.; Pathreker, S.; Genier, F. S.; Li, H.; Hosein, I. D. Plating and Stripping Calcium at Room Temperature in an Ionic-Liquid Electrolyte. *ACS Appl. Energy Mater.* **2020**, *3*, 2310–2314.
- (411) Li, Z.; Fuhr, O.; Fichtner, M.; Zhao-Karger, Z. Towards Stable and Efficient Electrolytes for Room-Temperature Rechargeable Calcium Batteries. *Energy Environ. Sci.* **2019**, *12*, 3496–3501.
- (412) Meitav, A.; Peled, E. Calcium - Ca (AlCl<sub>4</sub>)<sub>2</sub> - Thionyl Chloride Cell: Performance and Safety. *J. Electrochem. Soc.* **1982**, *129*, 451–457.
- (413) Aurbach, D.; Berthelot, R.; Ponrouch, A.; Salama, M.; Shterenberg, I. Battery Systems Based on Multivalent Metals and Metal Ions. In *Prospects For Li-ion Batteries And Emerging Energy Electrochemical Systems* **2018**, *4*, 237–318.
- (414) Gofer, Y.; Turgeman, R.; Cohen, H.; Aurbach, D. XPS Investigation of Surface Chemistry of Magnesium Electrodes in Contact with Organic Solutions of Organochloroaluminate Complex Salts. *Langmuir* **2003**, *19*, 2344–2348.
- (415) Levi, E.; Gofer, Y.; Aurbach, D. On the Way to Rechargeable Mg Batteries: The Challenge of New Cathode Materials. *Chem. Mater.* **2010**, *22*, 860–868.
- (416) Ling, C.; Zhang, R. Manganese Dioxide As Rechargeable Magnesium Battery Cathode. *Front. Energy Res.* **2017**, *5*, 30.
- (417) Muldoon, J.; Bucur, C. B.; Oliver, A. G.; Sugimoto, T.; Matsui, M.; Kim, H. S.; Allred, G. D.; Zajicek, J.; Kotani, Y. Electrolyte Roadblocks to a Magnesium Rechargeable Battery. *Energy Environ. Sci.* **2012**, *5*, 5941–5950.
- (418) Yagi, S.; Tanaka, A.; Ichikawa, Y.; Ichitsubo, T.; Matsubara, E. Electrochemical Stability of Magnesium Battery Current Collectors in a Grignard Reagent-Based Electrolyte. *J. Electrochem. Soc.* **2013**, *160*, C83–C88.
- (419) Shao, Y.; Gu, M.; Li, X.; Nie, Z.; Zuo, P.; Li, G.; Liu, T.; Xiao, J.; Cheng, Y.; Wang, C.; Zhang, J. G.; Liu, J. Highly Reversible Mg Insertion in Nanostructured Bi for Mg Ion Batteries. *Nano Lett.* **2014**, *14*, 255–260.
- (420) Tan, Y. H.; Yao, W. T.; Zhang, T.; Ma, T.; Lu, L. L.; Zhou, F.; Yao, H.-B.; Yu, S. H. High Voltage Magnesium-Ion Battery Enabled by Nanocluster Mg<sub>3</sub>Bi<sub>2</sub> Alloy Anode in Noncorrosive Electrolyte. *ACS Nano* **2018**, *12*, 5856–5865.
- (421) Jin, W.; Li, Z.; Wang, Z.; Fu, Y. Q. Mg Ion Dynamics in Anode Materials of Sn and Bi for Mg-Ion Batteries. *Mater. Chem. Phys.* **2016**, *182*, 167–172.
- (422) Niu, J.; Gao, H.; Ma, W.; Luo, F.; Yin, K.; Peng, Z.; Zhang, Z. Dual Phase Enhanced Superior Electrochemical Performance of Nanoporous Bismuth-Tin Alloy Anodes for Magnesium-Ion Batteries. *Energy Storage Mater.* **2018**, *14*, 351–360.
- (423) Murgia, F.; Stievano, L.; Monconduit, L.; Berthelot, R. Insight into the Electrochemical Behavior of Micrometric Bi and Mg<sub>3</sub>Bi<sub>2</sub> as High Performance Negative Electrodes for Mg Batteries. *J. Mater. Chem. A* **2015**, *3*, 16478–16485.
- (424) Arthur, T. S.; Singh, N.; Matsui, M. Electrodeposited Bi, Sb and Bi<sub>1</sub>-XSb Alloys as Anodes for Mg-Ion Batteries. *Electrochim. Commun.* **2012**, *16*, 103–106.
- (425) Singh, N.; Arthur, T. S.; Ling, C.; Matsui, M.; Mizuno, F. A High Energy-Density Tin Anode for Rechargeable Magnesium-Ion Batteries. *Chem. Commun.* **2013**, *49*, 149–151.
- (426) Parent, L. R.; Cheng, Y.; Sushko, P. V.; Shao, Y.; Liu, J.; Wang, C. M.; Browning, N. D. Realizing the Full Potential of Insertion Anodes for Mg-Ion Batteries through the Nanostructuring of Sn. *Nano Lett.* **2015**, *15*, 1177–1182.
- (427) Yaghoobnejad Asl, H.; Fu, J.; Kumar, H.; Welborn, S. S.; Shenoy, V. B.; Detsi, E. In Situ Dealloying of Bulk Mg<sub>2</sub>Sn in Mg-Ion Half Cell as an Effective Route to Nanostructured Sn for High Performance Mg-Ion Battery Anodes. *Chem. Mater.* **2018**, *30*, 1815–1824.
- (428) Cheng, Y.; Shao, Y.; Parent, L. R.; Sushko, M. L.; Li, G.; Sushko, P. V.; Browning, N. D.; Wang, C.; Liu, J. Interface Promoted Reversible Mg Insertion in Nanostructured Tin-Antimony Alloys. *Adv. Mater.* **2015**, *27*, 6598–6605.
- (429) Wu, N.; Lyu, Y.-C.; Xiao, R.-J.; Yu, X.; Yin, Y.-X.; Yang, X.-Q.; Li, H.; Gu, L.; Guo, Y.-G. A Highly Reversible, Low-Strain Mg-Ion Insertion Anode Material for Rechargeable Mg-Ion Batteries. *NPG Asia Mater.* **2014**, *6*, No. e120.
- (430) Wu, N.; Yang, Z. Z.; Yao, H. R.; Yin, Y. X.; Gu, L.; Guo, Y. G. Improving the Electrochemical Performance of the Li<sub>4</sub>Ti<sub>5</sub>O<sub>12</sub> Electrode in a Rechargeable Magnesium Battery by Lithium-Magnesium Co-Intercalation. *Angew. Chem., Int. Ed.* **2015**, *54*, 5757–5761.
- (431) Chen, C.; Wang, J.; Zhao, Q.; Wang, Y.; Chen, J. Layered Na<sub>2</sub>Ti<sub>3</sub>O<sub>7</sub>/MgNaTi<sub>3</sub>O<sub>7</sub>/Mg<sub>0.5</sub>NaTi<sub>3</sub>O<sub>7</sub> Nanoribbons as High-Performance Anode of Rechargeable Mg-Ion Batteries. *ACS Energy Lett.* **2016**, *1*, 1165–1172.
- (432) Wu, N.; Yao, W.; Song, X.; Zhang, G.; Chen, B.; Yang, J.; Tang, Y. A Calcium-Ion Hybrid Energy Storage Device with High Capacity and Long Cycling Life under Room Temperature. *Adv. Energy Mater.* **2019**, *9*, 180386S.
- (433) Yao, Z.; Hegde, V. I.; Aspuru-Guzik, A.; Wolverton, C. Discovery of Calcium-Metal Alloy Anodes for Reversible Ca-Ion Batteries. *Adv. Energy Mater.* **2019**, *9*, 1802994.
- (434) Wang, M.; Jiang, C.; Zhang, S.; Song, X.; Tang, Y.; Cheng, H. M. Reversible Calcium Alloying Enables a Practical Room-Temperature Rechargeable Calcium-Ion Battery with a High Discharge Voltage. *Nat. Chem.* **2018**, *10*, 667–672.
- (435) Attias, R.; Salama, M.; Hirsch, B.; Goffer, Y.; Aurbach, D. Anode-Electrolyte Interfaces in Secondary Magnesium Batteries. *Joule* **2019**, *3*, 27–52.
- (436) Ma, Z.; MacFarlane, D. R.; Kar, M. Mg Cathode Materials and Electrolytes for Rechargeable Mg Batteries: A Review. *Batter. Supercaps* **2019**, *2*, 115–127.
- (437) Rajput, N. N.; Seguin, T. J.; Wood, B. M.; Qu, X.; Persson, K. A. Elucidating Solvation Structures for Rational Design of Multivalent Electrolytes—A Review. *Top. Curr. Chem.* **2018**, *376*, 19.
- (438) Gaddum, L. W.; French, H. E. The Electrolysis of Grignard Solutions. *J. Am. Chem. Soc.* **1927**, *49*, 1295–1299.
- (439) Pour, N.; Gofer, Y.; Major, D. T.; Aurbach, D. Structural Analysis of Electrolyte Solutions for Rechargeable Mg Batteries by Stereoscopic Means and DFT Calculations. *J. Am. Chem. Soc.* **2011**, *133*, 6270–6278.
- (440) Doe, R. E.; Han, R.; Hwang, J.; Gmitter, A. J.; Shterenberg, I.; Yoo, H. D.; Pour, N.; Aurbach, D. Novel, Electrolyte Solutions Comprising Fully Inorganic Salts with High Anodic Stability for Rechargeable Magnesium Batteries. *Chem. Commun.* **2014**, *50*, 243–245.
- (441) See, K. A.; Chapman, K. W.; Zhu, L.; Wiaderek, K. M.; Borkiewicz, O. J.; Barile, C. J.; Chupas, P. J.; Gewirth, A. A. The Interplay of Al and Mg Speciation in Advanced Mg Battery Electrolyte Solutions. *J. Am. Chem. Soc.* **2016**, *138*, 328–337.
- (442) Nagy, Z.; Blaudeau, J. P.; Hung, N. C.; Curtiss, L. A.; Zurawski, D. J. Chloride Ion Catalysis of the Copper Deposition Reaction. *J. Electrochim. Soc.* **1995**, *142*, L87–L89.
- (443) Soares, D. M.; Wasle, S.; Weil, K. G.; Doblhofer, K. Copper Ion Reduction Catalyzed by Chloride Ions. *J. Electroanal. Chem.* **2002**, *532*, 353–358.
- (444) Johnson, D. C.; Resnick, E. W. Electrocatalysis of the Reduction of Iron(III) by Halides Adsorbed at Platinum Electrodes in Perchloric Acid Solutions. *Anal. Chem.* **1977**, *49*, 1918–1924.
- (445) Son, S. B.; Gao, T.; Harvey, S. P.; Steirer, K. X.; Stokes, A.; Norman, A.; Wang, C.; Cresce, A.; Xu, K.; Ban, C. An Artificial Interphase Enables Reversible Magnesium Chemistry in Carbonate Electrolytes. *Nat. Chem.* **2018**, *10*, 532–539.
- (446) Lapidus, S. H.; Rajput, N. N.; Qu, X.; Chapman, K. W.; Persson, K. A.; Chupas, P. J. Solvation Structure and Energetics of Electrolytes for Multivalent Energy Storage. *Phys. Chem. Chem. Phys.* **2014**, *16*, 21941–21945.
- (447) Giffin, G. A.; Moretti, A.; Jeong, S.; Passerini, S. Complex Nature of Ionic Coordination in Magnesium Ionic Liquid-Based

- Electrolytes: Solvates with Mobile Mg<sup>2+</sup> Cations. *J. Phys. Chem. C* **2014**, *118*, 9966–9973.
- (448) Lau, K.-C.; Seguin, T. J.; Carino, E. V.; Hahn, N. T.; Connell, J. G.; Ingram, B. J.; Persson, K. A.; Zavadil, K. R.; Liao, C. Widening Electrochemical Window of Mg Salt by Weakly Coordinating Perfluoroalkoxyaluminate Anion for Mg Battery Electrolyte. *J. Electrochem. Soc.* **2019**, *166*, A1510–A1519.
- (449) Zhao-Karger, Z.; Liu, R.; Dai, W.; Li, Z.; Diermant, T.; Vinayan, B. P.; Bonatto Minella, C.; Yu, X.; Manthiram, A.; Behm, R. J.; Ruben, M.; Fichtner, M. Toward Highly Reversible Magnesium-Sulfur Batteries with Efficient and Practical Mg[B(Hfip)<sub>4</sub>]<sub>2</sub> Electrolyte. *ACS Energy Lett.* **2018**, *3*, 2005–2013.
- (450) Gofer, Y.; Chusid, O.; Gizbar, H.; Viestfrid, Y.; Gottlieb, H. E.; Marks, V.; Aurbach, D. Improved Electrolyte Solutions for Rechargeable Magnesium Batteries. *Electrochim. Solid-State Lett.* **2006**, *9*, A257.
- (451) Aurbach, D.; Suresh, G. S.; Levi, E.; Mitelman, A.; Mizrahi, O.; Chusid, O.; Brunelli, M. Progress in Rechargeable Magnesium Battery Technology. *Adv. Mater.* **2007**, *19*, 4260–4267.
- (452) Ha, S. Y.; Lee, Y. W.; Woo, S. W.; Koo, B.; Kim, J. S.; Cho, J.; Lee, K. T.; Choi, N. S. Magnesium(II) Bis(Trifluoromethane Sulfonyl) Imide-Based Electrolytes with Wide Electrochemical Windows for Rechargeable Magnesium Batteries. *ACS Appl. Mater. Interfaces* **2014**, *6*, 4063–4073.
- (453) Hahn, N. T.; Seguin, T. J.; Lau, K. C.; Liao, C.; Ingram, B. J.; Persson, K. A.; Zavadil, K. R. Enhanced Stability of the Carba-Closododecaborate Anion for High-Voltage Battery Electrolytes through Rational Design. *J. Am. Chem. Soc.* **2018**, *140*, 11076–11084.
- (454) Zhao-Karger, Z.; Zhao, X.; Wang, D.; Diermant, T.; Behm, R. J.; Fichtner, M. Performance Improvement of Magnesium Sulfur Batteries with Modified Non-Nucleophilic Electrolytes. *Adv. Energy Mater.* **2015**, *5*, 1401155.
- (455) Jay, R.; Tomich, A. W.; Zhang, J.; Zhao, Y.; De Gorostiza, A.; Lavallo, V.; Guo, J. Comparative Study of Mg(CB 11 H 12) 2 and Mg(TFSI) 2 at the Magnesium/Electrolyte Interface. *ACS Appl. Mater. Interfaces* **2019**, *11*, 11414–11420.
- (456) Rajput, N. N.; Qu, X.; Sa, N.; Burrell, A. K.; Persson, K. A. The Coupling between Stability and Ion Pair Formation in Magnesium Electrolytes from First-Principles Quantum Mechanics and Classical Molecular Dynamics. *J. Am. Chem. Soc.* **2015**, *137*, 3411–3420.
- (457) Seguin, T. J.; Hahn, N. T.; Zavadil, K. R.; Persson, K. A. Elucidating Non-Aqueous Solvent Stability and Associated Decomposition Mechanisms for Mg Energy Storage Applications from First-Principles. *Front. Chem.* **2019**, *7*, 175.
- (458) Tutusaus, O.; Mohtadi, R.; Arthur, T. S.; Mizuno, F.; Nelson, E. G.; Sevryugina, Y. V. An Efficient Halogen-Free Electrolyte for Use in Rechargeable Magnesium Batteries. *Angew. Chem., Int. Ed.* **2015**, *54*, 7900–7904.
- (459) Zhang, Z.; Cui, Z.; Qiao, L.; Guan, J.; Xu, H.; Wang, X.; Hu, P.; Du, H.; Li, S.; Zhou, X.; Dong, S.; Liu, Z.; Cui, G.; Chen, L. Novel Design Concepts of Efficient Mg-Ion Electrolytes toward High-Performance Magnesium-Selenium and Magnesium-Sulfur Batteries. *Adv. Energy Mater.* **2017**, *7*, 1602055.
- (460) Ta, K.; Zhang, R.; Shin, M.; Rooney, R. T.; Neumann, E. K.; Gewirth, A. A. Understanding Ca Electrodeposition and Speciation Processes in Nonaqueous Electrolytes for Next-Generation Ca-Ion Batteries. *ACS Appl. Mater. Interfaces* **2019**, *11*, 21536–21542.
- (461) Mao, M.; Gao, T.; Hou, S.; Wang, C. A Critical Review of Cathodes for Rechargeable Mg Batteries. *Chem. Soc. Rev.* **2018**, *47*, 8804–8841.
- (462) Levi, E.; Lancry, E.; Mitelman, A.; Aurbach, D.; Isnard, O.; Djurado, D. Phase Diagram of Mg Insertion into Chevrel Phases, Mg<sub>x</sub>Mo<sub>6</sub>T<sub>8</sub> (T = S, Se). 2. The Crystal Structure of Triclinic MgMo<sub>6</sub>Se<sub>8</sub>. *Chem. Mater.* **2006**, *18*, 3705–3714.
- (463) Levi, E.; Lancry, E.; Mitelman, A.; Aurbach, D.; Ceder, G.; Morgan, D.; Isnard, O. Phase Diagram of Mg Insertion into Chevrel Phases, Mg XMo<sub>6</sub>T<sub>8</sub> (T = S, Se). 1. Crystal Structure of the Sulfides. *Chem. Mater.* **2006**, *18*, 5492–5503.
- (464) Sun, X.; Bonnick, P.; Nazar, L. F. Layered TiS<sub>2</sub> Positive Electrode for Mg Batteries. *ACS Energy Lett.* **2016**, *1*, 297–301.
- (465) Gu, Y.; Katsura, Y.; Yoshino, T.; Takagi, H.; Taniguchi, K. Rechargeable Magnesium-Ion Battery Based on a TiSe<sub>2</sub>-Cathode with d-p Orbital Hybridized Electronic Structure. *Sci. Rep.* **2015**, *5*, 12486.
- (466) Sun, X.; Bonnick, P.; Duffort, V.; Liu, M.; Rong, Z.; Persson, K. A.; Ceder, G.; Nazar, L. F. A High Capacity Thiospinel Cathode for Mg Batteries. *Energy Environ. Sci.* **2016**, *9*, 2273–2277.
- (467) Bonnick, P.; Sun, X.; Lau, K. C.; Liao, C.; Nazar, L. F. Monovalent versus Divalent Cation Diffusion in Thiospinel Ti<sub>2</sub>S<sub>4</sub>. *J. Phys. Chem. Lett.* **2017**, *8*, 2253–2257.
- (468) Verrelli, R.; Black, A. P.; Pattanathummasid, C.; Tchitchevka, D. S.; Ponrouch, A.; Oró-Solé, J.; Frontera, C.; Bardé, F.; Rozier, P.; Palacín, M. R. On the Strange Case of Divalent Ions Intercalation in V<sub>2</sub>O<sub>5</sub>. *J. Power Sources* **2018**, *407*, 162–172.
- (469) Gershinsky, G.; Yoo, H. D.; Gofer, Y.; Aurbach, D. Electrochemical and Spectroscopic Analysis of Mg<sup>2+</sup> Intercalation into Thin Film Electrodes of Layered Oxides: V<sub>2</sub>O<sub>5</sub> and MoO<sub>3</sub>. *Langmuir* **2013**, *29*, 10964–10972.
- (470) Spahr, M. E.; Novák, P.; Haas, O.; Nesper, R. Electrochemical Insertion of Lithium, Sodium, and Magnesium in Molybdenum(VI) Oxide. *J. Power Sources* **1995**, *54*, 346–351.
- (471) Feng, Z.; Yang, J.; NuLi, Y.; Wang, J.; Wang, X.; Wang, Z. Preparation and Electrochemical Study of a New Magnesium Intercalation Material Mg<sub>1.03</sub>Mn<sub>0.97</sub>SiO<sub>4</sub>. *Electrochim. Commun.* **2008**, *10*, 1291–1294.
- (472) Li, Y.; Nuli, Y. N.; Yang, J.; Yilinuer, T.; Wang, J. L. MgFeSiO<sub>4</sub> Prepared via a Molten Salt Method as a New Cathode Material for Rechargeable Magnesium Batteries. *Chin. Sci. Bull.* **2011**, *56*, 386–390.
- (473) Ling, C.; Banerjee, D.; Song, W.; Zhang, M.; Matsui, M. First-Principles Study of the Magnesiation of Olivines: Redox Reaction Mechanism, Electrochemical and Thermodynamic Properties. *J. Mater. Chem.* **2012**, *22*, 13517–13523.
- (474) Orikasa, Y.; Masese, T.; Koyama, Y.; Mori, T.; Hattori, M.; Yamamoto, K.; Okado, T.; Huang, Z.-D.; Minato, T.; Tassel, C.; Kim, J.; Kobayashi, Y.; Abe, T.; Kageyama, H.; Uchimoto, Y. High Energy Density Rechargeable Magnesium Battery Using Earth-Abundant and Non-Toxic Elements. *Sci. Rep.* **2014**, *4*, 5622.
- (475) Cabello, M.; Nacimiento, F.; Alcántara, R.; Lavela, P.; Pérez Vicente, C.; Tirado, J. L. Applicability of Molybdate as an Electrode Material in Calcium Batteries: A Structural Study of Layer-Type Ca<sub>x</sub>MoO<sub>3</sub>. *Chem. Mater.* **2018**, *30*, 5853–5861.
- (476) Tojo, T.; Tawa, H.; Oshida, N.; Inada, R.; Sakurai, Y. Electrochemical Characterization of a Layered  $\alpha$ -MoO<sub>3</sub> as a New Cathode Material for Calcium Ion Batteries. *J. Electroanal. Chem.* **2018**, *825*, 51–56.
- (477) Lipson, A. L.; Pan, B.; Lapidus, S. H.; Liao, C.; Vaughney, J. T.; Ingram, B. J. Rechargeable Ca-Ion Batteries: A New Energy Storage System. *Chem. Mater.* **2015**, *27*, 8442–8447.
- (478) Dacek, S. T.; Richards, W. D.; Kitchaev, D. A.; Ceder, G. Structure and Dynamics of Fluorophosphate Na-Ion Battery Cathodes. *Chem. Mater.* **2016**, *28*, 5450–5460.
- (479) Chen, T.; Sai Gautam, G.; Huang, W.; Ceder, G. First-Principles Study of the Voltage Profile and Mobility of Mg Intercalation in a Chromium Oxide Spinel. *Chem. Mater.* **2018**, *30*, 153–162.
- (480) Liu, M.; Rong, Z.; Malik, R.; Canepa, P.; Jain, A.; Ceder, G.; Persson, K. A. Spinel Compounds as Multivalent Battery Cathodes: A Systematic Evaluation Based on Ab Initio Calculations. *Energy Environ. Sci.* **2015**, *8*, 964–974.
- (481) Rong, Z.; Malik, R.; Canepa, P.; Sai Gautam, G.; Liu, M.; Jain, A.; Persson, K.; Ceder, G. Materials Design Rules for Multivalent Ion Mobility in Intercalation Structures. *Chem. Mater.* **2015**, *27*, 6016–6021.
- (482) Smeu, M.; Hossain, M. S.; Wang, Z.; Timosheskii, V.; Bevan, K. H.; Zaghib, K. Theoretical Investigation of Chevrel Phase Materials for Cathodes Accommodating Ca<sup>2+</sup> Ions. *J. Power Sources* **2016**, *306*, 431–436.
- (483) Emly, A.; Van Der Ven, A. Mg Intercalation in Layered and Spinel Host Crystal Structures for Mg Batteries. *Inorg. Chem.* **2015**, *54*, 4394–4402.

- (484) Yoo, H. D.; Liang, Y.; Dong, H.; Lin, J.; Wang, H.; Liu, Y.; Ma, L.; Wu, T.; Li, Y.; Ru, Q.; Jing, Y.; An, Q.; Zhou, W.; Guo, J.; Lu, J.; Pantelides, S. T.; Qian, X.; Yao, Y. Fast Kinetics of Magnesium Monochloride Cations in Interlayer-Expanded Titanium Disulfide for Magnesium Rechargeable Batteries. *Nat. Commun.* **2017**, *8*, 339.
- (485) Juran, T. R.; Smeu, M. TiSe<sub>2</sub> Cathode for beyond Li-Ion Batteries. *J. Power Sources* **2019**, *436*, 226813.
- (486) Liu, M.; Jain, A.; Rong, Z.; Qu, X.; Canepa, P.; Malik, R.; Ceder, G.; Persson, K. A. Evaluation of Sulfur Spinel Compounds for Multivalent Battery Cathode Applications. *Energy Environ. Sci.* **2016**, *9*, 3201–3209.
- (487) Kim, C.; Phillips, P. J.; Key, B.; Yi, T.; Nordlund, D.; Yu, Y. S.; Bayliss, R. D.; Han, S. D.; He, M.; Zhang, Z.; Burrell, A. K.; Klie, R. F.; Cabana, J. Direct Observation of Reversible Magnesium Ion Intercalation into a Spinel Oxide Host. *Adv. Mater.* **2015**, *27*, 3377–3384.
- (488) Wustrow, A.; Key, B.; Phillips, P. J.; Sa, N.; Lipton, A. S.; Klie, R. F.; Vaughay, J. T.; Poeppelmeier, K. R. Synthesis and Characterization of MgCr<sub>2</sub>S<sub>4</sub> Thiospinel as a Potential Magnesium Cathode. *Inorg. Chem.* **2018**, *57*, 8634–8638.
- (489) Rouxel, J. Anion-Cation Redox Competition and the Formation of New Compounds in Highly Covalent Systems. *Chem. - Eur. J.* **1996**, *35*, 1053–1059.
- (490) Sai Gautam, G.; Canepa, P.; Urban, A.; Bo, S. H.; Ceder, G. Influence of Inversion on Mg Mobility and Electrochemistry in Spinels. *Chem. Mater.* **2017**, *29*, 7918–7930.
- (491) Brown, I. D. What Factors Determine Cation Coordination Numbers? *Acta Crystallogr., Sect. B: Struct. Sci.* **1988**, *44*, 545–553.
- (492) Kulish, V. V.; Koch, D.; Manzhos, S. Aluminium and Magnesium Insertion in Sulfur-Based Spinels: A First-Principles Study. *Phys. Chem. Chem. Phys.* **2017**, *19*, 6076–6081.
- (493) Hannah, D. C.; Sai Gautam, G.; Canepa, P.; Rong, Z.; Ceder, G. Magnesium Ion Mobility in Post-Spinels Accessible at Ambient Pressure. *Chem. Commun.* **2017**, *53*, 5171–5174.
- (494) Sun, X.; Blanc, L.; Nolis, G. M.; Bonnick, P.; Cabana, J.; Nazar, L. F. NaV<sub>1.25</sub>Ti<sub>0.75</sub>O<sub>4</sub>: A Potential Post-Spinel Cathode Material for Mg Batteries. *Chem. Mater.* **2018**, *30*, 121–128.
- (495) Rong, Z.; Xiao, P.; Liu, M.; Huang, W.; Hannah, D. C.; Scullin, W.; Persson, K. A.; Ceder, G. Fast Mg<sup>2+</sup> Diffusion in Mo<sub>3</sub>(PO<sub>4</sub>)<sub>3</sub>O for Mg Batteries. *Chem. Commun.* **2017**, *53*, 7998–8001.
- (496) Lightfoot, P.; Krok, F.; Nowinski, J. L.; Bruce, P. G. Structure of the Cubic Intercalate Mg<sub>x</sub>TiS<sub>2</sub>. *J. Mater. Chem.* **1992**, *2*, 139–140.
- (497) Yoshino, A. The Birth of the Lithium-Ion Battery. *Angew. Chem., Int. Ed.* **2012**, *51*, 5798–5800.
- (498) Xie, F.; Liu, C.; Li, S.; Lin, Z.; Huang, Y. Long-Term Strategic Planning of Inter-City Fast Charging Infrastructure for Battery Electric Vehicles. *Transp. Res. Part E Logist. Transp. Rev.* **2018**, *109*, 261–276.
- (499) Donaldson, L. Making Fast-Charging Electric Vehicles a Possibility. *Mater. Today* **2018**, *21*, 105–106.
- (500) Zeng, X.; Li, M.; Abd El-Hady, D.; Alshitari, W.; Al-Bogami, A. S.; Lu, J.; Amine, K. Commercialization of Lithium Battery Technologies for Electric Vehicles. *Adv. Energy Mater.* **2019**, *9*, 1900161.
- (501) Ziegler, M. S.; Mueller, J. M.; Pereira, G. D.; Song, J.; Ferrara, M.; Chiang, Y. M.; Trancik, J. E. Storage Requirements and Costs of Shaping Renewable Energy Toward Grid Decarbonization. *Joule* **2019**, *3*, 2134–2153.
- (502) Gao, H.; Seymour, I. D.; Xin, S.; Xue, L.; Henkelman, G.; Goodenough, J. B. Na<sub>3</sub>MnZr(PO<sub>4</sub>)<sub>3</sub>: A High-Voltage Cathode for Sodium Batteries. *J. Am. Chem. Soc.* **2018**, *140*, 18192–18199.